

Performance and Stability of Semiconductor Nanowire Devices

Dissertation

zur Erlangung des akademischen Grades
doctor rerum naturalium (Dr. rer. nat.)

vorgelegt dem Rat der Physikalisch-Astronomischen Fakultät der
Friedrich-Schiller-Universität Jena



**FRIEDRICH-SCHILLER-
UNIVERSITÄT
JENA**

von M.Sc. Maximilian Zapf
geboren am 07.05.1992 in Bayreuth

1. Gutachter: Prof. Dr. Carsten Ronning, Friedrich-Schiller-Universität Jena

2. Gutachter: Prof. Dr. Tobias Voss, Technische Universität Braunschweig

3. Gutachter: Prof. Dr. Chennupati Jagadish, Australian National University

Tag der Abgabe: 29.03.2021

Tag der Disputation: 22.07.2021

Abstract

Nanotechnology is a key element in modern technological progress offering solutions to some of the most pressing issues for society, such as in the fields of health, communication, and energy consumption. The solutions that nanotechnology provides comprise amplifiers, actuators, or sensors and emitters, etc. as building blocks operating at the nanoscale. Semiconductor nanowires are perfectly suited for the use in such applications, as they not only provide functional electronic and optical properties but also nanoscale dimensions. Their high aspect ratio furthermore makes them inherently suited to bridge scales from the nanoscale to the macroscopic scales humans interact with. Key requirements for such nanodevices—besides the high functionality—are also reliability and stability. A thorough understanding of the operation and the limitations of nanowire-based devices is therefore urgently needed.

Here, the operation, stability, and degradation of optoelectronic and all-optical devices based on semiconductor nanowires are investigated. Ultra-high spatial resolution hard X-ray detection is demonstrated using a GaAs nanowire with an axial p-n junction. Advanced X-ray analytical techniques are applied to study the detector operation by monitoring internal electrical fields in-operando. Inspecting the stability, a hot electron beam-induced selective oxidization of the n-type nanowire segment is observed.

Further, the operation and stability of all-optical ZnO and CdS nanowire devices are investigated. The spontaneous and stimulated emission from the nanowires is detected as a function of electron irradiation using an electron microscope. As electron beams are frequently used for nanoscale sample inspection and fabrication, an understanding is sought for electron beam-induced changes of the optical properties. Slight changes are observed for the spontaneous emission, while the stimulated emission is drastically reduced due to a lowered waveguiding efficiency. These findings are attributed to changes in the surface band bending and non-radiative recombination centers. Finally, the power dependence of ZnO and CdS nanowire lasers were studied in detail. For high excitation power densities, a degradation is observed. The temperature-dependence of the threshold for degradation and the lasing threshold are presented and an upper temperature limit for lasing is determined.

The major limitations for the stable operation of nanowire-based optoelectronic and

all-optical devices are thus shown: the large surface-to-volume ratio facilitates the surface degradation, while the reduced thermal conductivity in nanowires enables the local build-up of heat gradients. This work thus contributes to the understanding of the inherent limitations of nanodevices, which is the basis for future improved device designs to enable long-term stable and reliable operation at the nanoscale.

Zusammenfassung

Die Nanotechnologie bildet ein Kernelement zur Lösung einiger der dringendsten gesellschaftlichen Herausforderungen in den Bereichen Gesundheit, Kommunikation und Energieverbrauch. Die von der Nanotechnologie angebotenen Lösungen beinhalten Verstärker, Aktuatoren oder Sensoren und Lichtquellen, die als nanoskalige Bausteine fungieren sollen. Halbleiternanodrähte sind ideal für viele solcher Anwendungen geeignet, da sie nanoskalige Dimensionen mit funktionalen elektrischen und optischen Eigenschaften verbinden. Ihr großes Aspektverhältnis macht sie außerdem inhärent geeignet, um eine Brücke von der Nano- zur Makroskala – der Ebene der menschlichen Interaktion – zu schlagen. Abgesehen von einer hohen Funktionalität sind insbesondere Zuverlässigkeit und Stabilität Kernanforderungen für nanoskalige Bauteile. Deshalb ist ein tiefgreifendes Verständnis für den Betrieb und die Limitationen von Nanodraht-basierten Bauelementen erforderlich.

Dazu werden in dieser Arbeit der Betrieb, die Stabilität und die Degradation von optoelektronischen und rein optischen Nanodraht-basierten Bauteilen untersucht. Ein GaAs Nanodraht mit einem integrierten axialen p-n Übergang wird genutzt, um die ultra-hochauflösende Detektion von harter Röntgenstrahlung zu demonstrieren. Der Betrieb des Detektors wird mit modernen Röntgenanalysemethoden überwacht, die Aufschluss über innere elektrische Felder geben. Die Stabilität des Detektors wird von einer selektiven Oxidation des n-dotierten Nanodrahtsegmentes durch hochenergetische Elektronen begrenzt.

Weiterhin werden der Betrieb und die Stabilität von rein optisch genutzten ZnO und CdS Nanodrähten betrachtet. Die spontane und stimulierte Emission der Nanodrähte wird in Abhängigkeit von der Bestrahlung mit Elektronen in einem Rasterelektronenmikroskop untersucht. Da Elektronenstrahlen häufig für die Betrachtung und Herstellung von nanoskaligen Bauelementen verwendet werden, ist ein Verständnis ihres Einflusses auf die optischen Eigenschaften der Probe unabdinglich. Für die spontane Emission zeigt sich lediglich eine schwache Änderung, während die stimulierte Emission aufgrund einer deutlich reduzierten Wellenleitungs-Effizienz drastisch abfällt. Diese Beobachtungen werden Änderungen in der Bänderverbiegung nahe der Oberfläche und nichtstrahlenden Rekombinationszentren zugeschrieben. Zudem wurde die

Leistungsabhängigkeit von ZnO und CdS Nanodrahtlasern im Detail analysiert. Bei hohen Anregungsdichten wird eine Degradation des Nanodrahtlasers beobachtet. Die Temperaturabhängigkeit des Schwellenwertes der Degradation und des Schwellenwertes für stimulierte Emission werden diskutiert und ein oberes Temperaturlimit des Laserprozesses wird bestimmt.

Die bestimmenden Limitationen für einen stabilen Betrieb von Nanodraht-basierten optoelektronischen und rein optischen Bauteilen werden somit aufgezeigt: das große Oberflächen-zu-Volumen-Verhältnis erleichtert eine Oberflächendegradation, während die reduzierte Wärmeleitfähigkeit in Nanodrähten zur Entstehung lokaler Temperaturgradienten führt. Diese Arbeit trägt zum Verständnis dieser inhärenten Beschränkungen von nanoskaligen Bauteilen bei und liefert somit wichtige Grundlagen für die zukünftige Konstruktion von stabilen und zuverlässigen Bauteilen auf der nanoskaligen Ebene.

Contents

1. Introduction	5
2. Fundamentals	11
2.1. General properties of the used material systems	11
2.1.1. Gallium arsenide	11
2.1.2. Zinc oxide	12
2.1.3. Cadmium sulfide	13
2.2. Electron matter interaction	13
2.3. Light matter interaction in II-IV nanowires	14
2.3.1. Excitation regimes	14
2.3.2. Optical emission	15
2.3.3. Waveguiding	17
2.3.4. Semiconductor lasing	18
2.4. X-ray matter interaction	21
2.4.1. X-ray fluorescence	22
2.4.2. X-ray absorption near edge structure spectroscopy	22
2.4.3. X-ray beam induced current	23
2.5. Semiconductor nanowires	23
2.5.1. Nanowire diodes	24
2.5.2. Band bending in ZnO nanowires	25
2.5.3. Defects and defect luminescence in ZnO	28
3. Experimental methods	31
3.1. Nanowire growth	31
3.1.1. Growth of ZnO and CdS nanowires	31

3.1.2.	Growth of axial GaAs nanowires	32
3.1.3.	Nanowire transfer and device fabrication	33
3.2.	Electron microscope-based characterization	34
3.2.1.	Scanning electron microscopy	34
3.2.2.	Energy-dispersive X-ray spectroscopy	34
3.3.	Optical characterization	35
3.3.1.	Photoluminescence	35
3.3.2.	Cathodoluminescence	37
3.4.	X-ray analytical methods	38
3.4.1.	X-ray fluorescence	39
3.4.2.	X-ray beam induced current	39
3.4.3.	X-ray absorption near edge spectroscopy	39
4.	An axial p-n junction nanowire X-ray detector at its limits	41
4.1.	X-ray detection	42
4.1.1.	Nanowire X-ray detector device	42
4.1.2.	Detector performance	43
4.1.3.	Voltage and incident energy dependence of the X-ray detection .	46
4.2.	X-ray absorption near edge structure analysis	49
4.2.1.	Degradation mechanism	49
4.2.2.	Assessing the selective oxidization	52
4.2.3.	Hot electron induced oxidization	55
4.3.	Conclusion	58
5.	Stability of photonic nanowire devices	61
5.1.	Limits of optical excitation in II-IV nanowire lasers	61
5.1.1.	Spontaneous luminescence and waveguiding in single nanowires	62
5.1.2.	Limits of the stimulated emission	67
5.2.	Influence of electron irradiation on the luminescence of nanowires . . .	72
5.2.1.	Electron irradiation dependent cathodoluminescence	73
5.2.2.	Possible interaction mechanisms	75
5.2.3.	Irradiation parameter dependency	78
5.2.4.	Electron irradiation dependent photoluminescence	80

5.2.5. Electron irradiation of nanowire lasers	86
5.2.6. Electron irradiation dependent waveguiding	88
5.2.7. Summarizing discussion of the electron irradiation	91
5.3. Conclusion	93
6. Conclusion and outlook	95
Bibliography	101
A. List of publications	i
B. Ehrenwörtliche Erklärung	v

1. Introduction

Nanotechnology, in its early days, caused people to envision both tremendous promises and horrible dangers [1, 2]. Like many new technologies, nanotechnology lost both the fears and the most utopian dreams in the course of time [3]. Neither was civilization destroyed by self-replicating nano-robots,¹ as some feared [5, 6], nor came true yet the hopes of others for efficient cancer medication or fast, disruptive commercialization of scientific discoveries [2, 7]. Today, dangers seen in nanotechnology are less catastrophic and mostly focus on environmental impact or toxicology [8, 9]. The promises of nanotechnology, however, are still immense; examples comprise medical-grade wearable sensor technology that could help prevent civilization diseases or the internet of nano-things that promises to speed up communication while decreasing energy consumption [10, 11].

Today, there is a variety of commercial products based on nanomaterials, such as sunscreens, laundry detergents, healthcare products, car wax, paints and inks, or food containers [12–15]. Almost all these widely distributed examples are based on passive nanotechnology, such as coatings, nanoparticles, nanostructured materials, etc. Passive nanotechnology is highly useful but does not suffice to hold up to the promises on the potential impact of nanotechnology [16]. Therefore, a large fraction of research towards nanotechnology is aimed at developing active devices [2] such as amplifiers, actuators, targeted drugs, or sensors and emitters that operate at the nanoscale [17, 18]. Utilizing such devices in future application poses the challenge to produce highly functional and stable nanodevices but also to connect the nanoscale with the macroscopic scales humans interact with [19]. Semiconductor nanowires

¹The so-called “gray goo” termed by K. Eric Drexler in his book “Engines of Creation: The Coming Era of Nanotechnology” [4].

are a class of nanomaterials inherently suited for bridging scales [20]: With lengths from few to tens of micrometers and diameters from few to hundreds of nanometers, semiconductor nanowires exhibit a high aspect ratio, a huge surface-to-volume-ratio [21, 22], and offer not only superior photonic properties—such as subwavelength light confinement and waveguiding [23–25]—but can also bridge the interface to electronic circuits enabled by their semiconducting properties [26]. This makes semiconductor nanowires an ideal platform for small-footprint optoelectronic building blocks. The nanowire geometry also offers an enhanced radiation stability compared to the bulk morphology [27], and the greatly increased elasticity range allows for applications in flexible (and even wearable) devices [28–31]. In short, nanowires are superior platforms for the miniaturization of active photonic and electronic devices enabled by the beneficial combination of their size, morphology, and semiconducting properties.

Nanowires can be fabricated either top-down—by sculpturing bulk structures to the nanoscale—or bottom-up—by growth from atomic/molecular constituents. Both methods have different strengths, which makes them useful for different applications [32]. Top-down fabrication is highly reproducible, allows etching very small structures, and enables a very good control of dopant incorporation [33]. Bottom-up growth results in a much smoother surface with less surface and bulk defects making it the future method of choice for most high-performance optoelectronic devices [34, 35]. Bottom-up fabrication further enables a good length control, lattice mismatched growth due to strain relaxation, and even the growth of metastable phases not achievable in bulk growth (such as wurtzite-structure GaAs [36, 37] or direct-bandgap, hexagonal Ge and SiGe [38]) [32, 39].

After growth, huge numbers of nanowires typically form ordered arrays or randomly oriented structures. There are several approaches that use such nanowire ensembles for, e.g., LEDs [40], high efficiency solar cells [41–44], photodetectors [45–47], or felt electrodes [48]. Compared to bulk, the nanowire architecture has several advantages such as a reduced material consumption and growth time accompanied with the ability to grow nearly without structural defects [49, 50]. Another approach for making use of the remarkable properties of semiconductor nanowires is designing *single nanowire* devices for nanoscale optoelectronics.

Single-nanowire optoelectronic devices The fundamental optoelectronic properties of semiconductor nanowires were studied in great detail in the last two decades, driven by the promise of a future integration as nanoscale devices into chip-based applications [28, 51–54]. Based on this, individual semiconductor nanowires were shown to be useful in a plethora of active optoelectronic devices that might be implemented in future integrated circuits or lab-on-a-chip devices [55, 56] as chemical [57, 58] or biological sensors [58], field effect transistors [59], phototransistors [60], photodetectors [61–66], or single nanowire spectrometers [67]. Furthermore, there is a great number of nanowire-based applications relying on p-n junctions at the heart of their functionality, such as single nanowire light emitting diodes [68–70], or detectors [70, 71]. Besides their use in such optoelectronic devices, nanowires also proved highly suitable for the use in all-optical nanowire-based devices, which rely on the purely photonic operation of individual semiconductor nanowires.

All-optical single-nanowire devices A wide spectrum of nanowire-based all-optical devices emerged in the last decade, comprising optical sensors [72–74], detectors [70, 71, 75], waveguides [24, 76], signal processors [77], optical switches [78], and light emitters in the spontaneous [68, 79] and stimulated [17, 80, 81] emission regime. These approaches are enabled by the combination of optical emission and confinement that nanowires intrinsically provide. By supplying sufficient optical pumping, nanowires thus constitute a suitable geometry for nanoscale laser sources [81–84]. The intense, coherent, and directional emission that such a nanolaser provides may enable future nanowire-based all-optical integrated circuits, optical lab-on-a-chip devices, or optical on-chip interconnects [17, 85, 86]. Although electrically driven nanowire lasers are favorable for most applications, especially for on-chip integrated photonics, they remain challenging to implement [87]; meanwhile optically driven nanowire lasers can readily be used in nanoscale applications [70, 85]. However, high optical pump powers are needed to overcome losses in such nanoscale lasers.

Historically, optically pumped nanowire lasing was first achieved in wide bandgap materials emitting in the near UV or the visible spectral range. Single nanowire lasing at room temperature was achieved in ZnO [88] and GaN [89] nanowires yielding emission wavelengths in the near UV. In the visible range, room temperature lasing

was observed in CdS [90] and CdSe [91]. Recently, stimulated emission in nanowires was successfully shifted to the near IR region using III–V materials, e.g., GaAs [92–94] and InP [34]. Yet, the IR region proved to be challenging for room temperature nanowire lasers. This is due to a high non-radiative surface recombination rate caused by the large surface-to-volume-ratio of nanowires [95] and as a result of the reduced gain in the materials suitable for these wavelengths [87]. Thus, achieving reasonably low lasing thresholds for stable room-temperature lasing in the near IR spectral region necessitates more elaborate efforts compared to the UV/visible range. In general, to achieve room temperature lasing, the lasing threshold for any given material must be sufficiently low such that it can be reached with reasonable pump power densities.

Challenges for integrating nanowires into real-world applications Despite the remarkable progress made in the field of semiconductor nanowire devices, real-world applications demand not only a cost-efficient mass production but also a deep understanding of their operation to ensure long-term stability and reliability [28, 96–98].

Tremendous progress was made regarding the fabrication of nanowires in the last decades including not only the growth of high crystalline quality nanowires free of structural defects [39, 49, 99], but also axial and core-shell heterostructure or homostructure nanowires [44, 100, 101]. One striking example is the recent establishment of the low-cost and high-throughput Aerotaxy production for axial GaAs nanowire p-n junctions [102].

However, this brings up the next critical points such as the precise positioning and alignment of nanowires at the desired location in the final nanodevice structure [19]. This can be realized either directly during growth—for example by selective-area epitaxy approaches [103–105]—or by post-growth repositioning—for example by transfer-printing microassembly [97].

Structure and scientific goals of this thesis

Besides growth and positioning, nanowire devices proved challenging regarding reliability of performance and stability [28, 74, 96, 106, 107], as their huge surface-to-volume ratio, and pronounced device-to-device variation renders them highly sensitive to environmental influences [108, 109]. Their reduced thermal conductivity—despite being beneficial for designing high thermoelectric figure of merit structures [110–112]—calls for a carefully considered heat management in nanowire optoelectronics [112–115]. This thesis thus explores several major aspects regarding the performance and stability of both optoelectronic and all-optical devices based on individual semiconductor nanowires. Special emphasis is put on investigating the physical properties that limit nanowire device stability aiming at solutions to overcome these limitations.

Chapter 2 – Fundamentals follows this introduction and gives an overview about the basic physical properties of nanowires for topics related to this thesis. The used material systems are introduced, and physical properties relating to the nanowire geometry are discussed. Further on, the interaction of electrons and photons—in the visible/near-UV as well as in the X-ray regime—with the semiconductor material is described.

Chapter 3 – Experimental methods summarizes the used experimental and simulation techniques. The methods used for the growth of semiconductor nanowires as well as the tools used for their characterization are presented with special focus on the synchrotron-based techniques and the setups used for photoluminescence and cathodoluminescence spectroscopy.

Chapter 4 – An axial p-n junction nanowire X-ray detector at its limits demonstrates the operation and stability of an optoelectronic nanodevice: a high-resolution X-ray detector realized by a GaAs nanowire with an embedded axial p-n junction. Such a detector offers a significantly improved spatial resolution compared to conventional bulk versions. In-operando X-ray analytical techniques with a focused synchrotron nanobeam are used to probe internal electrical fields allowing for a deep insight into the device operation. Finally, hot electron effects are discussed and the device stability and final degradation are studied in detail. Parts of this chapter are published in

reference [116].

Chapter 5 – Stability of photonic nanowire devices presents the operation and stability of ZnO and CdS nanowire all-optical devices. The spontaneous emission, the waveguiding, as well as the stimulated emission from ZnO nanowires is investigated as a function of electron-irradiation as applied in an electron microscope. Understanding the effects of electron irradiation on semiconductor nanowires is urgently needed, as electron beams are widely used for sample inspection and selection using electron microscopy, or for sample preparation using electron lithography. Nanowire lasers are further scrutinized with respect to their working range and degradation as a function of excitation intensity and temperature. Parts of this chapter are published in the state examination thesis of Gesine Thees [117] and the bachelor thesis of Johannes Nicklaus [118]. Parts of this chapter are published in reference [96].

Chapter 6 – Conclusion and outlook summarizes the major results of this thesis. Finally, an outlook on future experiments is given and future steps on the route to nanowire-based applications are envisioned.

2. Fundamentals

The material systems mostly addressed in this thesis are two “prototype” compound semiconductors, namely zinc oxide (along with cadmium sulfide) as a II-IV and gallium arsenide as a III-V compound. While silicon-based electronics dominate over a large market share, II-IV and III-V semiconductors have the potential to (and already do) fill niches for manifold applications from fast optical modulators to precise gas detectors [119–121]. The intrinsic material properties that define the degree of suitability for such applications will be discussed in this section. The nanowire geometry and its implications for several topics of interest to this thesis is considered throughout the discussion. Further on, a more detailed introduction is given to light-matter interaction, specifically related to nanowires, from the visible and the near-UV to the X-ray regime.

2.1. General properties of the used material systems

2.1.1. Gallium arsenide

In the cubic zincblende lattice of gallium arsenide (GaAs), one basis atom is positioned at (0,0,0) while the other is at $(\frac{1}{4}, \frac{1}{4}, \frac{1}{4})$ of the fcc unit cell with a cubic lattice constant of 5.5633 \AA [122, 123]. Also a wurtzite phase can be found at high pressures [37]. Remarkably, both the zincblende and the wurtzite phase can coexist in nanowires at ambient conditions [124, 125]. The crystal density of zincblende GaAs is 5.360 g cm^{-3} while its melting point is at $1238 \text{ }^\circ\text{C}$ [122]. A direct band gap of 1.425 eV at room temperature [122] makes GaAs an ideal material for photovoltaic and other optoelectronic

applications [126]. The long-wavelength phonon energies are 36.25 meV and 33.29 meV for longitudinal and transversal optical phonon modes (LO- and TO-phonons), respectively [127]. The interaction of electrons with phonons is usually described by the Fröhlich coupling parameters, which is 0.068 at the Γ valley and 0.152 at the X valley [128]; however, also transversal acoustic (TA) phonons are relevant for electron-phonon scattering processes [129]. The large static dielectric constant of 12.9 [130] and the small effective mass ($m_c = 0.063 m_e$) lead to weakly bound excitons with a binding energy of ~ 4 meV [131, 132].

2.1.2. Zinc oxide

Zinc oxide (ZnO) is a direct II-VI compound semiconductor with a mass density of 5.6 g cm^{-3} [133]. It is biocompatible and approved for use in cosmetic products (e.g., sunscreen, baby powder) and as food additive [134, 135]. At room temperature, the thermodynamically stable structure of ZnO is hexagonal wurtzite (lattice parameters $a = b = 3.296 \text{ \AA}$ and $c = 5.207 \text{ \AA}$ [136]) with a tetrahedral coordination, typically associated with covalent bonding; however, there is strong ionicity (0.616 [137] on the Phillips scale [138]) of the bonding leading to a large direct band gap of $E_g = 3.44 \text{ eV}$ at $T = 4 \text{ K}$ [139]. The valence band is split into three bands: the light hole and heavy hole bands, which are separated by spin-orbit coupling as well as the split-off band, where the degeneracy is lifted by the crystal field splitting. The energetic splitting between the A and B subbands is $\Delta E_{AB} = 4.9 \text{ meV}$ and the splitting between B and C is 43.7 meV [140].

The ordinary refractive index of ZnO is $n = 2.38$ with a dispersion of $dn/d\lambda = -15 \mu\text{m}^{-1}$ at a wavelength of $\lambda = 385 \text{ nm}$ [133, 141]. Excitons in ZnO have a binding energy of $\sim 60 \text{ meV}$ and are thus stable even above room temperature [140]. Due to the substantial ionic character, the Fröhlich coupling to LO phonons is particularly strong in ZnO [142].

2.1.3. Cadmium sulfide

Cadmium sulfide (CdS) is a direct II-VI semiconductor with a band gap of $E_g = 2.58$ eV at 1.6 K [143]. The wurtzite crystal phase is thermodynamically stable at room temperature with the lattice parameters $a = b = 4.14 \text{ \AA}$ and $c = 6.72 \text{ \AA}$ [144]. CdS is tetrahedrally coordinated with a Phillips ionicity of 0.69, i.e., larger than that of ZnO [145]. The band structure of CdS is similar to that of ZnO with a subband splitting of $\Delta E_{AB} = 16$ meV and $\Delta E_{BC} = 57$ meV [146]. The ordinary refractive index is $n = 2.83$ with a dispersion of $dn/d\lambda = -11.97 \mu\text{m}^{-1}$ at a wavelength of $\lambda = 510$ nm [147].

2.2. Electron matter interaction

When an electron hits a material, different elastic and non-elastic interaction processes are possible. Incident electrons therefore exhibit an energy loss with increasing penetration depth. The interaction volume of electrons in the sample can be estimated by the Kanaya-Okayama-range [148]:

$$R_{\text{K-O}} = \frac{27.6 A E_{\text{el}}^{1.67}}{Z^{0.89} \rho}, \quad (2.1)$$

where A is the atomic mass, Z is the average atomic number, E_{el} is the electron energy in keV. The three dimensional interaction volume can be simulated using Monte-Carlo methods (in this thesis, "CASINO" [149] was used). The simulation also yields the three dimensional energy loss distribution. In the interaction volume, the primary electrons can generate secondary electrons, backscattered electrons, and X-rays. The average energy necessary to create one electron-hole pair (E_{pair}) can be roughly approximated by $E_{\text{pair}} \approx 3E_g$, where E_g is the band gap energy [150]. The average energy transferred from an incident electron to the material is reduced by backscattering [151]; the total number of excited electron-hole pairs is given by:

$$G_0 = \frac{E_{\text{el}}}{E_{\text{pair}}} - \frac{E_{\text{be}}}{E_{\text{pair}}} Y_{\text{be}}, \quad (2.2)$$

with the average energy per backscattered electron E_{be} and the backscattering yield Y_{be} , which can both be determined via Monte-Carlo simulations. A certain fraction of the generated electron-hole pairs can recombine radiatively, yielding the cathodoluminescence (CL) signal. The detection of generated characteristic X-rays is used in energy-dispersive X-ray spectroscopy (EDX). Electrons can be elastically scattered—i.e., backscattered—or create secondary electrons, as used for electron microscope imaging.

2.3. Light matter interaction in II-IV nanowires

Upon external optical stimulation, semiconductors can be excited such that finally an electron is located in the conduction band and a hole remains in the valence band. The subsequent photoluminescence for different electron-hole pair generation rates is discussed in this section.

2.3.1. Excitation regimes

Electron-hole pairs in II-IV semiconductors typically do not recombine directly, but form hydrogen-like quasi-particles—(free) excitons—with lifetimes of tens of ps to few ns [152–155]. Due to a strong screening of the Coulomb interaction by the semiconductor material, their exciton Bohr radii exceed the unit cell (1.8 nm for ZnO and 2.8 nm for CdS) [156, 157]. These weakly bound excitons are referred to as Wannier-Mott-type; the exciton binding energies for ZnO (CdS) is 60 meV (28 meV), such that excitons are stable above (at) room temperature [143, 158]. Excitons couple strongly to the light field, such that they cannot be treated isolated from it. Thus, exciton-polaritons have to be considered: these quasi-particles are superimposed states of the excitonic excitation in the medium and the electromagnetic field. They describe an alternating process of exciton recombination resulting in photons, which in turn create electron-hole pairs that subsequently form excitons, and so on [159]. Excitons-polaritons and excitons will both be referred to as excitons in the following.

So far, only independent excitons were addressed, which is a reasonable description in the weak coupling limit for low electron-hole pair generation rates. Upon increasing the generation rate, interactions of different excitons become relevant, such as exciton-exciton or exciton-carrier scattering [160, 161]. Additionally, excitons can form bound complexes for higher generation rates—biexcitons, which are made up of 2 electrons and 2 holes. Similarly, trions can form, i.e., complexes of 2 electrons and 1 hole or of 1 electron and 2 holes [159]. In this intermediate density regime, the band gap is renormalized via exchange and correlation effects [158]; however, this is balanced by Pauli blocking and Coulomb screening that reduced the exciton binding energy, such that the exciton emission energy remains almost constant with increasing electron-hole pair generation rate [159, 162].

Increasing the generation rate further leads to the dissolution of the exciton quasi-particles. This happens when the electron-hole pair density reaches the Mott density

$$n_{\text{mott}} \approx 1/a_{\text{B}}^3, \quad (2.3)$$

i.e., the mean exciton distance falls below the Bohr radius a_{B} (however, this transition is not sharp) [158]. Electrons and holes in this high density regime form a collective phase—the electron-hole plasma. Mott densities for ZnO were reported in a range from $\sim 1.8 \times 10^{18} \text{ cm}^{-3}$ to $3.8 \times 10^{18} \text{ cm}^{-3}$, and in CdS from $\sim 5 \times 10^{17} \text{ cm}^{-3}$ to $1 \times 10^{19} \text{ cm}^{-3}$ [158, 163].

2.3.2. Optical emission

After excitation of the semiconductor to the low, intermediate, or high electron-hole pair density regime, light emission is observed. The power-dependent luminescence and different luminescence channels are described in the following.

Spontaneous luminescence In the luminescence process, there are several transitions possible, as sketched in figure 2.1a. At room temperature, the excitonic emission is not resolved and results in an emission band below the band gap energy, usually

referred to as near band edge (NBE) emission. Besides the NBE, a variety of defect bands is observed in large-bandgap semiconductors such as ZnO, resulting in the broad, unstructured deep level emission (DLE). This emission stems from transitions to or from deep acceptor or deep donor levels (see figure 2.1a). The different bands are commonly referred to as blue, green, orange, and red defect luminescence bands, however with no generally applied definition [164–169].

The intensity of the photoluminescence approximately follows a power law as a function of the excitation power density P :

$$I \propto P^k, \quad (2.4)$$

where the exponent k is between 1 to 2 for the excitonic emission [170],¹ while k is usually below 1 for the defect luminescence (however, the different transitions exhibit slightly different k values, indicating that they stem from different defect levels [173]). As a rule of thumb, k was observed to be constant in experiments when the excitation power density was varied for less than two orders of magnitude [171]. Further insights into the excitation power dependent luminescence were gained by solving coupled rate equations taking into account the background doping, photogenerated electrons and holes, as well as the rates for the different radiative or non-radiative decay channels (except for donor-acceptor pair recombination) [174–176]. In this way, the emission intensity of the NBE and the DLE were simulated as a function of the generation rate for ZnO nanowires [174] (see figure 2.1b).

Non-radiative recombination Besides the radiative recombination channels discussed above, non-radiative recombination processes are important in semiconductors [158, 177]. Non-radiative recombination processes imply that excited carriers transfer their energy to defect(-complexes) or surface sites with a fast energy dissipation to the crystal lattice via phonons [178]. Often, non-radiative recombination sites are referred to as “killer centers” as their occurrence severely affects electrical and optical properties, reduces device efficiency, and leads to a decrease in emission intensity [179]. The

¹The exponent k is 1 for resonant excitation but generally between 1 and 2 for free-exciton and bound-exciton emission [171, 172].

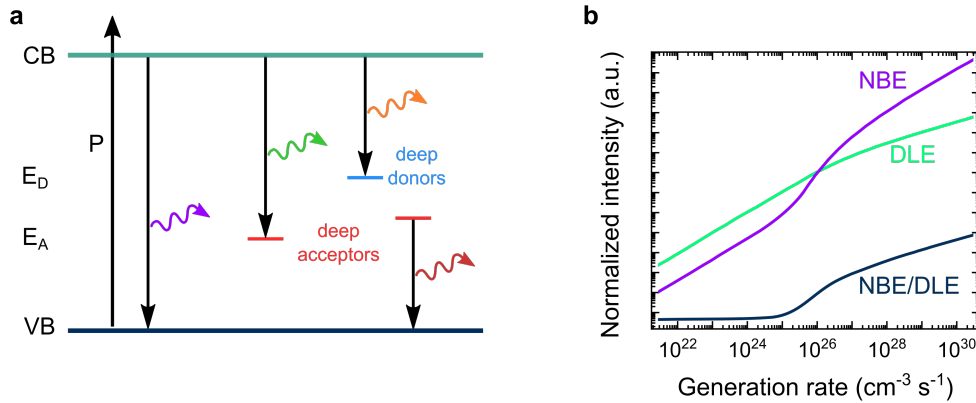


Figure 2.1.: Recombination processes. **a** Band diagram showing the energy levels of different exemplary recombination channels. Electrons are excited from the valence band above the bandgap with an excitation power density P . They subsequently relax non-radiatively to the conduction band edge. Direct band-to-band recombination (in ZnO, the recombination from excitonic states) competes with radiative recombination—via deep acceptor or donor states—and non-radiative recombination. **b** Photoluminescence intensity as a function of the electron-hole pair generation rate for the near band edge emission (NBE), deep level emission (DLE), and NBE-to-DLE-ratio. The data is taken from simulations of an ZnO nanowire in reference [174].

large surface-to-volume ratio renders non-radiative surface recombination processes dominant in nanostructures [93].

2.3.3. Waveguiding

The refractive index difference between nanowire ($n = 2.38$ for ZnO [141]) and its surrounding ($n = 1$ for air and $n = 1.5$ for silica substrates [180]) makes semiconductor nanowires efficient waveguides [23–25], similar to the principle of a step-index fiber [181]. This large refractive index difference also allows for a strong confinement of the light field such that vacuum wavelengths much larger than the nanowire diameter can be efficiently guided [24]. In contrast to conventional dielectric fibers, waveguiding in semiconductor nanowires induces absorption and emission for photon energies close to the band gap. Thus, in contrast to the passive dielectric waveguides, semiconductor nanowires are referred to as active waveguides [182]. Exponentially decaying states below the band gap—the Urbach tail states (see figure 2.2a)—allow for the re-absorption of photons with energies below the band gap (see figure 2.2b). The states were ascribed to result from a combination of impurities, structural disorder and exciton-phonon

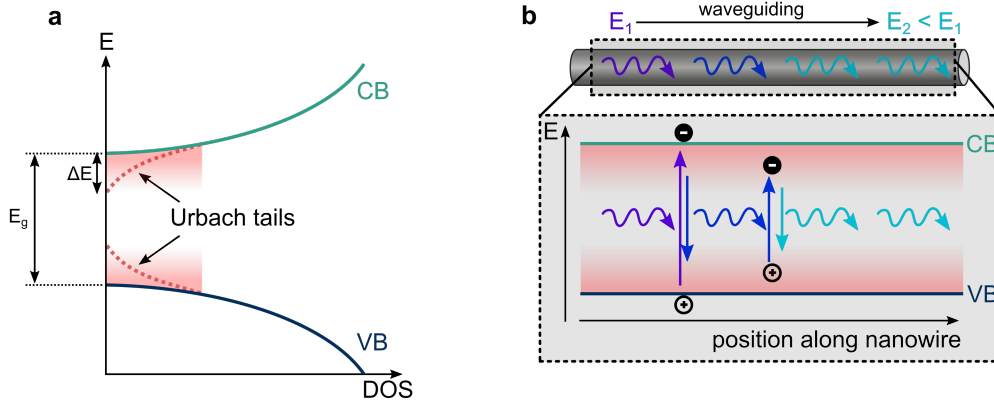


Figure 2.2.: Waveguiding in nanowires. **a** Scheme of the electronic density of states (DOS) in the band gap region of a semiconductor. The (greatly exaggerated) Urbach tails decay exponentially in the band gap and are shown as red dashed lines. **b** Scheme of the waveguiding redshift along the nanowire due to the repeated re-absorption and emission of photons in Urbach tail states and the subsequent energy loss. The energy loss ends when the photon energy drops below the absorption edge of the Urbach tails.

coupling [183, 184]. The empirical Urbach (or Urbach-Martienssen) rule [185, 186] gives the energy-dependent absorption coefficient below the exciton peak:

$$\alpha(E) = \alpha_0 \exp\left(\frac{E - E_0}{E_U}\right), \quad (2.5)$$

where α_0 and E_0 are characteristic parameters of the material ($\alpha_0 = 2.8 \times 10^6 \text{ cm}^{-1}$ and $E_0 = 3.62 \text{ eV}$ for ZnO [183]) and E_U is the Urbach energy, indicating the width of the exponential tail at a fixed temperature. At room temperature, values for E_U between 44 meV to 85 meV were found in ZnO [183, 187, 188]. The process of absorption in the Urbach tail states, emission, subsequent re-absorption, and so on, leads to a reduction in emission energy of light guided in the nanowire (see figure 2.2b) [189, 190].

2.3.4. Semiconductor lasing

Stimulated emission In the intermediate and high electron-hole pair density regime, light can be amplified by stimulated emission in semiconductors. While several processes, e.g., exciton-exciton scattering [191–193], exciton-carrier scattering [194] and exciton-phonon scattering [195], were discussed in literature as possible gain mechanisms, only the electron-hole plasma can provide sufficient gain to compensate for

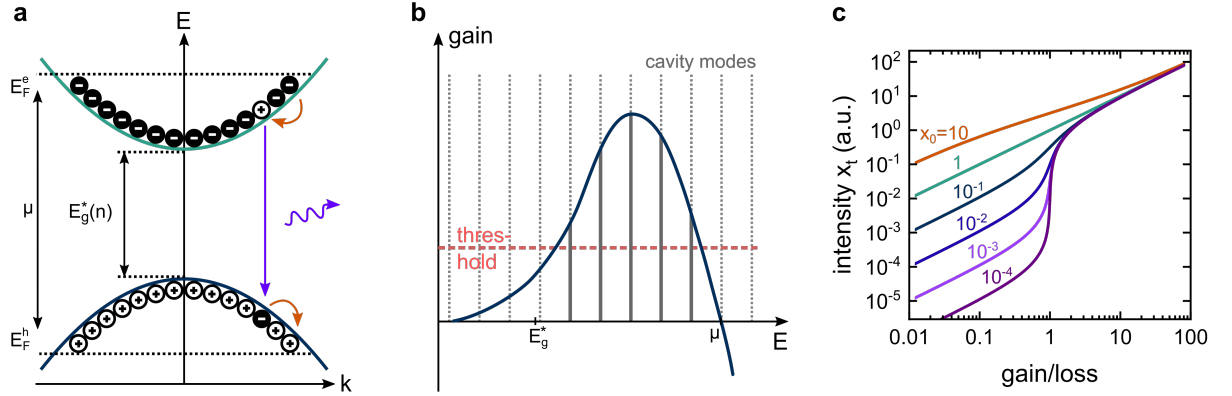


Figure 2.3.: Laser gain mechanism. **a** Scheme of the electron-hole plasma recombination process. Electrons (holes) fill the conduction (valence) band up to the quasi-Fermi level E_F^e (E_F^h). The recombination process (purple arrow) and the final state damping (orange arrows) are sketched. **b** Gain spectrum provided by an electron-hole plasma between the renormalized bandgap E_g^* and the chemical potential μ (the smooth tail below E_g^* is caused by final state damping [198]). Cavity modes (gray, vertical lines) exhibit amplification if their gain surpasses the threshold (red). **c** Emission intensity of a multimode laser as a function of the gain-to-loss ratio for different spontaneous emission parameters x_0 .

enhanced losses in nanowire lasers [196]. The gain coefficient of the electron-hole plasma is dependent on the laser material and is $\sim 7 \times 10^3 \text{ cm}^{-1}$ for ZnO [196] and $\sim 2.4 \times 10^4 \text{ cm}^{-1}$ for CdS at low temperatures [163]. As sketched in figure 2.3a, the gain provided by the electron-hole plasma stems from the recombination of electrons and holes in the conduction and valence band. The conduction (valence) band is filled with electrons (holes) up to the quasi Fermi energy. Electrons are absorbed into states with high momentum k , from where they relax into lower k states (in a timescale of fs) by carrier and phonon scattering processes [197]. Emission is enabled by recombination of relaxed electrons and holes from the low k states. Thus, the electron-hole plasma provides a quasi-4-level lasing system with fast (\sim fs) non-radiative transitions providing carriers for the laser transition (with longer lifetimes in the ps range). This results in gain in a spectral region $\Delta E = \mu - E_g^*(n)$, where lasing modes are supported (see figure 2.3b), with the transparency point μ as an upper limit and the renormalized bandgap $E_g^*(n)$ as the lower limit.

Optical resonator The nanowire geometry forms a cavity that allows Fabry-Pérot modes at spectral positions that are determined by the cavity (nanowire) length L :

$$\lambda_N = \frac{2n_{\lambda_N}L}{N}, \quad (2.6)$$

with the mode number N and the refractive index n_{λ_N} at the respective wavelength λ (see figure 2.3b). The mode spacing $\Delta\lambda$, i.e., the distance from one mode to its neighboring one, at the central wavelength λ is [199]

$$\Delta\lambda = \frac{1}{L} \left[\frac{\lambda^2}{2} \left(n - \lambda \frac{dn}{d\lambda} \right)^{-1} \right], \quad (2.7)$$

with the dispersion $\frac{dn}{d\lambda}$. To understand emission amplification, the fraction of the guided mode that overlaps the gain medium—the confinement factor Γ —must be considered. In nanowires, however, the confinement factor can exceed 1, which can be explained by the multiple side facet reflections in the waveguiding process, leading to an increased propagation distance [83, 200]. The material gain must therefore be replaced by the modal gain:

$$g_{\text{mod}}(E) = \Gamma g(E). \quad (2.8)$$

Simulated emission from such a cavity is possible if the modal gain overcomes the threshold value:

$$g_{\text{th}} = \alpha_r + \alpha_w + \alpha_s, \quad (2.9)$$

with the losses in reflection (α_r), waveguiding (α_w), and scattering (α_s). The reflection losses, in turn, can be calculated from the reflectivities R_1 and R_2 at both cavity end facets and the cavity (nanowire) length L :

$$\alpha_r = \frac{1}{2L} \ln \frac{1}{R_1 R_2}. \quad (2.10)$$

Threshold characteristics of multimode lasers A basic feature of laser emission is the excitation power dependence of its output power. Commonly, the onset of lasing is accompanied by an abrupt raise in output intensity. In semiconductor lasers, however, this transition can become less distinct due to the strong spontaneous emission. To

address this quantitatively, rate equations of 4-level (or 3-level) laser systems can be solved analytically. Casperson et al. used a multimode laser model with a set of coupled rate equations to calculate analytical expressions describing the total power output for a homogeneously broadened laser [201]. Casperson's model will be used in this thesis to fit the power dependent lasing characteristics. It gives an explicit expression for the multimode output power

$$x_t = \frac{r(1+x)^{-1}x_0}{[1-r(1+x)^{-1}]^{1/2}}, \quad (2.11)$$

where r is the ratio of the round trip-gain to the round-trip cavity loss (abbreviated as gain/loss throughout this thesis) and x_0 gives the spontaneous emission input into the laser modes (see figure 2.3c). The parameter x is calculated from

$$x = x_0 \left(\sqrt{\frac{1+x}{1+x-r}} - 1 \right), \quad (2.12)$$

in case the mode spacing is smaller than the transition linewidth (which is true for most semiconductor lasers). For a spontaneous emission parameter $x_0 = 1$, the laser characteristic appears "thresholdless" (see figure 2.3c). For typical semiconductor lasers, however, x_0 is much less than 1 and the transition from spontaneous to stimulated transition—the amplified spontaneous emission—is accompanied by a steeper slope around the lasing threshold (where to gain-to-loss ratio is 1).

2.4. X-ray matter interaction

X-rays that interact with matter are either absorbed or scattered, while non-interacting X-rays are transmitted. The absorption coefficient follows the Lambert-Beer law [202, 203]:

$$I(d) = I_0 \cdot \exp[-d \cdot \mu(E)], \quad (2.13)$$

with the initial intensity I_0 , the penetration depth d , and the energy dependent X-ray absorption coefficient $\mu(E)$. The energy that X-rays typically carry allows them to excite a core electron via the photoelectric effect leaving a core hole behind (see figure

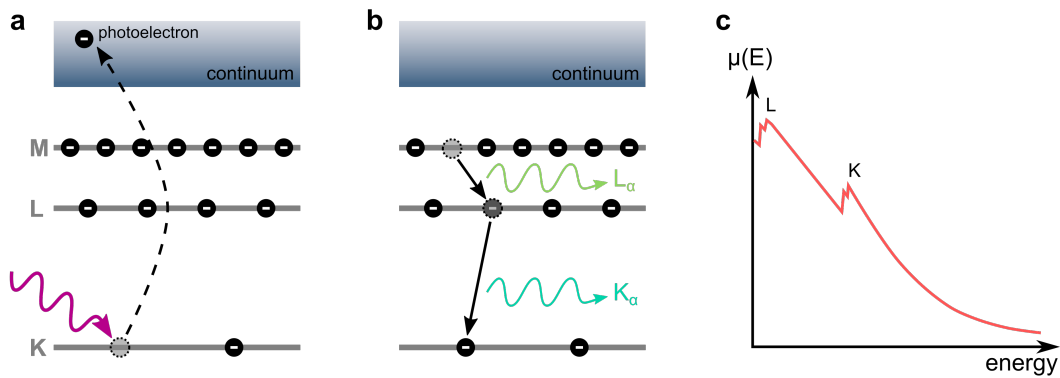


Figure 2.4.: X-ray matter interaction. **a** Scheme of the X-ray excitation process. An incident high-energy X-ray excites a core-electron to the continuum leaving a core-hole behind. **b** Scheme of the subsequent radiative recombination process resulting in L and K-shell X-ray fluorescence. Besides the radiative processes, Auger recombination also allows for a carrier recombination (not shown here). **c** Schematic representation of the X-ray absorption coefficient $\mu(E)$ as a function of energy along the L and K absorption edge.

2.4a). Depending mostly on the element's atomic number Z , the core hole is filled with electrons from outer shells either by emitting characteristic X-rays (dominant for high Z) or by the ejection of Auger electrons (dominant for low Z) [204].

2.4.1. X-ray fluorescence

The energy of the emitted X-ray created upon filling the core hole amounts to the energy difference between the two levels; therefore, different elements reveal distinct characteristic emission energies (see figure 2.4a and b). Hence, the X-ray fluorescence (XRF) signal allows to draw conclusions about the sample composition. In GaAs, the K_{α} emission line of Ga is at 9.251 keV and that of As at 10.544 keV. Fluorescence energies of further transitions are summarized in the X-ray data booklet [205].

2.4.2. X-ray absorption near edge structure spectroscopy

X-ray absorption spectroscopy, in general, is based on analyzing the energy dependent X-ray absorption coefficient $\mu(E)$ as a function of energy [206, 207]. While $\mu(E)$ is mostly monotonically decreasing with increasing X-ray energy, there is a steep increase

if the excitation energy surpasses the electron binding energy of a specific shell (see figure 2.4c). In the monotonically decreasing sections $\mu(E)$ can be approximated by [207]:

$$\mu(E) = \frac{\rho Z^4}{AE^3}, \quad (2.14)$$

where ρ is the sample density, Z the atomic number, and A the atomic mass. When $\mu(E)$ is measured a few tens of eV around such an absorption edge, this is referred to as X-ray absorption near edge structure (XANES) spectroscopy [207, 208]. The XANES signal is extremely sensitive to changes in coordination, oxidation state, and bond length [209–213].

2.4.3. X-ray beam induced current

Beyond the XRF mechanism, there is a more complex cascade of processes that, among other processes, give rise to the X-ray beam induced current (XBIC) [214]. After the initial excitation process leaves a core hole, this hole is immediately filled with an electron from the next higher shells via the Auger or XRF process. This process, however yields further core-holes in these shells that are in turn filled with electrons from higher shells resulting in a recombination cascade [215]. Furthermore, the highly energetic Auger electrons and photoelectrons thermalize in the surrounding material via inelastic scattering; this creates even more electrons (holes) that—in semiconductors—finally thermalize to the bottom of the conduction (the top of the valence) band [216, 217]. If this process happens in the vicinity of an electrical field (such as the internal electrical field of a p-n junction), the carriers can be separated, transported to the contacts, and finally measured as the XBIC signal [214].

2.5. Semiconductor nanowires

A semiconductor nanowire combines semiconducting properties with a high aspect ratio cylindrical structure. Optical and electrical properties of nanowires are strongly

influenced by their surface, as they exhibit a huge surface-to-volume ratio due to the nanoscale diameter. Therefore, the nanowire geometry will be considered in the following topics of interest for this thesis.

2.5.1. Nanowire diodes

Diodes are central building blocks in electronic circuits. They are created by forming a junction between n- and p-type material. In thermal equilibrium, the Fermi levels align and valence and conduction bands shift and bend accordingly (see figure 2.5a). The resulting built-in electric field leads to the formation of a depletion region around the junction, with a spatial extent in the n- and p-type region of [218]

$$d_n = \sqrt{\frac{2\epsilon\epsilon_0 V_b}{e} \frac{N_A/N_D}{N_A + N_D}}, \quad (2.15)$$

$$d_p = \sqrt{\frac{2\epsilon\epsilon_0 V_b}{e} \frac{N_D/N_A}{N_A + N_D}}, \quad (2.16)$$

with the semiconductor dielectric permittivity ϵ , the vacuum permittivity ϵ_0 , the fundamental charge e , the built-in voltage V_b , and the acceptor (donator) concentration N_A (N_D).

Electron-hole pairs that are generated in the depletion region are separated and can be measured as a current (see figure 2.5b). The diffusion length of the minority carriers is given by [219]

$$L_i = \sqrt{\tau_i D_i}, \quad (2.17)$$

with carrier lifetimes τ_i and diffusion coefficients D_i , for electrons and holes, respectively. The diffusion coefficient is related to the mobility μ by the Einstein equation:

$$D = \mu \frac{kT}{q}, \quad (2.18)$$

where k is the Boltzmann constant, T the temperature and q the electric charge. In nanowires, surface recombination must be included in these considerations due to the

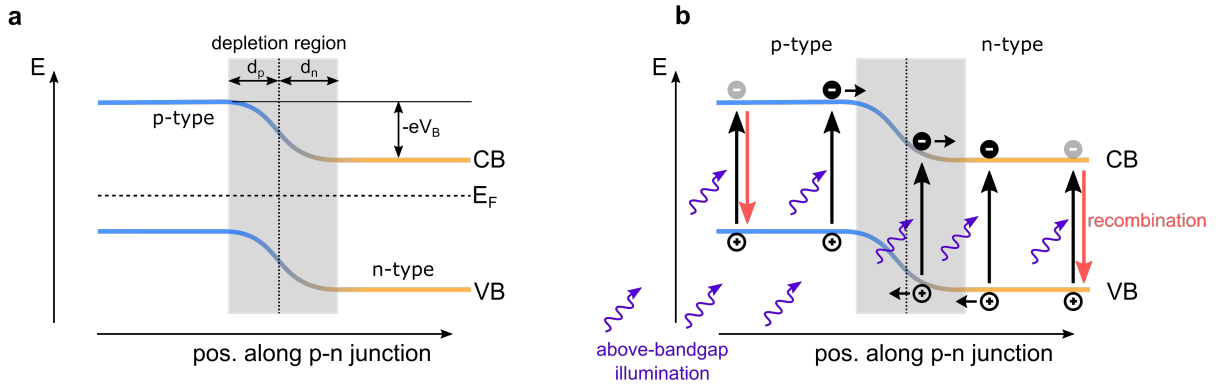


Figure 2.5.: P-n junction band diagrams. **a** Schematic band diagram along a p-n junction. Due to the alignment of the Fermi levels in the p- and n-type regions (dashed line), a depletion zone forms with a spatial extend $d = d_p + d_n$ as marked in gray. The resulting built-in voltage V_B is marked. **b** Schematic band diagram along a p-n junction under above-bandgap illumination. Electron-hole pairs generated within the depletion region (marked gray) can be separated. Electrons (holes) drift towards the n-type (p-type) section, as indicated by the black horizontal arrows. If not separated, electron-hole pairs will recombine (red arrows).

huge surface-to-volume ratio. Therefore, the lifetime τ in equation 2.17 is replaced by an effective lifetime τ^* that can be calculated from the bulk lifetime τ_b , the surface recombination velocity, and the nanowire diameter d [220]:

$$\frac{1}{\tau_i^*} = \frac{1}{\tau_b} + \frac{4S}{d}. \quad (2.19)$$

2.5.2. Band bending in ZnO nanowires

The surface is a strong perturbation of the crystal symmetry resulting in surface states. In nanowires the surface plays an even more preminent role due to the huge surface-to-volume ratio. Dangling bonds (i.e., unpaired electrons) at the surface form energy states located in the band gap [221]. In an n-type semiconductor such as ZnO, the Fermi energy alignment yields an upwards band bending towards the surface. This implies a surface potential

$$\Phi = \frac{e^2 N_s^2}{2\epsilon\epsilon_0 N'} \quad (2.20)$$

with the semiconductor dielectric permittivity ϵ , the vacuum permittivity ϵ_0 , the fundamental charge e , the electron density N , and the surface state density N_s . This leads to an electron depletion near the surface, with a spatial extent d , and an accumulation

in the "bulk" part of the nanowire, where the bands are flat (see figure 2.6a). Vice versa, holes will accumulate at the surface [222]. The spatial extent of the depletion region can be calculated by

$$d = \sqrt{\frac{2\epsilon\epsilon_0\Phi}{e^2N}}. \quad (2.21)$$

As the density of states at the surface is usually several orders of magnitude larger than in the bulk, the position of the Fermi energy is determined almost exclusively by the surface. This is generally referred to as Fermi level pinning, implying that the Fermi energy is pinned to the surface. The surface band bending plays a crucial role for the electrical and optical properties of nanostructures. It strongly affects the photoluminescence due to the spatial separation of created electron-hole pairs. Furthermore, the activation of indirect transitions in the surface depletion region was reported in reference [223]. Band bending is strongly influenced by the nanowire diameter, doping level, and its surface roughness [222, 224–227]. But also the ambient plays a crucial role, as the adsorption of molecules affects the band bending [221, 228].

Surface adsorption Molecules that adsorb to the surface alter the band bending due to an electron transfer. Acceptors like O_2 that physisorb to the surface will capture free electrons, thus increase the band bending, and finally bind more tightly (i.e., get chemisorbed) [57, 229]. This leads to an increasing extent of the depletion zone leaving a decreasing conductive channel in the core and therefore a reduced conductivity (see figure 2.6a). Donator molecules like NH_3 release electrons to the conduction band leading to a decrease of the band bending [221].

The prevailing species found at the surface of ZnO are oxygen-related ones, such as O^- , O_2^- and OH^- [109, 230–234]. As the electrical conductance of the nanowire is dependent on the band bending, the change of band bending upon molecule adsorption allows for gas sensing using ZnO nanowires [57, 231, 235]. Mostly, the target gas reacts with surface oxygen species and thus induces their desorption [229, 235]. Since a connection between V_O and gas sensitivity was hinted in several studies, V_O might be a preferential surface species adsorption site [235, 236].

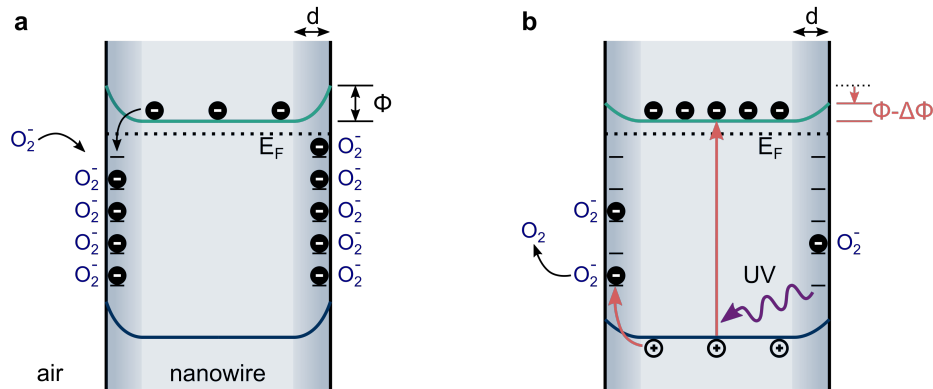


Figure 2.6.: Surface band bending. **a** Sketch of the energy bands of a ZnO nanowire in air. Electrons from the conduction band are trapped at the surface by adsorbed O_2 leading to a surface band bending with the surface potential Φ . **b** Energy bands of a ZnO nanowire upon above-bandgap illumination. The hole-assisted surface species desorption process leads to a reduction of the surface band bending.

Stimulated desorption and persistent photoconductivity Upon exciting an electron from the valence to the conduction band, the residual hole is likely to migrate towards the surface due to the surface potential (see figure 2.6b). There, it can recombine with a trapped electron inducing the desorption of the respective surface species [229, 237]. This process thus results in the decrease of the surface band bending and leaves the generated electron in the conduction band with a prolonged lifetime. In other words, there is an increase in density of conduction band electrons as well as an increase of the width of the non-depleted bulk region of the nanowire. As a result, a high photoconductivity can be measured in ZnO [63, 238]. Performing these experiments in vacuum furthermore prevents the re-adsorption of O_2 at the surface yielding a persistent photoconductivity [239]. Exposure to air leads to a decay of conductivity within seconds [62, 63, 240–242] to minutes [238, 243].

Furthermore this implies that the surface band bending leads to a photoluminescence quenching as it spatially separates the charge carriers preventing radiative recombination. Lowering the band bending by the desorption of surface species is thus expected to increase the photoluminescence; this was confirmed by the observation of an increase in near band edge emission when moving a ZnO nanoparticle thin film from air to vacuum and vice versa [244, 245]. The photo-response is strongly dependent on the excitation conditions, especially the interaction depth [246]. Additionally, the excitation power plays a role for above-bandgap photoexcitation [247].

2.5.3. Defects and defect luminescence in ZnO

Many theoretical studies explored the formation of point defects and defect clusters in ZnO by density functional theory (DFT) simulations. The most common defects that are potential candidates for the luminescence observed in the visible spectral regime—the defect luminescence—will be addressed in this section. There is a number of intrinsic defects in ZnO that can give rise to mid-gap states yielding optical transitions, which span a broad wavelength range in the visible. From DFT simulations the most common defects (i.e., those with the lowest formation energies) are known to be oxygen vacancies (V_O) and zinc vacancies (V_{Zn}). The next highest formation energies are that of the Zn interstitial (Zn_i) and the (Zn_O) antisite. At even higher formation energies—and thus unlikely to form—are oxygen interstitials (O_i) and (O_{Zn}) antisites. While most calculations agree well on this qualitative order, quantitative conclusions about energy levels are more difficult to achieve due to the derivative discontinuity that results in the generic band gap prediction weakness of DFT [248].

Assigning point defects to the different defect-related luminescence bands in ZnO (see chapter 2.3.2) proved challenging in the last decades and lead to a wide range of contradicting claims [164–169, 249–258]. Their local origin, however, was recently reported more conclusively: High resolution CL spectra of ZnO nanowires revealed that the NBE signal was mostly emitted along the central axis, while blue, green, and orange luminescence were mostly emitted at the surface. The red luminescence originated from all regions of the nanowire [259, 260]. These ascriptions were corroborated by other studies, where capping layers were shown to reduce surface-related emission lines [261–263].

In nanowires, surface defects and defect in the vicinity of the surface are prominent due to the huge surface-to-volume-ratio. Still, the occurring defects are in principle the same as in bulk material. In the following, the most prominent defects in ZnO are introduced.

Hydrogen Hydrogen can occupy several different positions in ZnO. While the thermal stability of interstitial H_i is low due to its small migration energy of 0.4 eV to 0.5 eV [264], there are configurations that are stable even at elevated temperatures: substitutional

hydrogen (H_O) was reported to be a thermally stable shallow donor with a migration energy of 1.7 eV, and Zn vacancy-hydrogen defect complexes $V_{Zn-n}\cdot H$ (with $n = 1 \dots 4$) were reported to be stable with electrical properties depending on n [165, 264–266] (hydrogen-based complexes with V_O and V_{Zn} will be addressed in the following sections). Hydrogen also might play a role in the stabilization of other defects such as Cu_{Zn} and Li_{Zn} [267, 268]. In several studies, a correlation between hydrogen content and resistivity was found. A decrease in resistivity was observed when increasing the H concentration during growth [269] or by H plasma treatment [173]. This is in excellent agreement with DFT calculations showing that hydrogen is a shallow donor in ZnO [270, 271]. Hydrogen is commonly assumed to be the source of the intrinsic n-type conductivity of ZnO [270, 272, 273], since it is present in almost all growth processes (unlike other shallow donors such as B, Ga, or Al) and has an exceptionally high diffusivity [274–276]. Additionally, hydrogen can passivate active recombination centers such that hydrogen incorporation into ZnO yielded increases in the NBE and lowered stimulated emission thresholds [277–279]. Due to acceptor compensation, hydrogen was also reported to contribute to the difficulty for stable p-type doping in ZnO [280].

Zinc vacancies Several recent publications stress the role of V_{Zn} and their complexes as the most important defect states in ZnO [165, 266, 281]. Commonly, V_{Zn} were assigned a main source for the defect luminescence with contrasting views on emission wavelength: bands originating from V_{Zn} were observed in the blue [254, 282], green [164, 167, 283, 284], or red [260]. Recent DFT calculations, however, assign V_{Zn} to non-radiative transitions with energies in the infrared [285, 286]; this is in agreement with experimental studies [153, 165, 281]. In contrast, $V_{Zn-n}\cdot H$ complexes were shown to give rise to radiative transitions that are commonly named as source of the red luminescence [165, 281]. The defect clusters' electrical properties depend on n : for $n = 1$ it is a single acceptor, for $n = 2$ it is neutral, and for $n = 3$ and $n = 4$ it is a single and double donator, respectively. Remarkably, $V_{Zn}\cdot H$ and $V_{Zn-2}\cdot H$ complexes were reported to have binding energies around 2 eV to 3 eV; thus, they were predicted to be stable up to 1200 °C. This prediction was corroborated experimentally by nuclear reaction analysis [287]. Meanwhile, $V_{Zn-4}\cdot H$ was predicted to have high formation

energies while contrasting results were obtained for $V_{\text{Zn}}-3\cdot\text{H}$ [267, 268, 280, 286, 288].

Oxygen vacancies From first-principles calculations V_{O} is known to be a deep donor state (~ 1 eV above the valence band maximum) [177, 289, 290]. Despite occasional reports claiming that V_{O} is responsible for the unintentional n-type doping in ZnO [291], there is a broad consensus that V_{O} is a deep donor and cannot cause the n-type doping [266, 292–297]. Despite being regarded as the major defect in ZnO in many studies, the formation energy of V_{O} is high under n-type conditions (which are almost always present in ZnO) [266]. In O-rich conditions, V_{O} barely forms and V_{Zn} is the dominant defect, while in Zn-rich conditions both are expected due to similar formation energies. At the surface of ZnO, the formation energy of V_{O} was reported to be drastically lowered [298]; due to the huge-surface-to-volume ratio, surface-near V_{O} might be a dominant defect in ZnO nanowires [299, 300]. This agrees with reports that link V_{O} to a role in the processes for gas sensing and persistent photoconductivity [235]. Additionally, (surface) V_{O} was frequently assigned as a source of a green luminescence band around ~ 500 nm [166, 167, 252, 301]. An oxygen vacancy occupied by a hydrogen atom (H_{O}) is, together with the $V_{\text{Zn}}-n\cdot\text{H}$ complex, the most frequent and stable hydrogen configuration in ZnO [281]. Its formation energy is similar to that of H_{O} [294] and it was reported to be stable upon annealing up to 800 °C [140, 302]. As H_{O} is a shallow donor, it is a probable candidate for the intrinsic n-type doping of ZnO [294].

Zn interstitials If ZnO is grown under extremely Zn-rich growth conditions, Zn_i have a sufficiently low formation energy to be formed [249, 266]. They were ascribed to optical transitions in the blue [303] and are shallow donors. However, Zn_i are unstable at room temperature and thus cannot account for stable emission lines or n-type conductivity [249, 304].

3. Experimental methods

The experimental methods that were used within this thesis are summarized within this section. If not stated otherwise, measurements were conducted at the Institute for Solid State Physics at the Friedrich Schiller University Jena.

3.1. Nanowire growth

The nanowires investigated within this thesis were grown via chemical vapor deposition using the vapor liquid solid (VLS) method as described by Wagner and Ellis in 1964 for Si whiskers [305] and established as a technique to grow nanoscale-sized semiconductors in the 1990s [306–308].¹ The process relies on a liquid metal catalyst—i.e., a metal heated above its melting point—that allows for the rapid adsorption of the vaporized growth material resulting in the growth of quasi-one-dimensional structures [310].

3.1.1. Growth of ZnO and CdS nanowires

Nanowires of ZnO and CdS were grown in a horizontal tube furnace. For the growth of ZnO nanowires, the source material powder was mixed with graphite powder with a molar ratio of 1:1 to reduce the sublimation point of ZnO via to the carbothermal reduction process [311], while pure CdS powder was used for growing CdS nanowires. The source material (ZnO with graphite or CdS) was then evaporated at 1050 °C (800 °C)

¹The VLS process was also found to occur in nature resulting in germanium sulfide microwires [309].

for ZnO (CdS). Argon was used as an inert carrier gas to transport the growth material vapor to the growth substrates, which were kept downstream at a lower temperature (900 °C to 1000 °C for ZnO and 700 °C to 800 °C for CdS). During the growth of ZnO nanowires, O₂ was added to the Ar carrier gas to improve the stoichiometry.

A thin metal layer (10 nm of Au) was deposited onto the Si growth substrates prior to the growth. The film melts upon heating the substrate and forms nanometer-sized droplets. The liquid Au catalyst acts as a preferential adsorption site for the CdS (ZnO) vapor and an eutectic solution is formed. A continuous supply of growth material vapor leads to a supersaturation in the catalyst causing the material to precipitate beneath the catalyst droplet. This, in turn, enables solid crystal growth and the formation of CdS (ZnO) nanowires with diameters determined by the catalyst particle size [32].

One of the major advantages of the VLS technique is the high growth rate of up to $\mu\text{m min}^{-1}$ compared to a much lower growth rate of the vapor solid (VS) growth (nm min^{-1}) that occurs at high growth temperatures [312]. The high growth rates of the VLS process enables high aspect ratio structures, while for longer growth times also tapered nanowires and nanosails form via VS growth [136, 313]. The VLS grown nanowires investigated within this thesis cover lengths of 5 μm to 30 μm with diameters of 150 nm to 500 nm for ZnO and lengths of 5 μm to 40 μm with diameters ranging from 200 nm to 800 nm for CdS. Details on the growth of ZnO nanowires are provided in references [314, 315] and details on the growth of CdS nanowires can be found in reference [316].

3.1.2. Growth of axial GaAs nanowires

The axial GaAs p-n junction nanowires investigated in this thesis were grown via VLS growth in an AIX200 RF metal organic vapor phase epitaxy (MOVPE) reactor by Lisa Liborius in the group of Dr. Werner Prost at the University of Duisburg-Essen. Prior to the growth, periodically structures of Au catalysts were deposited on a (111)B GaAs:Zn substate via nanoimprint lithography. The mask was hexagonally structured with a hole diameter of 400 nm and a pitch of 2.5 μm . Subsequently, 22 nm of Au was evaporated under an angle of 25°.

The MOVPE reactor was heated to 450 °C at a reactor pressure of 50 mbar and a total flow of 3400 mL/min from a steady supply of tertiarybutylarsine (TBAs; 0.05 mmol/min) to prevent the desorption of As from the substrate and allow the eutectic formation from the Au catalyst. The Au eutectic was subsequently presaturated with the Zn-dopant by supplying diethylzinc (DEZn) for 4 min. Next, the nanowire base was grown for 3 min supplying the precursors TBAs and trimethylgallium (TMGa) at a V/III ratio of 2.5 and DEZn at a II/III ratio of 0.004. After completing the base growth, the reactor temperature was reduced to 400 °C for growing the p-type segment (for 30 min) using the same precursors and flows. For growing the n-type segment, the dopant precursor was then switched to tetraethyltin (TESn) using a IV/III ratio of 0.1. The resulting axial p-n junction nanowires had lengths up to 20 μm with diameters ranging from 100 nm to 200 nm.

3.1.3. Nanowire transfer and device fabrication

The VLS grown nanowires were densely packed on the substrate after the growth with random orientation for the CdS and ZnO nanowires and standing upright for the GaAs axial p-n junction wires. For optical experiments as well as electrical contacting, nanowires were transferred to a clean substrate such that individual nanowires could be identified. A dry imprint technique was used for CdS and ZnO nanowires: The nanowire growth substrate was gently rubbed onto a clean target substrate until the desired density of transferred nanowires was reached. While this mechanical method might lead to low levels of stress in the nanowires [317], it avoids any surface alteration as no chemicals are needed in the process. As a target substrate, a Si substrate with a thermally grown SiO₂ layer (1.5 μm) was chosen, as a low refractive index is needed to enable efficient waveguiding of the photonic mode.

The GaAs nanowires were scraped off the growth substrate into a beaker with 2-propanol. The dispersed nanowires were transferred onto a clean Si/SiO₂ substrate using a pipette. After the 2-propanol was evaporated, the nanowires were randomly distributed on the insulating substrate. Electrical contacts were then defined using electron beam lithography and physical vapor deposition. Different metallization stacks

were deposited on the p- and n-type sides to enable ohmic contacts: Pt/Ti/Pt/Au (5/10/10/400 nm) on the p-side and Ge/Ni/Ge/Au (2/20/50/400 nm) on the n-side. Ohmic contacts were finally formed after annealing for 30 s at a temperature of 280 °C in a rapid thermal annealing setup under nitrogen atmosphere.

To prevent damage during the subsequent macroscopic contacting, the two contacts of each nanowire were short-circuited by thin metal lines defined by electron beam lithography. The individual nanowire devices were then contacted via wire bonding. Finally, the metal short-circuit lines were scraped to enable electrical measurements.

3.2. Electron microscope-based characterization

3.2.1. Scanning electron microscopy

The morphology of nanowires cannot be accessed by optical microscopy as their diameters are typically below the Abbe resolution limit. Scanning electron microscopy (SEM) was used within this thesis to characterize the nanowire morphology. The electron beam of a FEI DualBam Helios NanoLab 600i system was used allowing for high resolution SEM with a maximum energy of 30 keV and a maximum current of 22 nA. This enables lateral resolutions down to ~ 1 nm.

Further on, a JEOL-6490 SEM with a LaB₆ electron gun was employed with a maximal energy of 30 keV and beam currents between 1 pA and 100 nA enabling a lateral resolution down to 10 nm. Detailed information about electron microscopy can be found in references [318, 319].

3.2.2. Energy-dispersive X-ray spectroscopy

In energy-dispersive X-ray spectroscopy (EDX), characteristic X-rays—emitted from core electrons excited by the electron beam of an SEM—are measured as a function of their energy. The characteristic X-ray intensity of the matrix elements of nanowires was investigated using the electron beam of the FEI DualBam Helios NanoLab 600i

FIB system equipped with a Peltier-cooled, large area silicon drift detector (Oxford Instruments X-Max^N) with a detection limit below 1 at.% depending on the electron energy and the investigated element. Data analysis was performed using the commercial software package AZtec provided by Oxford Instruments. Detailed information about EDX can be found in references [319, 320].

3.3. Optical characterization

3.3.1. Photoluminescence

In photoluminescence (PL) spectroscopy, the sample is illuminated with a monochromatic light source—typically a laser—and the samples' luminescence is collected. Micro-photoluminescence spectroscopy was measured in a home-built epifluorescence microscope setup installed by Dr. Sebastian Geburt [316], as sketched in figure 3.1. All PL measurements were performed at ambient conditions and room temperature unless specifically stated. A frequency-tripled Innolas Spitlight Nd:YAG laser was used as excitation laser for lasing measurements, emitting at 355 nm with a repetition rate of 100 Hz and a pulse duration of 10 ns. A cw Kimmon HeCd laser, emitting at a wavelength of 325 nm, was used for micro PL and waveguiding measurements. The laser beam was guided through a Pellin-Broca prism, where the light was dispersed such that the central laser wavelength was reflected at 90°; disturbing sidebands were reflected at deviating angles such that they are blocked by a pinhole after the prism. Neutral density filters were used to attenuated the laser beam to the desired power. A fraction of the laser beam was reflected by a beam splitter to permanently monitor the power with a Si photodiode (Thorlabs S130VC) or a thermopile sensor (Thorlabs S302C).

The laser beam was then directed via a second beam splitter to a refractive long working distance 50x objective (Sigmakoki PAL-50-NUV-A or PFL-50-UV-AG) with a numerical aperture of 0.45 or 0.42 where the light was focused to a spot size of 1 μm onto the sample. A lens was added into the beam path before the objective to enlarge the spot on the sample up to 30 μm to provide nearly homogeneous pumping for lasing

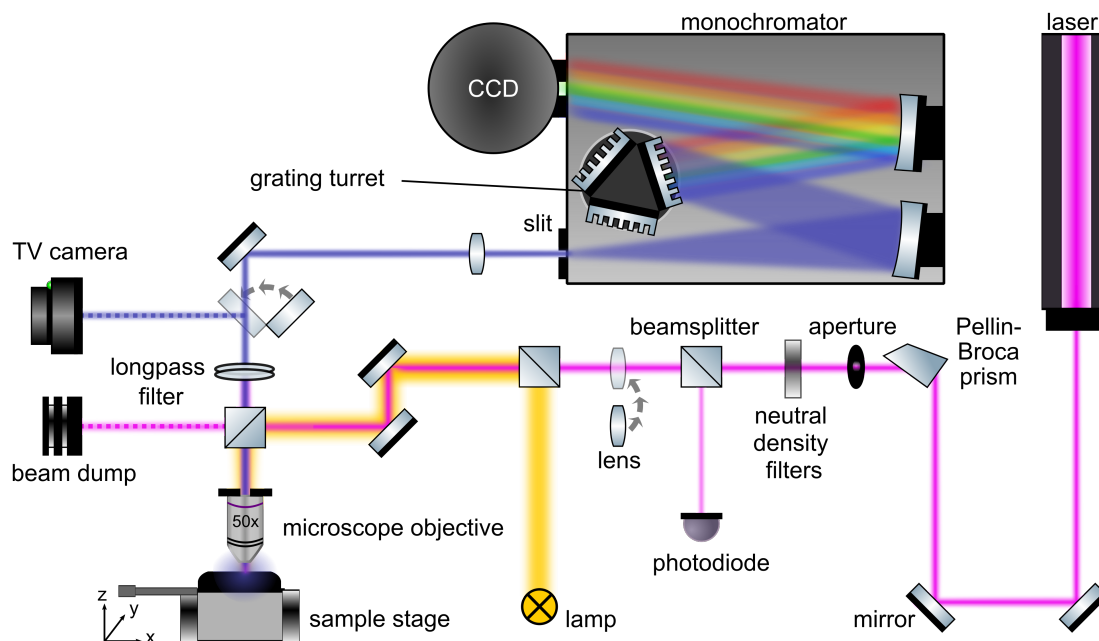


Figure 3.1.: Micro photoluminescence setup. The excitation laser was guided to a 50x microscope objective where it was focused onto the sample. The fluorescence light was collected with the same objective and guided to the monochromator. Microscopic observation was enabled by coupling white light into the beam path and imaging with a TV camera.

measurements. For microscopical sample observation, white light was coupled into the beam path and guided through the objective for sample illumination. The sample was mounted on an xyz-translation stage. Coarse positioning of the samples was enabled by manual differential drives, while fine positioning was enabled by piezoelectric actuators mounted at all 3 axis controlled with a 150 V closed-loop piezo controller (Thorlabs BPC303). For low-temperature measurements down to temperatures of ~ 4 K, the samples were placed in a liquid He flow cryostat (Janis ST-500). The fluorescence light was collected by the objective and passed through a longpass filter that attenuated the reflected excitation laser. A mirror was flipped into the beam path to guide the luminescence and the reflected white light to a TV camera for microscopic brightfield or luminescence observation. For spectroscopy, the light was directed to the entrance slit of a Czerny-Turner imaging monochromator (Princeton Instruments SP-2500i, $f/6.5$). Here, the light was directed to a grating mounted on a grating turret equipped with 3 different gratings (12001/mm - blaze 300 nm, 4001/mm - blaze 550 nm, and 1501/mm - blaze 500 nm), where the light was dispersed and finally detected in a front-illuminated charge coupled device (CCD) camera (Princeton 10:256E/LN, open electrode chip). More details on the PL setup are given in reference [316].

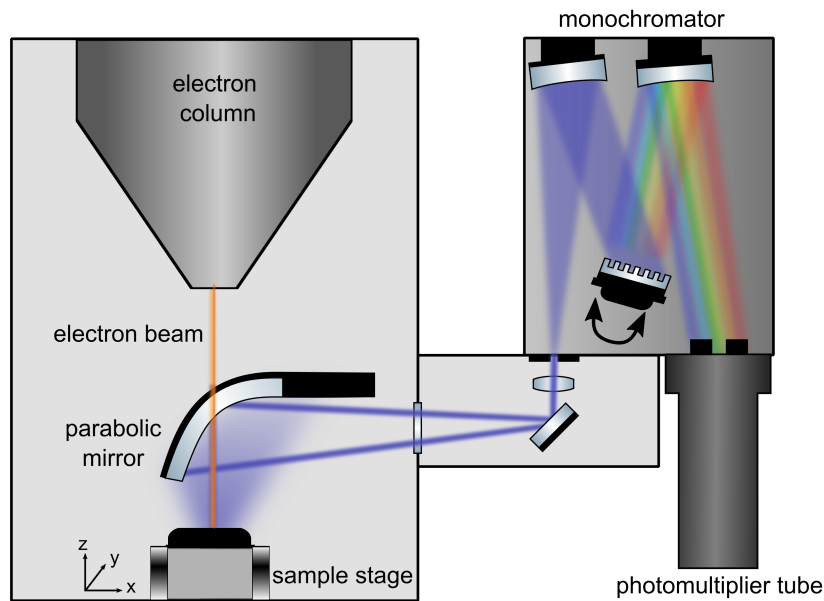


Figure 3.2.: Cathodoluminescence setup. The focused electron beam of the JEOL-6490 SEM was used to excite the sample locally. The luminescence light was collected globally by a parabolic mirror, which was positioned above the sample (the mirror was aligned such that the electron beam can pass through a hole in the mirror).

3.3.2. Cathodoluminescence

Cathodoluminescence (CL) measurements were performed using the JEOL-6490 SEM equipped with a GATAN MonoCL3+ recording system. A parabolic mirror was used to collect the CL created during focused electron beam irradiation, as schematically shown in figure 3.2. Therefore, despite the local excitation, the light collection in CL was global, in contrast to the local light collection in micro PL. Via a further mirror, the light was directed to the entrance slit of a 300 mm Czerny-Turner type monochromator. A 1200 l/mm (VIS) grating was used to disperse the light which was finally focused to the exit slit of the monochromator; spectra were acquired serially with a Peltier-cooled photomultiplier detector optimized for the visible regime (Hamamatsu R943) with step sizes of 1 nm to 5 nm. Further details on the CL setup are given in reference [316].

Electron irradiation Nanowires were irradiated with the electron beam to investigate electron-beam induced effects using the JEOL-6490 and the electron beam of the FEI DualBam Helios NanoLab 600i as introduced in section 3.2.1. For CL, PL, and

waveguiding experiments, about 40 % of the respective individual nanowire was irradiated, while the rest remained pristine and served as a reference. For lasing measurements, the full length of the nanowire was irradiated, respectively. Similar, neighboring nanowires were used as references in this case.

In the JEOL-6490, nanowires were irradiated using acceleration voltages of 10 keV to 30 keV and currents between 0.3 nA to 3.3 nA with a magnification of 10000x, which was equivalent to a horizontal field width² of 13.25 μm . In the FEI DualBam Helios NanoLab 600i, an acceleration voltage of 10 keV was used with currents of 21 pA at a horizontal field width of 12.8 μm . In both microscopes, irradiation times were varied between 30 s and 90 min. It should be noted, however, that also before the start of the controlled irradiation, the nanowire was exposed to a certain (but comparatively low) electron dose during the focusing procedure in the SEM.

3.4. X-ray analytical methods

The different synchrotron-based techniques used throughout this thesis were conducted at the nano-analysis beamline ID16B of the European Synchrotron Radiation Facility (ESRF) in Grenoble [322]. The electron beam was delivered in the 7/8+1 filling mode, where a train of 868 bunches (filling 7/8 of the storage ring circumference) is combined with a single bunch (in the remaining (1/8) of the storage ring), yielding an X-ray flux of 2×10^8 ph/s and a pulse width of ~ 20 ps. The X-ray beam provided by the undulator was focused using a pair of Kirkpatrick-Baez multilayer-coated Si mirrors, which enabled a beam size of $80 \text{ nm} \times 90 \text{ nm}$. The monochromatic beam mode was used ($\Delta E/E = 10^{-4}$)[322], and all synchrotron-based methods were recorded at room temperature in ambient air.

²The horizontal field width is the length of the horizontal field of view at a given magnification [321].

3.4.1. X-ray fluorescence

The X-ray fluorescence (XRF) was detected by a 7-element Si drift detector positioned at an angle of 35° with respect to the sample plane. The sample was raster scanned through the X-ray beam and an XRF spectrum was recorded at each position. Each spectrum was individually fitted using the software package PyMCA [323] to determine the spatially resolved elemental intensity. In this way, XRF maps were recorded. High-resolution maps were recorded in selected regions of interest using a scan area of $1.3\ \mu\text{m} \times 1.5\ \mu\text{m}$, a pixel size of 20 nm, and an integration time of 200 ms per pixel.

3.4.2. X-ray beam induced current

Simultaneous to the XRF maps, the X-ray beam induced current (XBIC) signal was recorded at each position while scanning the sample through the X-ray beam. The XBIC signal of the electrically contacted sample was detected using an EG&G 7280 DSP lock-in amplifier, such that finally an XBIC map was recorded. Additionally, IV-curves were measured repeatedly to monitor the device operation.

3.4.3. X-ray absorption near edge spectroscopy

The energy of the incoming X-rays was varied using a Si (111) double crystal monochromator. This enabled an energy resolution of ~ 1 eV. In this way, XRF (for the in-operando measurements, simultaneously also XBIC) was measured as a function of incident X-ray energy around the Ga K-edge, yielding X-ray absorption near edge spectra (XANES). If not stated in detail, the XANES spectra were normalized to the post-edge spectral region. Details about XANES data evaluation can be found in references [208, 324].

4. An axial p-n junction nanowire X-ray detector at its limits

The core functionality of many nanowire-based devices such as solar cells or detectors lies in their p-n junction [42, 43, 69, 70]. For the future use of such nanowire pn-junction devices in real-world applications, key factors are device stability and reliability [28, 97, 98]. In this chapter, the operation of a single GaAs nanowire axial p-n junction is studied, aiming for the detection of hard X-rays. This nanowire X-ray detector enables high spatial resolutions compared to state of the art bulk indirect scintillation detectors, which are limited to the refraction limit [325], or direct pixel detectors that have typical pixel sizes of tens of microns [326]. A thorough in-operando characterization using nanoscale X-ray analytical techniques allows deep insights into the device operation and degradation mechanism.

The synthesis of the GaAs axial p-n nanowires, electrical contacting, and electrical pre-characterization was performed by Lisa Liberius within the group of Dr. Werner Prost at the Universität Duisburg-Essen. Nano-XRF, nano-XBIC and nano-XANES measurements were performed in collaboration with Dr. Maurizio Ritzer, Dr. Andreas Johannes, Dr. Martin Hafermann, Dr. Sven Schönherr, Dr. Jaime Segura-Ruiz (ESRF–The European Synchrotron), Dr. Damien Salomon (ESRF–The European Synchrotron), and Dr. Gema Martínez-Criado (Instituto de Ciencia de Materiales de Madrid). Parts of this chapter are published in reference [116].

4. An axial p-n junction nanowire X-ray detector at its limits

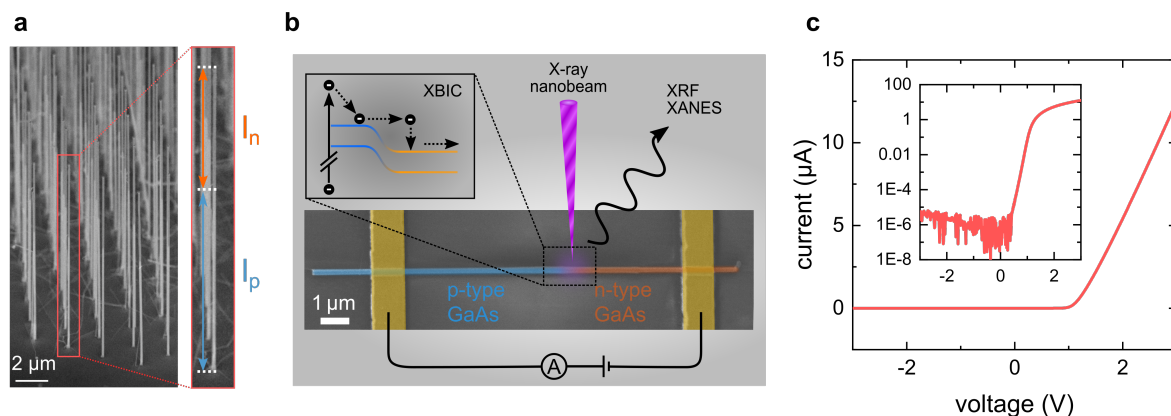


Figure 4.1.: Nanowire X-ray detector device. **a** SEM image of as-grown nanowires on the (111)B GaAs substrate. The n-doped part on top and the p-doped part at the bottom are marked in the inset. **b** Colorized SEM image depicting the nanowire device. An energy-tunable hard X-ray beam was tightly focused onto the GaAs nanowire with a p-n junction along the growth axis and a diameter of ~ 150 nm. The nanowire was contacted, which allowed for combined in-operando nano-XBIC (see inset), nano-XRF, and nano-XANES measurements while applying external voltages. **c** Current-voltage characteristic of an axial p-n junction nanowire. The inset shows the same data on a lin-log scale.

4.1. X-ray detection

4.1.1. Nanowire X-ray detector device

Axial p-n junction GaAs nanowires were grown by gold-catalyzed vapor-liquid-solid growth in a metal organic vapor phase epitaxy (MOVPE) reactor (see figure 4.1a). Doping was performed during growth by incorporating Zn and Sn for p and n-type, respectively (for details see chapter 3.1.2). The resulting doping concentrations were estimated by analyzing p-GaAs and n-GaAs nanowires, which were grown with the same growth parameters at the p and n-type sections in the p-n nanowires. By determining the path resistances of several nanowires via four point measurements, the doping concentrations were estimated to be $\sim 6 \times 10^{18} \text{ cm}^{-3}$ in both the p- and the n-type segment. Individual nanowires were transferred to a silica substrate and electrically contacted (for details see chapter 3.1.3) for the X-ray detection experiments (see figure 4.1b).

Prior to the X-ray analytical measurements, I-V curves of several individual nanowires were recorded to obtain the diode performance (see figure 4.1c). Ideality factors of 2 to 2.3 and reverse saturation current densities around $3 \mu\text{A cm}^{-2}$ were obtained for the

measured devices. The current was normalized to the respective cross-sectional area of the nanowire. Further I-V characterizations from more than 20 other nanowires from the same growth substrate yielded similar characteristics. No hints of degradation were observed—neither in the device performance nor in subsequent SEM images (not shown)—in any of the nanowire devices upon measuring these I-V characteristics repeatedly up to ± 5 V.

4.1.2. Detector performance

Electrons and holes that are generated by the X-ray beam in the depletion zone of the p-n junction can be separated by the internal electric field and can finally be measured as a current at the contacts (see chapter 2.4). If electron-hole pairs are generated far from the depletion zone they mostly recombine radiatively or non-radiatively. Thus, hard X-rays can be detected with extremely high spatial resolution that is determined by the length of the p-n junction depletion zone (together with the diffusion length) and the nanowire diameter. Finally, the convolution of the detector resolution and the spot size of the focused hard X-ray beam yields the XBIC signal (figure 4.2a and b). Remarkably, the direct imaging FWHM of the XBIC signal along the nanowire is only ~ 200 nm (figure 4.2c). Note that the spatial extent of the focused X-ray nanobeam is roughly $80 \text{ nm} \times 90 \text{ nm}$ and therefore considerably smaller than the detector resolution. Hence, it does not play a major role in broadening the width of the measured signal. But it is still included in the measured detector resolution and thus an upper bound is gained for the resolution directly obtained from the measurements. An even smaller FWHM of ~ 150 nm was measured perpendicular to the nanowire axis. This coincides well with the nanowire diameter of ~ 150 nm. Thus, by reducing the nanowire diameter and engineering the p-n junction, detector resolutions well below 100 nm are possible in direct scanning hard X-ray axial nanowire detectors.

There are only a few further reports about semiconductor nanowire-based hard X-ray detectors: There, nanowires offer an outstanding performance regarding XBIC efficiency and spatial resolution compared to their bulk counterparts [66, 217, 327, 328]. Using InP nanowires, however, a much higher spatial resolution of $0.51 \mu\text{m}$ was

4. An axial p-n junction nanowire X-ray detector at its limits

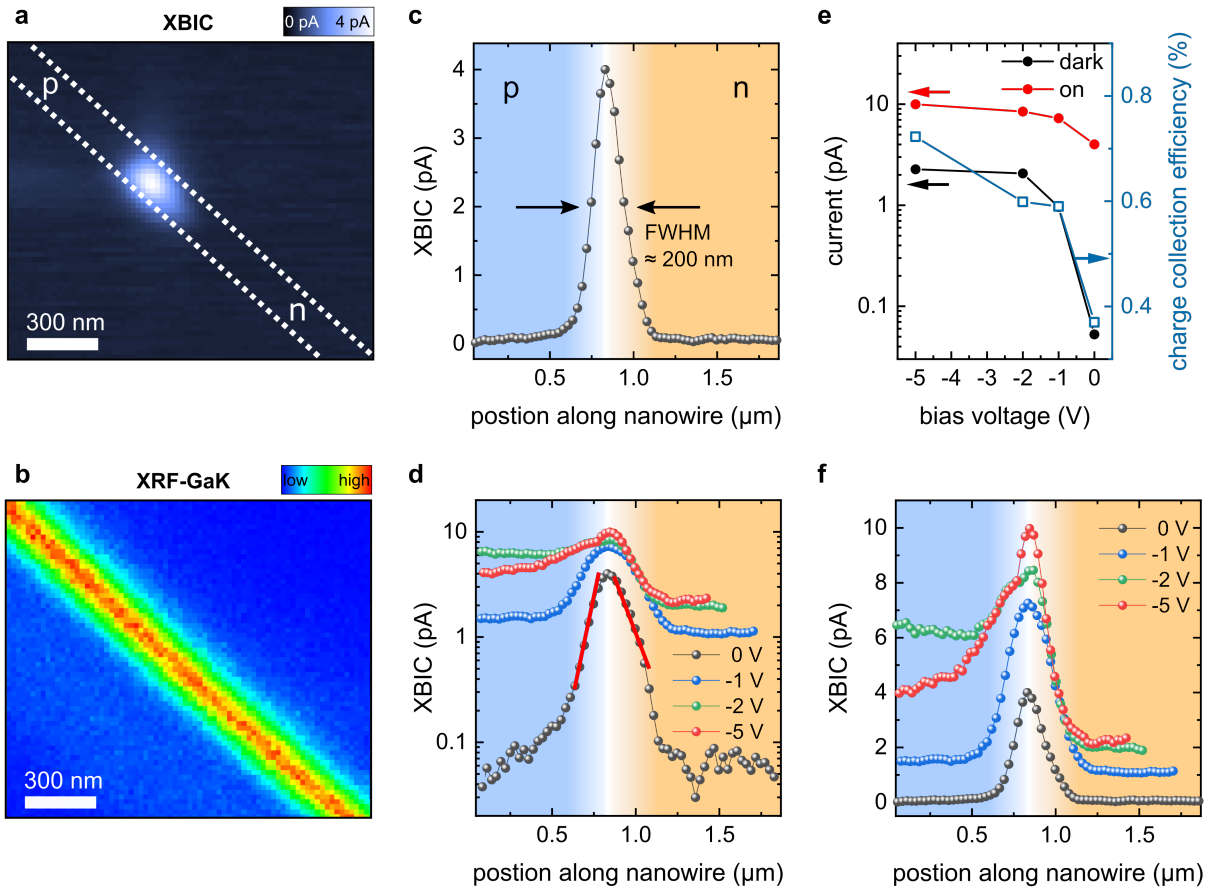


Figure 4.2.: Simultaneous mapping of nano-XRF and nano-XBIC **a** The X-ray beam induced current signal at 0V bias voltage of a GaAs nanowire around the p-n junction measured at an incident X-ray energy of 11.9 keV, i.e., above the Ga and As K-edges. The GaAs nanowire (as located via the Ga map) is indicated by the dashed, white lines. **b** X-ray fluorescence map of the Ga K_{α} line fluorescence. **c** Line scan of the XBIC signal along the nanowire. **d** Line scans of the XBIC signal along the nanowire for different voltages on a logarithmic scale. The red lines indicate the extraction of the minority carrier lengths at zero bias voltage by fitting an exponential decay to the XBIC signal. **e** Maximum XBIC signal (red dots) and dark current (black dots) as a function of the bias voltage in reverse direction. The right axis indicates the estimated charge collection (blue squares) efficiency. **f** Line scans of the same XBIC signal as in (d) along the nanowire for different voltages on a linear scale.

achieved [327]. Recently, an even better spatial resolution of ~ 150 nm was observed in vertically oriented (i.e., the nanowire axis was parallel to the X-ray beam) InP nanowires [66]. The vertical detector geometry offers clear advantages for future applications in pixel array detectors as it facilitates scaling with multiple pixels. More specifically, the vertical geometry allows using as-grown nanowire arrays such that the challenging transfer and alignment step is unnecessary. Furthermore, the much larger absorption length allows for a much more efficient X-ray absorption [66, 329]. Additionally, as the detector resolution for vertically oriented nanowires is limited by the nanowire

diameter, such that using thin nanowires could enable resolutions of few nanometers [327, 330, 331]. The horizontal geometry (where the nanowire is lying on a substrate and is thus oriented perpendicular to the X-ray beam), on the other hand, allows for a detailed, spatially resolved investigation of the internal electrical fields. It is thus ideally suited to gain a deeper understanding of the axial nanowire p-n junction, as demonstrated in the following.

The shape of the XBIC signal along the nanowire axis (see figure 4.2c) is given by the size of the depletion zone and the minority carrier diffusion length in the n- and the p-doped region [217, 332, 333]. Fitting the exponential decay of the XBIC signal (red lines in figure 4.2d) yields the minority carrier diffusion lengths L_i for electrons ($L_{D,n}=68$ nm) and holes ($L_{D,p}=108$ nm), respectively. Carrier lifetimes τ_i for electrons and holes can be assessed using the relation $L_i = \sqrt{D_i \tau_i}$, with the diffusion coefficient D_i . Inserting bulk values for D_i [334] yielded carrier lifetimes of 0.6 and 4.6 ps for electron and holes, respectively. The use of bulk values is a good approximation for our nanowires (with the diameter of ~ 150 nm) since the size dependence of the minority carrier mean free path in bulk GaAs was indeed shown to be strongly diameter-dependent below 100 nm, but hardly diameter-dependent above [123, 332, 335]. The obtained values for the minority carrier diffusion lengths are much shorter than reported bulk values, which stems from the much higher recombination rate at the nanowire surface [332, 336, 337]. This, on the one hand, reduces the efficiency of the hard X-ray detector but, on the other hand, allows the very high spatial resolution.

To quantify the detector efficiency, the charge collection efficiency (CCE) was estimated. Based on the peak values of the XBIC signal compared to the dark current, the charge collection efficiency is calculated by $CCE = Q_{\text{coll}}/Q_{\text{gen}}$ [338]. Here, Q_{coll} is the collected charge as measured at the contacts and Q_{gen} is the charge generated by the impinging X-rays. To estimate Q_{gen} , the beam energy E and the ionization energy ϵ (4.2 eV for GaAs [339]) are needed: $Q_{\text{gen}} = e \cdot E/\epsilon$, with the elementary charge e . The number of generated electrons per absorbed primary X-ray is calculated by $N = E/\epsilon$ [150]. For an X-ray energy of 11.9 keV, ~ 2800 primary electrons are generated per absorbed X-ray. In an experimental setup and device geometry comparable to our case, effects from substrate photoelectrons were shown to be negligible [327]. To finally calculate the charge carrier collection efficiency, the absorption probability in the GaAs nanowire

has to be taken into account via the absorption length ($\mu \approx 11 \mu\text{m}$ at 11.9 keV beam energy) [340]. The calculated charge carrier collection efficiency is shown in figure 4.2e. The unbiased nanowire detector reveals an charge collection efficiency of $\sim 0.4\%$, limited by charge trapping and recombination at surface defects (see carrier lifetime estimations above) [93, 336, 341, 342]. The internal electric fields in the p-n junction can be manipulated by applying a bias voltage (see figure 4.2d-f); in this way, the detector charge collection efficiency was improved.

4.1.3. Voltage and incident energy dependence of the X-ray detection

Further insights were obtained by varying the incident X-ray energy across a specific absorption edge. In this way, nano-XRF and nano-XBIC were simultaneously acquired as a function of incident X-ray energy around the Ga K-edge (see figure 4.3). The XBIC maps allow locating the p-n junction and gaining insights into the local electric fields, while XRF probes the local material composition. Mappings of XRF and XBIC were simultaneously recorded, first at 0 V with an X-ray energy below the Ga-K edge. The X-ray energy was successively increase while keeping the voltage fixed (first row). Afterwards, the bias voltage was set to -1 V and the mapping was repeated starting again at the same energy below the Ga-K edge and than successively increasing the incident X-ray energy. This was similarly repeated for -2 V and -5 V . At each bias voltage, the incident X-ray energy was varied from 10.367 keV to 10.381 keV in steps of 1 eV. In figure 4.3, XRF and XBIC maps are shown at three representative incident X-ray energies.

A clear increase of the XBIC signal is observed for applying voltages in reverse direction since the electric field of the p-n junction gets enhanced by the external voltage. At -2 V , the maximum detector signal is reached; this is accompanied, however, by a strong reduction of the spatial resolution as the spatial extent or the depletion zone increases. The reduction in XBIC signal at -5 V is associated with the degradation of the device (as shown below in more detail). As discussed above, no degradation was observed for solely applying bias voltages. Therefore, an applied bias voltage in reverse

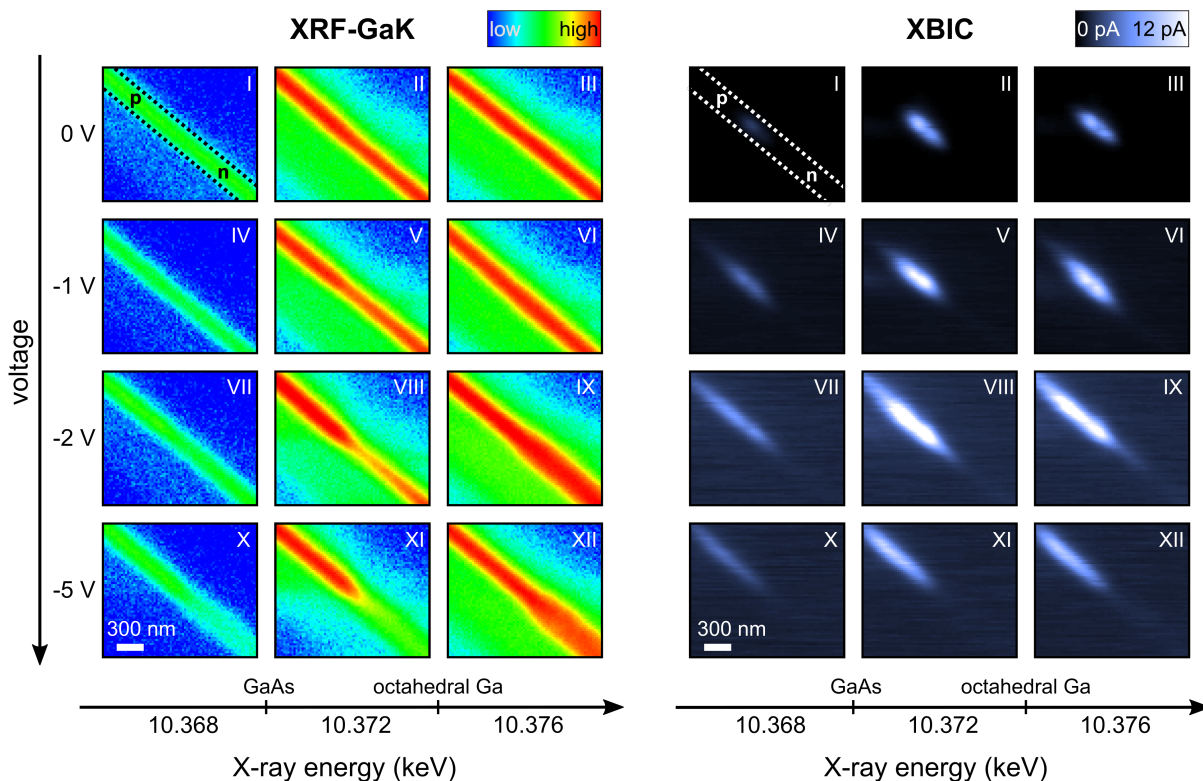


Figure 4.3.: Voltage dependent maps of nano-XRF and nano-XBIC Mappings of the Ga K_{α} XRF (left) and XBIC (right), which were recorded simultaneously at the p-n junction, as a function of incident X-ray energy and applied bias voltage. The measurement sequence is indicated by Roman numbers. All XRF/XBIC maps are equally scaled, respectively. The data is displayed on a logarithmic scale and the dashed lines in map I indicate the GaAs nanowire.

direction *together* with the incident X-ray beam are required for inducing damage.

At an incident X-ray energy of 10.368 keV, i.e., below the Ga K-edge, the XRF as well as the XBIC signal is weak (see first column). This is due to the low primary X-ray absorption in the pre-edge region, which, in turn, leads to weak secondary processes (see section 2.4). Increasing the incident X-ray energy to 10.372 keV, i.e., above the Ga-K edge, yields an abrupt increase in both signals (see middle column). This clearly indicates that X-ray absorption of core electrons from the 1s shell (which are excited above the Ga-K edge) efficiently contributes to the XRF/XBIC process. Upon increasing the voltage, however, a decrease of the Ga- K_{α} XRF signal is observed in the n-type section.

To understand this signal decrease, edge region XANES spectra were gained from the energy dependent in-operando XRF maps. This was done as a function of position along the nanowire axis for the different bias voltages (see figure 4.4a). The near-edge

4. An axial p-n junction nanowire X-ray detector at its limits

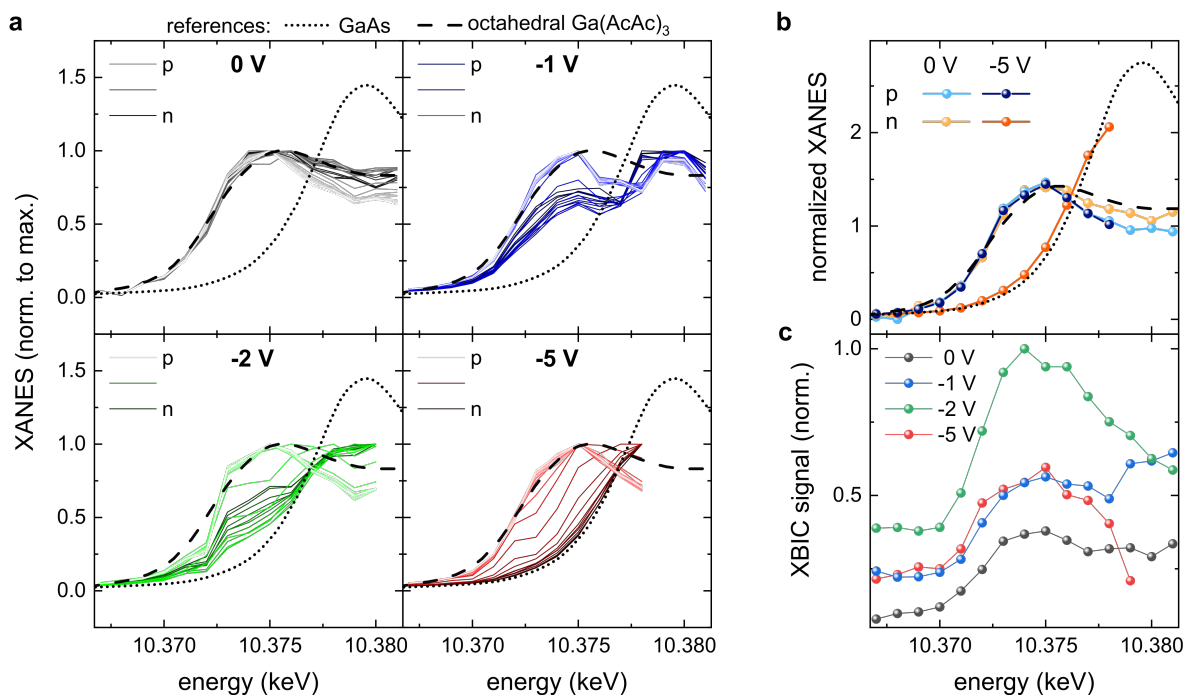


Figure 4.4.: In-operando XANES line scans **a** Near-edge region XANES spectra along the nanowire p-n junction for different bias voltages of 0 V, -1 V, -2 V, and -5 V; the spectra are normalized to the respective maximum values. References for tetragonal GaAs and octahedral Ga ($\text{Ga}(\text{AcAc})_3$) are included [343, 344]. Data acquisition failed for the last data points for the -5 V measurement (from 10.378 keV) due to device degradation. **b** Direct comparison of near edge XANES spectra in the p-type (blue) and the n-type (orange) segment for 0 V (light colors) and -5 V (dark colors), respectively. The spectra were normalized to the post-edge of full XANES spectra recorded after the in-operando measurements in the p- and n-type segment (see below). **c** Integrated XBIC signal as a function of impinging X-ray energy for the different bias voltages.

XANES spectra could not be normalized to the post-edge region, due to the limited measured energy range of the in-operando XANES spectra. The spectra were thus normalized to their maximum value. Choice and normalization of the reference spectra are based on full XANES spectra that were recorded after the in-operando measurements (see below).

At 0 V, all near edge region XANES spectra along the nanowire p-n junction are similar and clearly match the GaAs reference regarding edge energy and spectral features [343, 344], indicating a (short-range) GaAs structure. Observing the near-edge region XANES spectra from the p-type segment, no significant change in the edge energy is observed. Spectra from the n-type segment, however, reveal a shift towards higher edge energies upon increasing the bias voltage. While there is only a slight shift at -1 V, the XANES edge significantly shifts to higher energies for -2 V. Finally, at a bias

voltage of -5 V the shift in the n-type segment saturates.

Directly comparing the data collected at bias voltages of 0 V and -5 V corroborates the findings: While spectra acquired in the p-type segment remain unchanged, spectra in the n-type segment drastically shift to higher edge energies (see figure 4.4b). Simultaneously to the XRF signal, the XBIC signal was recorded as a function of the incident X-ray energy (see figure 4.4c). For all measured bias voltages, the XBIC signal reveals an energy edge similar to the Ga-K XANES edge of GaAs. At bias voltages of 0 V and -1 V the spectral features match those observed in XANES; this correlation is expected as the post-edge features arise from the fine structure of the absorption cross section [345]. At -2 V , however, the drop of the XBIC signal is stronger compared to the XANES spectra. At -5 V the XBIC signal is generally weaker and decreases even more drastically in the post-edge region. Finally, the device became insulating, leading to the failure of the pending measurements. We thus observed in-operando the step-by-step degradation of the nanowire X-ray detector.

4.2. X-ray absorption near edge structure analysis

Understanding the degradation mechanism of the axial nanowire p-n junction requires to first apprehend the observed shift in the XANES edge. To this end, full XANES spectra were acquired in the p- and the n-type segment around the p-n junction after all in-operando experiments were finished.

4.2.1. Degradation mechanism

In figure 4.5a XANES spectra from the p- and the n-type segment are compared to several references. Additionally, the full XANES spectra are compared to the in-operando near edge region spectra that were recorded at a bias voltage of -5 V . The edge energies clearly match for the respective spectra from the p- and the n-type segment, respectively; thus, the changes in XANES edge energy we observed at -5 V were permanent and transient effects connected to electrical fields or heating can be

ruled out.

In literature, Ga K-edge XANES measurements were performed investigating energy shifts in the X-ray absorption edge [211, 212, 344, 346]. In particular, absorption edges for Ga-based compounds with different ligands and coordination states of three, four, and six were reported. Edge energies were found to significantly increase with increasing coordination [211, 347]. The coordination of Ga in GaAs is tetragonal, giving rise to the peak at 10.375 keV [343]. An increase in coordination of the Ga atoms is frequently observed upon oxidization to the stable β phase of Ga_2O_3 [348]; it consists of equal fractions of tetrahedrally (GaO_4) and octahedrally (GaO_6) coordinated Ga atoms [206, 349, 350]. Nearly ideal octahedral coordination was found in $\text{Ga}(\text{AcAc})_3$,¹ which is commonly taken as a reference for Ga in the octahedral GaO_6 coordination [211, 344, 346]. There are several works on the thermal oxidization of GaAs, mostly observing the formation of β - Ga_2O_3 together with the occurrence of elemental As and well as an As depletion [107, 206, 352].

Second derivatives were calculated for all XANES spectra (see figure 4.5b) to facilitate the comparison between the measured data and the literature references. The first zero crossing of the second derivative (i.e., the first inflection) point is usually considered as the absorption edge [213, 324]. Clearly, the data from the p-type segment of the nanowire is best matched by the GaAs reference with tetrahedral coordination (as indicated by the gray, vertical line in figure 4.5b). This indicates that the p-type segment still consisted of pristine GaAs that remained structurally unchanged throughout all experiments.

The absorption edge in the n-type segment, however, shifted to higher energies. Comparing it to β - Ga_2O_3 (mixed tetrahedral and octahedral), α - Ga_2O_3 (distorted octahedral), and $\text{Ga}(\text{AcAc})_3$ (octahedral) references [211, 343, 344] reveals an excellent match to the $\text{Ga}(\text{AcAc})_3$ reference (as indicated by the black, vertical line in figure 4.5b). Both α - Ga_2O_3 and β - Ga_2O_3 have XANES edges at lower energies (~ 2 eV lower). This implies that the nanowire underwent a selective oxidization in the n-type segment resulting in an octahedral GaO_6 coordination (like in $\text{Ga}(\text{AcAc})_3$ or α - Ga_2O_3).

These findings allow to interpret the findings from section 4.1.3: a step-by-step oxi-

¹Tris(acetylacetonato)gallium(III) $\text{C}_{15}\text{H}_{21}\text{O}_6\text{Ga}$ [351].

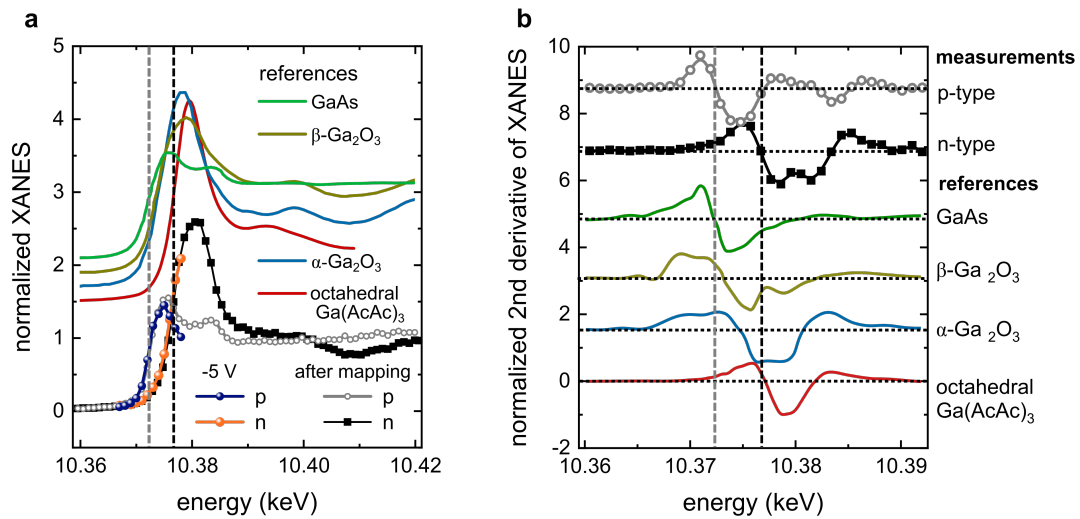


Figure 4.5.: XANES spectra **a** Ga K-edge XANES spectra acquired in the p- and n-type segment (black hollow circles and squares), respectively; the spectra were normalized to the post-edge signal. The in-operando edge region spectra recorded at -5 V (as shown in figure 4.4b) are shown as blue and orange dots. References for tetragonal GaAs, α - and β -Ga₂O₃, and octahedral Ga (Ga(AcAc)₃) are included [343, 344]. The dashed, vertical lines in gray and black indicate the Ga K-edge energies in the p- and n-type segment, respectively. **b** Second derivatives of the respective data and references. The zero crossing (indicated by the horizontal, dashed lines)—i.e., the inflection point—is considered as the edge energy. The gray, vertical lines indicate the edge energies in the p- and n-type segment, respectively. The data best matches the edge energies of the GaAs and octahedral Ga(AcAc)₃ references, respectively.

dization is observed in the n-type area of the nanowire in direct proximity to the p-n junction. In the p-type segment, however, no changes of the XANES energy edge were observed. This explains the incident X-ray energy-dependence of the XRF maps in figure 4.3 for -2 V and -5 V. The XRF signal in the p-type segment shows the same energy-dependence as for the other voltages. But the signal in the n-type segment is weak above an energy of 10.372 keV, as this is above the Ga K-edge of GaAs but below that of octahedrally coordinated Ga. The XRF signal in both segments is again leveled above an X-ray energy of 10.376 keV, as this is also above the K-edge of Ga in the octahedral GaO₆ coordination. The selective oxidization of the n-type segment also explains the decrease in XBIC signal observed for -5 V and the subsequent breakdown of the device as it became electrically insulating.

4.2.2. Assessing the selective oxidization

To make sense of the selective oxidization that is limited to the n-type segment, the full spatial extent of the oxidized region was assessed. A XANES line scan was recorded by acquiring XANES spectra along the nanowire p-n junction in steps of 50 nm. To ensure that the X-ray beam hits the nanowire centrally for all measurement points along the nanowire, multiple XRF spectra were recorded while z-scanning perpendicular to the nanowire axis (see several z-position scans along the nanowire in figure 4.6a). At the z-position with maximum Ga XRF signal the X-ray beam hits the nanowire axis centrally and the XANES spectrum was recorded. Representative XANES spectra along the nanowire are depicted in 4.6b. The measurement positions are marked in the SEM image of figure 4.6c with arrows colored corresponding to the lines in 4.6a and b. A swollen segment of $\sim 1\ \mu\text{m}$ is observed in the n-type region close to the p-n junction. The nanowire diameter has roughly doubled in diameter in the swollen segment, which coincides well with the XRF scan in figure 4.6a.

While XANES spectra far from the swollen region (purple and red spectra in figure 4.6b) clearly reveal a GaAs short-range structure, the spectrum in the middle of the swollen region (green) shows Ga in an octahedral short-range structure. Spectra in the transition region (blue and yellow) are superpositions of both. Direct effects from the incident X-ray beam—as recently observed in GaAs core-shell nanowires for directing the X-ray beam to a single spot for a prolonged period [353]—can be ruled out in our case, as the measurement region (indicated by the white, dashed lines) of the high-resolution in-operando XRF/XBIC maps comprised both the p- and the n-type segment but the oxidization is only observed in the n-type segment. Furthermore, oxidization also affected parts of the nanowire in the n-type segment that were not included in the measurement area of the high-resolution maps. This agrees with reports observing only low sample heating in an focused X-ray nanobeam [354] considering the used flux and the pulsed beam mode (see section 3.4).

To evaluate the material composition along the swollen region, three features of the XANES spectra (marked in gray in 4.6b) were integrated and plotted along the nanowire axis in figure 4.6d-f; the x-axis is aligned to the SEM image in figure 4.6c

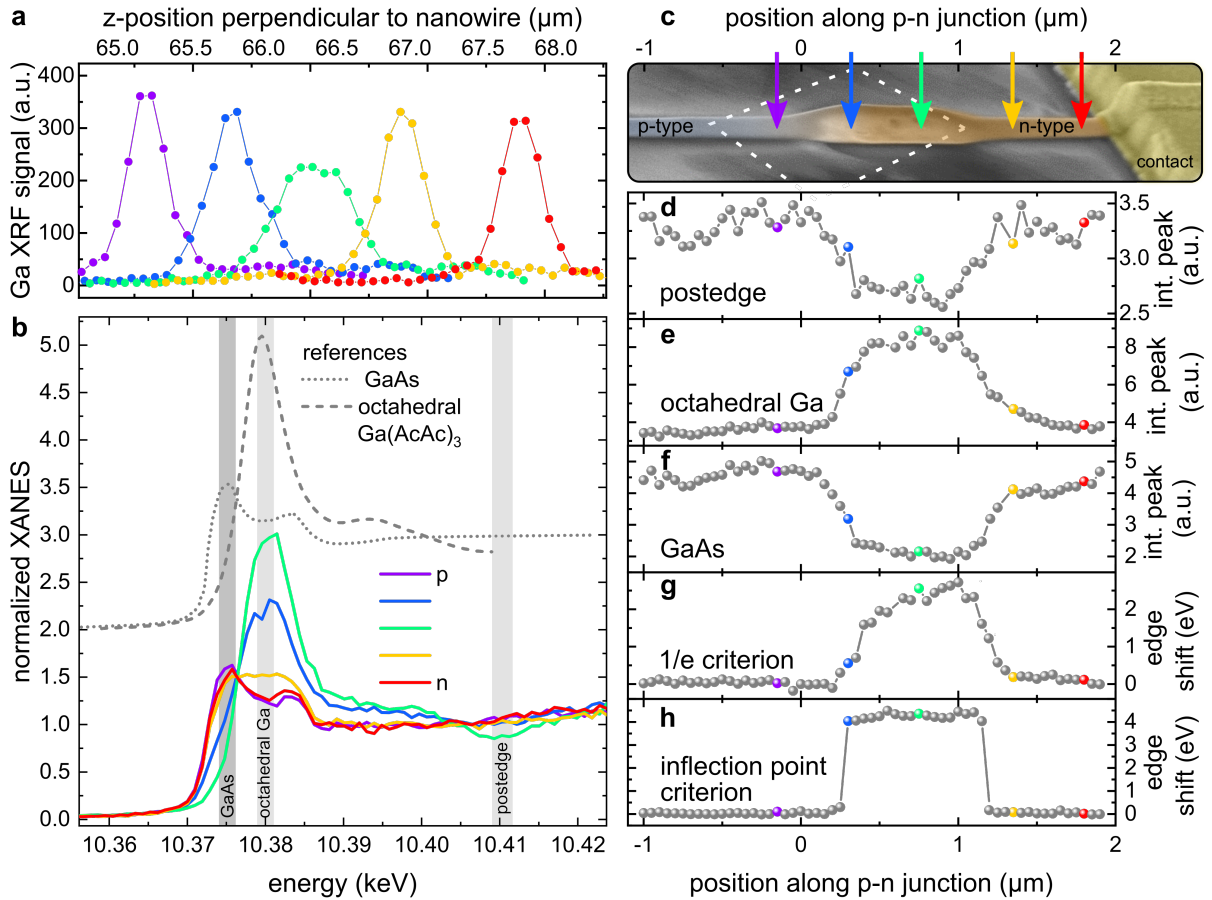


Figure 4.6: XANES line scan **a** Ga K_{α} XRF signal scanned perpendicular to the nanowire axis recorded to conduct the subsequent XANES measurement in the center of the nanowire. The symbol colors match the color of the arrows in (c) that indicate the respective measurement position. **b** Ga K-edge XANES spectra measured at different positions along the nanowire (as indicated by the arrows in (c)). References for GaAs and octahedral Ga ($\text{Ga}(\text{AcAc})_3$) are added [343, 344]. **c** Colorized SEM image of the nanowire p-n junction region after all X-ray analysis measurements. The sample was tilted by 50° and the length scale corrected accordingly. The origin of the x-axis is chosen such that the p-n junction (as identified via XBIC) is positioned at $0 \mu\text{m}$. The dashed white lines indicate the measurement area of the high resolution in-operando maps. **d-f** Line scan along the nanowire axis of the integrated XANES values from spectral regions as indicated in (b). The colored dots match the positions of the arrows in (c). **g** Line scan along the nanowire axis of the XANES edge shift as identified by the 1/e-criterion. **h** Line scan along the nanowire axis of the XANES edge shift as identified by the inflection point criterion.

such that the p-n junction (as identified from XBIC maps) is positioned at $x = 0 \mu\text{m}$ and the acquisition position for all data points can be identified. The different features were chosen at energies where the spectra of GaAs and Ga in octahedral coordination exhibit distinct differences. Therefore, GaAs material is represented by high values in the GaAs peak (figure 4.6d) and postedge curve (figure 4.6f), while oxidized Ga in octahedral coordination is represented by low values; this is vice versa for the

octahedral Ga feature curve (figure 4.6e). In this way, spectra from the p-type segment can be clearly assigned to the GaAs short-range structure and spectra from the swollen region in the n-type segment to the octahedral GaO₆ short-range structure. Spectra in the n-type segment but far from the p-n junction can also be assigned to GaAs.

Intermediate edge values between GaAs and octahedral GaO₆ were observed in transition regions at both edges of the swollen region. The intermediate Ga K-edge energies most likely stem from a superposition of an oxidized surface layer and the pristine GaAs core part of the nanowire [345]. At the edge of the swollen region that points to the p-type segment this region extends over ~ 200 nm. This transition region is broadened to ~ 500 nm at the edge that point to the n-type segment. A detectable fraction of octahedral Ga is even observed up to $1.5 \mu\text{m}$ from the p-n junction (figure 4.6e). In short, the oxidization along the nanowire can be assessed from the XANES spectra in this way.

Usually, the XANES edge is determined to distinguish between XANES spectra. There are two common criteria for obtaining values of the XANES edge energy. Often, the second derivative is calculated and the first inflection point is taken as the XANES edge energy [213, 324]. The resulting edge energies along the p-n junction are shown at the bottom in figure 4.6h. One can clearly see the benefits of the inflection point method: there is a clear distinction in edge energy between the swollen and the pristine nanowire segments and the point-to-point spreading in the respective segments is low. A major drawback, however, is the insensitivity to gradual changes in composition as observed in the XANES spectra from the transitions (blue and yellow data in figure 4.6b and c); while their XANES spectra reveal a superposition of Ga in the tetragonal GaAs site and the octahedral GaO₆ site, their inflection-point XANES edges are assigned to pure GaAs or oxidized Ga, respectively.

Another criterion to determine the XANES edge is to take the energy of the rise from the pre-edge to a fixed fraction of the edge maximum (here: $1/e$; see figure 4.6g) [213, 324]. Compared to the inflection point method, gradual changes in the transition between GaAs and octahedral Ga are reflected much better, while the point-to-point spreading is much stronger (see 4.6c). After the X-ray experiments, energy-dispersive X-ray spectroscopy (EDX) was performed close to the p-n junction of the nanowire (see figure 4.7a). A line scan across the p-n junction reveals a slight reduction of the Ga

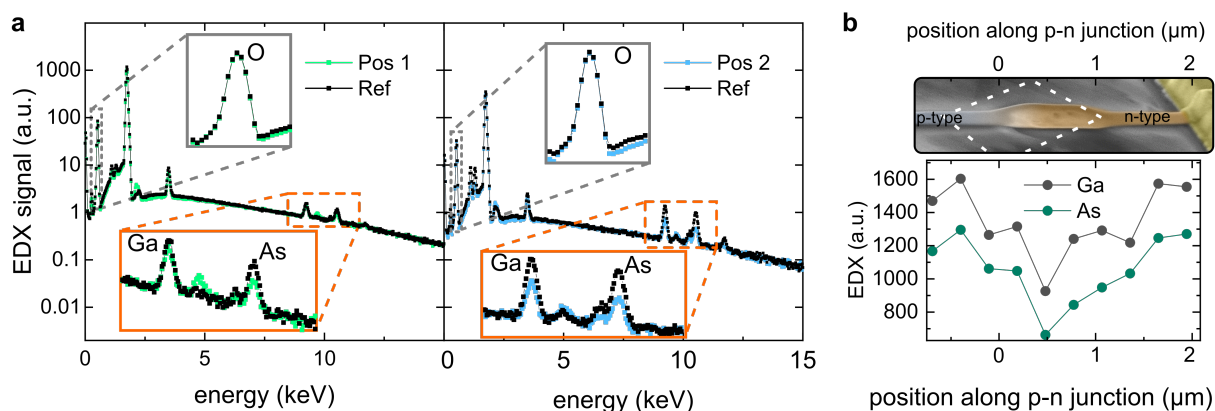


Figure 4.7.: EDX analysis in the p-n junction region **a** EDX spectra taken at two different positions in the swollen region. Additionally, reference spectra were acquired from the pristine nanowire far from the swollen region. The insets show the enlarged K_{α} lines of oxygen (at an energy of 0.53 keV), as well as of gallium (at 9.24 keV) and arsenic (at 10.53 keV). The signals of Ga and As are both reduced in the swollen region. **b** EDX line scan of the Ga and As signal across p-n junction of the nanowire. The SEM image is aligned to the x-axis of the graph and the p-n junction is chosen at the origin of the x-axis ($x = 0 \mu\text{m}$). In the swollen region, a reduction of both signals is clearly visible. The white, dashed line indicates the measurement region of the in-operando XRF/XBIC measurements.

and an even stronger reduction of the As signal (see figure 4.7b). The oxygen signal in the EDX spectrum is dominated by the signal from the insulating silica substrate underneath the nanowire; thus, changes of the EDX oxygen signal coming from the nanowire cannot be detected by EDX. The behavior of the Ga and As signals, however, agrees well with the XANES and XRF/XBIC data and thus corroborates the oxidization hypothesis.

4.2.3. Hot electron induced oxidization

Having gained a clear view on the final state of the nanowire p-n junction region, allows to gather a deeper understanding of the selective oxidization process by revisit the in-operando measurements. The Ga-K edge energy was determined from in-operando edge-region XANES spectra from figure 4.4 (via the 1/e-criterion, as discussed above) and is plotted as a function of position along the p-n junction in figure 4.8a. The XBIC signal at a bias voltage of 0 V is added to precisely locate the p-n junction, which is used as the origin of the x-axis ($x = 0 \mu\text{m}$). The Ga K-edge energy in the p-type segment is constant at $\sim 10.372 \text{ keV}$ for all bias voltages. At 0 V (black

4. An axial p-n junction nanowire X-ray detector at its limits

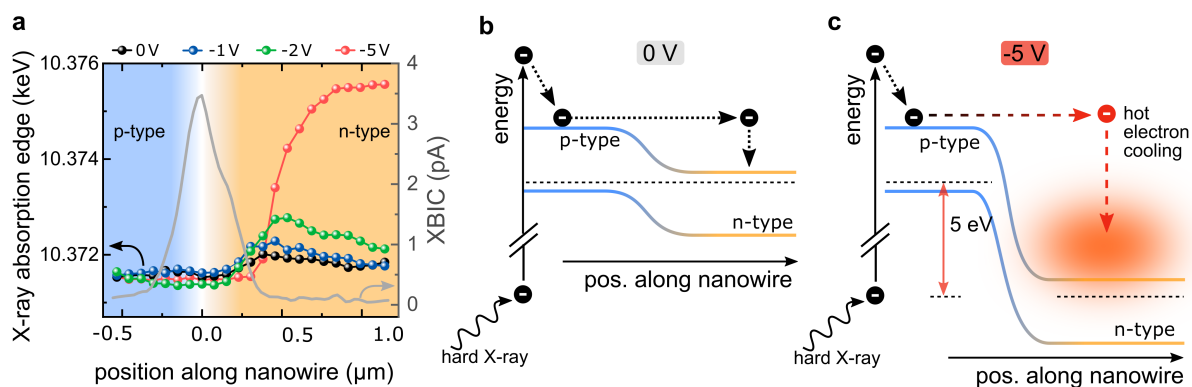


Figure 4.8.: Hot electron induced selective oxidation **a** Line scan along the nanowire axis of the Ga K-edge energies (colored dot symbol lines; left y-axis) obtained from the in-operando measurements for the different bias voltages. The XBIC signal is added to locate the p-n junction (gray line; right y-axis). **b** Schematic band diagram of the p-n junction without an external bias voltage. **c** Schematic band diagram of the p-n junction at a bias voltage of -5 V.

curve in figure 4.8a), the Ga K-edge energy is almost constant along the p-n junction. A slight increase in energy of the Ga K-edge becomes apparent in the n-type segment for applying -1 V and -2 V (blue and green curves), while the Ga K-edge energy in the p-type segment stays constant. Applying a bias voltage of -5 V (red curve) lead to an drastic increase of the Ga K-edge energy (up to almost 10.376 keV) in the n-type segment. The intermediate Ga K-edge energies that are observed in the transition region most likely are assigned to a superposition of an oxidized surface layer and the pristine GaAs core part of the nanowire, as discussed above.

To understand the underlying processes of the sample degradation, energy band diagrams of the p-n junction are addressed without and with an applied bias voltage in reverse direction (figure 4.8b and c). The built-in voltage of the GaAs nanowire p-n junction is ~ 1.1 V without an external voltage, due to band alignment with respect to the Fermi level [342]. Electron-hole pairs that are created in the depletion region are separated by this built-in voltage and can thus be measured as the XBIC signal, as shown in figure 4.8a. The electron-hole pairs are created in a cascade process: After an impinging X-ray excites electrons from core levels, core-holes are left behind, which are immediately filled from shallower levels by XRF or Auger processes. In this way, a large number of electrons and holes (~ 2500 per absorbed X-ray at 10.380 keV) is created (see section 4.1.2) at the bottom of the conduction band and the top of the valence band, respectively. This process is shown greatly simplified in figure 4.8b. Subsequently,

electrons in the conduction band that are close to the p-n junction can recombine or move down (accelerated by the built-in field) the potential towards the n-type region. The hot electrons can finally transfer their surplus energy via electron-phonon scattering to the lattice [129, 355]. Lattice heating is balanced by thermal conduction to the surrounding and along the nanowire for low electron energies [354]. As a result, there is no significant change of the Ga K-edge energy at 0 V (compare black curve in figure 4.8a). A similar behavior is expected for holes, but they do not become as hot as electrons [356] since they have lower mobilities and much higher recombination rates due to their greatly enhanced non-radiative losses [123, 336]; thus, no degradation is observed in the p-type segment.

Upon applying an external voltage, charge carriers are accelerated even more due to the additional electrical field (see 4.8). By applying a bias voltage of -5 V, hot electrons could therefore in principle reach energies up to ~ 6 eV above the conduction band in the n-type segment. The cooling of hot electrons is typically achieved by multiple scattering processes [355, 357, 358]. Beyond electron-phonon scattering, however, Auger processes and impact ionization can contribute to the electron cooling for hot electron energies above 1.45 eV [129, 359]. This limits the maximal electron energy; on the other hand, this leads to a much larger number of electrons in the n-type region of the p-n junction enabling hot electron induced chemical reactions, e.g., an oxidization of the surface [359–361]. Theoretically, this could be followed by an avalanche breakdown resulting in a pronounced heating of the n-type region, which in turn could lead to oxidization in the ambient environment. Such processes are not expected in the p-type segment as—compared to electrons—the hole mobility in GaAs is more than one order of magnitude lower, while the recombination dynamics are much faster [123, 336]. This results in the selective oxidization of the n-type segment.

Apart from those material-related effects, also the nanowire geometry plays an important role in the device degradation. The thermal conductivity of bulk GaAs is $59 \text{ W m}^{-1} \text{ K}^{-1}$. In nanowires, the thermal conductivity depends on surface roughness and wire diameter and can be much lower ($8 \text{ W m}^{-1} \text{ K}^{-1}$ to $36 \text{ W m}^{-1} \text{ K}^{-1}$) compared to bulk [110, 111, 114, 115, 362, 363]. No significant effect of doping on the thermal conductivity of GaAs was found in literature [364, 365]. The heat that is generated by hot electron cooling, is therefore distributed inefficiently and thermal gradients can

build up [354, 363]. Finally, also the large surface-to-volume ratio of nanowires and the surface band bending facilitate a surface oxidization [107, 337, 358].

A segment with a length of $\sim 1 \mu\text{m}$ was affected by the hot electron induced oxidization (compare figure 4.6c-h). However, mean free paths of hot electrons in GaAs are reported to be 30 nm to 50 nm (for much lower energies compared to our case) [357, 366]. A higher electron energy leads to a decreasing mean free path, as increased scattering rates were reported [129, 367]. The apparent contradiction can be resolved by taking multiple scattering events into account. Electrons transfer their energy stepwise via inelastic scattering to the lattice leading to a decrease in energy; this, in turn leads to increasing mean free paths during the cooling process [129, 357]. Multiple inelastic scattering of hot electrons also allows to explain the larger transition region (where the XANES edge is between GaAs and octahedral GaO_6) on the edge of the oxidized region that points to the n-type segment (between $\sim 1 \mu\text{m}$ and $1.5 \mu\text{m}$ in figure 4.6): As the electrons lose energy, their mean free path increases allowing for some electron-induced surface oxidization also further from the p-n junction. Thus, multiple inelastic scattering upon hot electrons thermalization results in an interaction length of over $1 \mu\text{m}$, i.e., much larger than the hot electron mean free path.

4.3. Conclusion

Axial p-n junction nanowires were shown to be capable of very high spatial resolution hard X-ray detection. The device revealed a direct scanning X-ray imaging resolution of $\sim 200 \text{ nm} \times 150 \text{ nm}$ with no immediate limit for a resolution enhancement by engineering the p-n junction and reducing the nanowire diameter. Based on this, spatial resolutions in the tens of nanometers might be possible for direct scanning hard X-ray imaging.

Thorough investigations using different X-ray analytical techniques enabled resolving hot electron effects in the p-n junction device. Increasing the bias voltage increased the detector efficiency but reduced the detector resolutions and led to device degradation. Incident X-ray energy-dependent X-ray fluorescence and X-ray beam induced current mapping allowed to follow the device performance and eventual degradation in-

operando as a function of bias voltage. A selective oxidization was observed in the n-type segment of the nanowire, while the p-type segment stayed pristine. The Ga coordination of the oxidized segment was found to be octahedral in contrast to the tetrahedral GaAs. The oxidization was attributed to the cooling of hot electrons resulting in the degradation of the biased device. Several technical components rely on hot carrier effects, e.g., Gunn diodes and IR sensors [368, 369]. On the other hand, hot carrier effects are well-known as the prevailing degradation mechanism in transistors [370]. These effects are expected to be even more pronounced for nanoscale applications—including nanowires—due to their pronounced surface-to-volume ration and the limited thermal conductivity [114, 362, 363].

5. Stability of photonic nanowire devices

In this chapter, the stability of photonic II-IV nanowires is analyzed. First, the spontaneous photoluminescence and waveguiding in pristine ZnO nanowires is studied. Afterwards, the stimulated emission of CdS and ZnO nanowires is examined with regard to the stability at high excitation intensities. Finally, the stability of the spontaneous and stimulated emission as well as of the waveguiding in ZnO nanowires were studied as a function of electron irradiation.

This work was done in close collaboration with Gesine Thees within the scope of her state examination thesis [117] and Johannes Nicklaus within his bachelor thesis [118]. Parts of these results are published in references [96, 317].

5.1. Limits of optical excitation in II-IV nanowire lasers

Today, optical excitation is the go-to method for achieving population inversion and thus lasing in nanowires [17, 84]. Future applications in nanoscale devices would, however, often require electrical pumping of the nanowire lasers. While there are some reports on electrically driven amplified spontaneous emission (ASE) and electrical triggering of nanowire lasing, reaching sufficient current densities for population inversion proved challenging [87, 371, 372]. Yet, external optical pumping might be compatible with device integration in many cases and could be used for nanowire-based lab-on-a-chip or on-chip interconnection applications. To ensure stable and enduring operation, device stability is crucial for most approaches. Therefore, the operational

stability of optically pumped nanowire lasers is investigated in the following. First of all, optical emission and waveguiding is addressed in the spontaneous emission regime. Further, the emission in the stimulated emission regime is discussed and limits for the operation of optical pumped nanowire lasers are examined. The findings of this section will be taken as the groundwork for electron irradiation dose dependent measurements in sections 5.2.4 and 5.2.6.

5.1.1. Spontaneous luminescence and waveguiding in single nanowires

Investigating individual nanostructures by micro photoluminescence (PL) requires a tightly focused laser spot to efficiently excite the small nanostructure volume that usually is smaller than the diffraction limit; since the active (i.e., excited) area is by definition small in nanostructures, an efficient local detection is furthermore needed. Still, much higher excitation densities compared to conventional PL are necessary to generate a sufficient signal-to-noise ratio.

Spontaneous luminescence A typical photoluminescence spectrum of a ZnO nanowire (see figure 5.1a) shows a narrow emission band around 380 nm—the near band edge emission (NBE)—and a broader emission in the visible—the deep level emission (DLE). The latter stems from several transitions involving deep level defects (see section 2.5.3) and can thus be fitted by multiple Gaussian contributions. Here, the wavelength-dependent spectra were fitted. Note that fitting the same data on an energy-dependent scale yields the same results, as the differences in the two scales are negligible here for the Gaussian fitting.

To evaluate the working range of harmless excitation, the peak position of the NBE peak was investigated as a function of excitation laser intensity for several individual nanowires (see figure 5.1b). The peak position is constant at ~ 382.3 nm up to ~ 3 kW/cm², while it redshifts for higher excitation power densities. This redshift is attributed to a bandgap reduction due to heating of the nanowire by the excitation laser [373]. The cw laser induced heating for an excitation intensity of ~ 90 kW/cm²

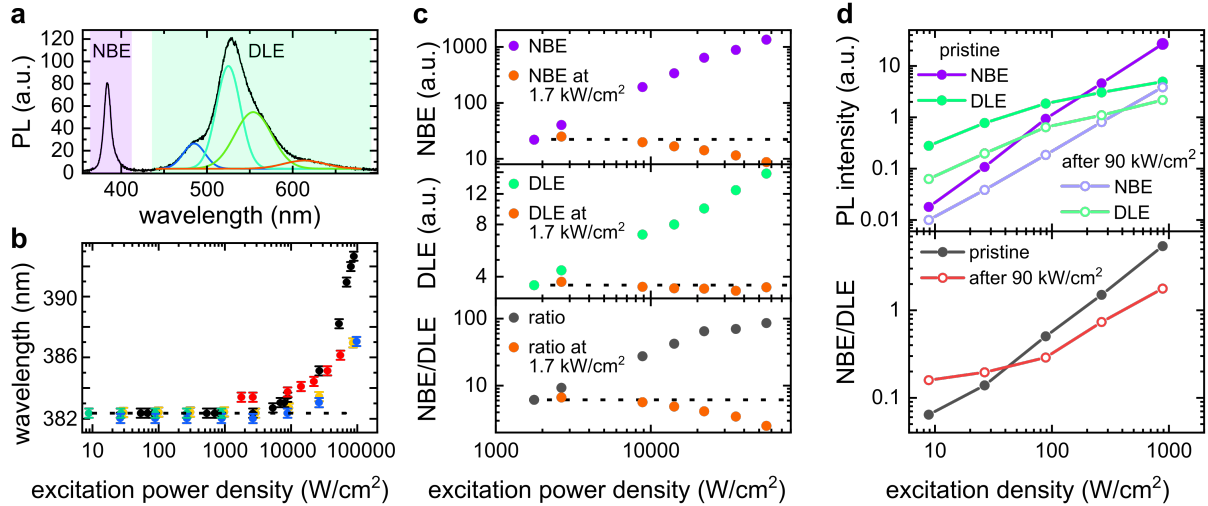


Figure 5.1.: Power-dependent photoluminescence. **a** Photoluminescence spectrum of a single ZnO nanowire on a SiO₂/Si substrate excited at 325 nm with an excitation intensity of $\sim 200 \text{ W cm}^{-2}$. The defect emission peak is fitted with multiple Gaussian functions. **b** Peak position of the NBE as a function of excitation laser intensity. Different colors represent different nanowires. The dashed lines indicates the peak position for the black dots at low powers. **c** Power dependency of the photoluminescence signals. From top to bottom, the panels show the integrated NBE, DLE, and NBE-to-DLE-ratio. The orange dots are from repeated measurements at 1.7 kW cm^{-2} recorded after exposure to the power density indicated by the respective x-axis position. **d** Excitation power dependencies prior and after irradiating the nanowire with an excitation intensity of 90 kW cm^{-2} for 60 s.

can be estimated to be between 50 and $\sim 160 \text{ K}$ for the different nanowires by using the Varshni equation with the parameters $\alpha = -5.5 \times 10^{-4} \text{ eVK}^{-1}$ and $\beta = -900 \text{ K}$ [374]. Thus, further measurements were generally limited to powers below 3 kW/cm^2 to avoid strong heating.

Luminescence quenching for was investigated by observing the power dependency of the integrated NBE and DLE. The excitation laser intensity was successively increased starting from 1.7 kW/cm^2 ; after each intensity step the intensity was reduced back to 1.7 kW/cm^2 and an additional spectrum was recorded to investigate for degradation (see figure 5.1c). With increasing excitation power both NBE and DLE increase nearly linearly. However, the repeatedly measured reference spectrum at 1.7 kW/cm^2 reveals a monotonically decreasing NBE, while the DLE remains almost constant (see orange dots in figure 5.1c). The NBE-to-DLE ratio increases linearly with increasing excitation power, while the ratio for the reference measurements monotonically decreases. Often, the NBE-to-DLE ratio is taken as an indication of crystal quality in semiconductors; however, this ratio has to be compared at a fixed excitation conditions since it strongly

depends on the excitation intensity [174]. Thus, the decrease of the NBE-to-DLE ratio observed at 1.7 kW/cm^2 after illumination with increasing excitation power might be attributed to degradation [375]. To study the laser-induced degradation in more detail, the power dependency of the PL emission was investigated for another, pristine ZnO nanowire (full circles in figure 5.1d). Afterwards, the nanowire was irradiated at an laser intensity of $\sim 90 \text{ kW/cm}^2$ for 60 s and the power dependencies were re-measured (empty circles in figure 5.1d). Both NBE and DLE are quenched after the strong laser irradiation. While the DLE decreased by an almost constant factor for all excitation powers, the slope of the power-dependent NBE decreased from ~ 1.6 to ~ 1.3 . Interestingly, this leads to an increased NBE-to-DLE ratio at low powers. This clearly demonstrates that the NBE-to-DLE ratio at one particular excitation power cannot simply be taken as an indicator of optical quality; instead, one has to consider the full power dependency. The background electron concentration from unintentional doping dominates the electron density at low excitation power densities while generated electrons become increasingly dominant with increasing excitation power (compare section 2.3.2). The slope of the NBE (and the NBE-to-DLE ratio) can thus give qualitative insight into changes of the quantum yield (this will be discussed in section 5.2.4 for electron irradiated nanowires).

Waveguiding The ability of semiconductor nanowires to actively guide light along its axis allows for directing and switching the light transport at sub-wavelength scales [78]; it also is a necessary prerequisite for nanowire lasing (see next section) [80, 88–90]. The light guided through the nanowire, however, also allows to examine the absorption near the band edge as presented in this section. Waveguiding in pristine nanowires will serve as a reference for investigating the electron beam irradiation dependent waveguiding in section 5.2.6.

To observe waveguiding, a single nanowire was excited at one end (called A in the following) and the luminescence was recorded at the other end (called B; see figure 5.2a). Subsequently, the excitation laser was moved along the nanowire while the waveguided emission was recorded at end facet B. One should bear in mind that this configuration is different from coupling light to a fiber or measuring transmission in thin films [183, 376, 377]: The source of the light that is guided through the nanowires

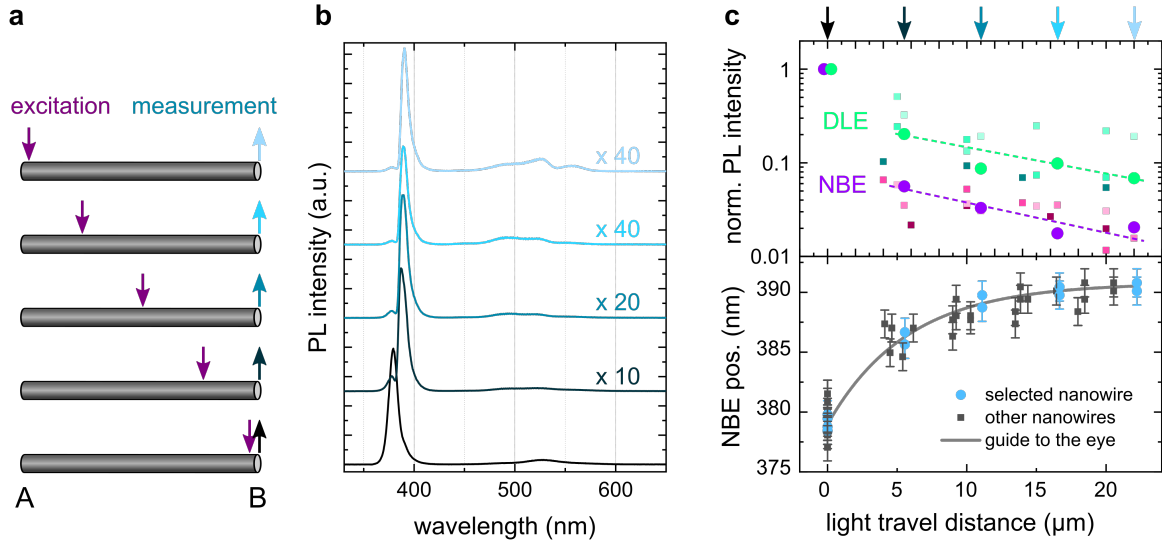


Figure 5.2.: Waveguiding in ZnO nanowires. **a** Schematic of the excitation/measurement configuration. At each excitation position, the luminescence at the excitation spot and the waveguided spectrum at end facet B were acquired. **b** Waveguided photoluminescence spectra recorded at end facet B for different excitation positions (blue curves) from a single nanowire ($d \approx 250$ nm, $L \approx 22$ μm). The black curve depicts the spectrum recorded directly at the excitation spot (end B, black curve). All curves match the colors of the arrows in (a) illustrating the respective measurement configuration. The waveguided spectra were multiplied by the indicated scaling factors. The weak peak at ~ 380 nm in the waveguided spectra is scattered light from the excitation spot. **c** Upper graph: Integrated intensity of the NBE and DLE signal as a function of the waveguiding distance. All intensities were normalized to the spectra at the excitation position. The dashed lines are guides to the eye. Lower graph: NBE peak position as a function of waveguided distance. In both graphs, the large dots stem from the same nanowire as the spectra shown in (b)—the blue arrows on top match the colors of the respective waveguided spectra—and the small squares stem from three further similar nanowires.

is not the excitation laser itself but the ZnO luminescence spectrum generated by the excitation laser [76].

Comparing the waveguided spectrum (blue curves in figure 5.2b) to the spectrum measured directly at the excitation position A (black curve) reveals a decrease in intensity and a redshift in peak position of the NBE (see figure 5.2b and c). The latter is attributed to the absorption in the Urbach tail states and the subsequent emission-absorption-emission process (see section 2.3.3) [184], which leads to a successive loss in photon energy until saturation is reached when the photon energy becomes too low to be absorbed in the tail states (lower graph in figure 5.2c). At this point, the emission-absorption-emission process breaks down and the waveguiding in the nanowire becomes passive. The redshift of $\Delta\lambda = \lambda_0 - \lambda_{\max} = (12 \pm 3)$ nm from the excitonic emission (recorded at the excitation-spot) to the saturated emission allows

estimating the energy width of the Urbach tail states to $\Delta E = (100 \pm 30)$ meV. This agrees reasonably well with reported values of the Urbach tail state width for ZnO thin films, which are between 44 and 85 meV [183, 187, 188]. The slightly higher tail state width observed in the nanowires might be attributed to an increased density of surface defects in nanowires [168, 251, 261, 299].

To investigate the decay of the PL signal with waveguiding distance (upper graph in figure 5.2c), NBE and DLE signals were integrated in the waveguided spectra for several nanowires. The waveguided signals were normalized to the respective signal from the excitation positions to account for small deviations in intensity for the different excitation positions. The intensities show a much greater spread compared to the peak positions (lower graph in figure 5.2c) since the intensities are strongly dependent on the exact excitation conditions (due to changes in the coupling to the waveguide), while the peak position is independent of such variations. Both, the waveguided NBE and DLE, show an exponential decay with traveled distance in the nanowire. No saturation was observed for the investigated travel lengths. A saturation of the NBE signal, however, would be expected at the point where the waveguiding becomes passive (see above), if the emission-absorption-emission process dominated the intensity loss. This indicates that the intensity decay of the NBE is not dominated by the emission-absorption-emission process in the Urbach tail states. Instead, passive losses from impurity scattering, surface scattering and confinement [378] strongly contribute to the transmission losses for the NBE and DLE in the investigated distance range. Assuming these optical losses as linear and constant over the length of the nanowire, this explains the exponential decay of the waveguided NBE and DLE intensity [25].

Compared to the excitation spot value, $\sim 20\%$ of the waveguided DLE signal is detected at end facet B, while the NBE signal shrinks to below 6% after traveling a distance of $\sim 5\ \mu\text{m}$ through the nanowire. For traveling the full nanowire length ($22\ \mu\text{m}$), these values reduce to $\sim 7\%$ for the DLE and $\sim 2\%$ for the NBE. In the following, these values will be referred to as "transmission", keeping in mind that the initial signal is the luminescence at the excitation spot (to be more precise, the fraction of light that couples into the waveguide). Two factors might contribute to these different transmission values. First, absorption and scattering are lower for the DLE due to the lower photon energy, i.e., the waveguiding losses are lower. Confinement losses,

however, are potentially much higher for the DLE [23]; nevertheless, they seem to be low within the nanowire diameters of ~ 250 nm used in these experiments. Second, the transmission of the DLE gains from absorbed photons from the NBE that recombine via deep defects in the waveguiding process and thus emit in the DLE range. Due to energy conservation, the opposite process (DLE to NBE) is not possible.

5.1.2. Limits of the stimulated emission

Achieving room temperature lasing for any given material requires a sufficiently low lasing threshold, such that the lasing regime can be reached upon exciting with reasonable pump power densities. This immediately implies that there is an excitation power limit that may not be surpassed for stable laser emission [317]. In the following, this limit is identified and quantified in CdS and ZnO nanowires that serve as a model system.

A CdS nanowire laser was illuminated with a widened laser spot such that the whole nanowire was excited to prevent re-absorption within the nanowire. The spectral evolution for increasing pump intensity is shown in figure 5.3a. At low excitation power densities, a broad spontaneous emission peak is observed (black curve). Increasing the excitation power yields sharp modes that are superimposed to the spontaneous emission: the amplified spontaneous emission (ASE; light blue curve). In the double-logarithmic power dependency (see green curve in figure 5.3b), this is accompanied by a superlinear increase. Further increasing the power leads to the lasing regime; here, the modes clearly dominate the spectrum and the slope of the power dependency becomes linear again (see also blue and orange spectra). The transition to the lasing regime is marked by the lasing threshold (where gain/loss is 1). The power dependency was fitted with a multimode laser model [201] that yielded a lasing threshold of $\sim 70 \text{ kW cm}^{-2}$ and an spontaneous emission parameter x_0 of ~ 0.1 . This fit agrees well with the data in the spontaneous, the ASE, and the lasing regime. Upon increasing the pump intensity even further, however, there is a point where the acquired data points clearly deviate from the fit and the emission even decreases despite increasing the excitation power. This is the regime of irreversible degradation and the point where

the emission starts to decrease despite increasing excitation is defined as the degradation threshold. This threshold thus separates the regime of stable lasing from the regime of irreversible degradation. The decrease in emission at high pump intensities is accompanied by alterations in the spectra (see figure 5.3a): The formerly nearly equidistant Fabry-Pérot modes start to merge and become increasingly irregular (red spectrum). Remarkably, new modes start emerging far from the initial gain envelope. For the highest excitation power density, all modes are finally eradicated leaving a broad spontaneous emission spectrum behind (dark red spectrum).

Similarly, a lasing-degradation curve was measured for ZnO nanowires. Fitting the data with a multimode laser model yielded a threshold of $\sim 210 \text{ kW cm}^{-2}$ and an x_0 value of ~ 0.01 , in good agreement with literature [83, 379]. For the highest measured excitation powers, the emission is halved upon increasing the excitation power. Thus, the degradation threshold for this nanolaser was $\sim 3 \text{ MW cm}^{-2}$. However, a further increase of excitation power was prevented as the nanowire moved out of the excitation laser spot. Similar effects of moving nanowires were observed for all investigated ZnO nanowires under high excitation power densities and might be attributed to strong thermal gradients. The movement prevented a more thorough degradation analysis for ZnO and further experiments were conducted for CdS nanowires. However, to corroborate the degradation in the ZnO nanolasers, additional to the power-dependent emission, the lasing spectrum at the threshold power was repeatedly measured. The area under the lasing modes, integrated from those spectra, was constant up to the degradation threshold of $\sim 3 \text{ MW cm}^{-2}$ and drastically decreased above the threshold (see inset in figure 5.3b). This degradation threshold is in good agreement with literature [375]. There is a slight deviation from the fit at low and high gain-loss values, hinting to an important subject. Since the experimental setup has a limited detection angle and spatial detection region, there are different detection efficiencies in the different regimes due to the changing emission angle and spatial emission origin when transiting from spontaneous emission to lasing (see section 2.3.2). This experimental realities—together with further experimental factors, such as spot homogeneity and pulse-to-pulse variation of the excitation laser, nanowire-to-nanowire variations, detection (and monochromator) setup efficiencies, and substrate properties—imply that the obtained threshold values cannot directly be compared to values obtained

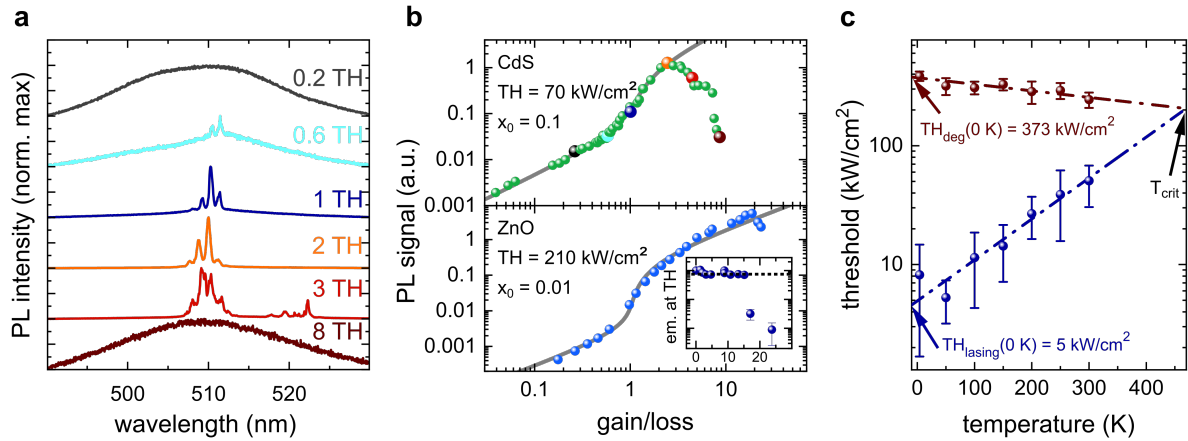


Figure 5.3.: Lasing limitation in CdS and ZnO. **a** Normalized spectra from one individual CdS nanowires for increasing pump intensity (top to bottom). The respective pump intensities are indicated as multiples of the lasing threshold. At low pump intensities the broad, unstructured NBE is observed (black). Increasing the pump intensity yields cavity modes that appear on top of the spontaneous emission. The cavity modes start to dominate the spectrum when increasing the pump intensity further (i.e., above the lasing threshold TH_{lasing}). Above $\sim 3 TH_{\text{lasing}}$, the nanowire emission shows a significant decrease in intensity; also the spectral shape reveals deviations. Finally, above $\sim 8 TH_{\text{lasing}}$, the lasing modes totally vanish, clearly indicating the lost lasing capability. **b** Double logarithmic power dependence of the optical emission from the CdS nanowire (top) and a ZnO nanowire (bottom) as a function of the gain/loss ratio. A typical laser behavior is observed up to $\sim 2 TH_{\text{lasing}}$ and $\sim 15 TH_{\text{lasing}}$ for the CdS and ZnO nanowires, respectively. Exceeding this degradation threshold (TH_{deg}), causes the emitted intensity to drop. The power dependence below TH_{deg} was fitted by a multimode laser model (gray line) [201]. The inset shows the emission at the threshold that was repeatedly measured after each power step. **c** Temperature-dependency of the average threshold values. For each temperature, the threshold values of 5 nanowires were measured and averaged; the error bars represent the respective standard deviation. Both, the lasing (blue) and the degradation (red) threshold follow an exponential temperature-dependency (dash-dotted lines). Extrapolating the curves to higher temperatures yields an intersection point, which is defined as the critical temperature $T_{\text{crit}} = 470$ K. Above, no stable lasing can be achieved.

from different setups. It is furthermore well-known that the spontaneous emission parameter x_0 is heavily depending on the detection geometry [84, 380].

Using CdS nanowires, further nanolaser degradation experiments were carried. A larger number of nanowires was used allowing for a statistical approach that can compensate some of the experimental challenges named above; however, it must be emphasized, that obtained threshold values still depend strongly on excitation laser, substrate, and detection conditions such that caution must be taken when comparing absolute values of measurements in different setups.

Lasing and degradation threshold values at room temperature were obtained for 19 different CdS nanowires. To do so, criteria for both thresholds were defined such that

they can be measured without acquiring the full power dependency. In consistency with the findings from figure 5.3a and b, the lasing threshold was defined as the excitation power at which the modes surpassed twice the spontaneous emission background. The degradation threshold was defined as the point at which the detected nanolaser emission decreased despite increasing the excitation power. In this way, lasing and degradation thresholds were determined for all nanowires and finally averaged. Besides the room temperature measurements, the thresholds were further determined as a function of temperature by measuring 30 additional nanowires at each temperature step. The average values are shown in figure 5.3c as function of temperature; the standard deviation is added as error bars. In laser systems, the threshold behavior is well-known to be exponential with temperature [381–384]

$$\text{TH}(T) = \text{TH}(0) \cdot \exp(T/T_0). \quad (5.1)$$

Fitting the exponential increase of the lasing threshold yields values of $\text{TH}_{\text{lasing}}(0 \text{ K}) = (5 \pm 1) \text{ kW cm}^{-2}$ and $T_{0,\text{lasing}} = (125 \pm 14) \text{ K}$, while fitting the exponential decrease of the degradation threshold yields $\text{TH}_{\text{deg}}(0 \text{ K}) = (373 \pm 16) \text{ kW cm}^{-2}$ and $T_{0,\text{deg}} = (-800 \pm 100) \text{ K}$. Hence, like it is well-known for the lasing threshold, the underlying mechanism for the degradation is temperature-dependent, which points to a thermal contribution in the degradation process. To address the full temperature-stability of CdS nanolasers, both threshold dependencies were extrapolated to higher temperatures, allowing to determine the intersection point of both curves, the critical temperature T_{crit} (as shown in figure 5.3c). For temperatures below this point, stable lasing in the nanowire lasers can be reached, while above, no lasing is possible without immanent degradation of the device. The critical temperature thus is the high temperature limit of lasing for the specific experimental conditions used here.

The gain mechanism that supports the nanowire lasing is an electron-hole plasma, which forms under strong optical pumping [82, 385]. As the excitation laser pulse duration in the experiments was $\sim 7 \text{ ns}$, a thermal degradation mechanism can be expected (in contrast to non-thermal degradation mechanisms that dominate for shorter ($\lesssim 200 \text{ fs}$) laser pulses) [386, 387]. This is in agreement with the temperature dependence of the degradation threshold described above. High laser pump densities

might thus lead to decomposition, desorption, or melting. Yet, since the nanowire morphology was mostly unchanged after the lasing experiments, melting can be discarded. This agrees well with ns-laser experiments on bulk CdS. Above a desorption threshold of 18 mJ cm^{-2} , the ejection of species (mostly S_2) was observed from the surface and regions close to the surface [388, 389]. These findings were explained by a bond softening mechanism: non-thermal effects, such as the formation of the electron-hole plasma at high excitation powers screen bond charges and therefore reduce thermal stability at sufficiently high pump powers [389, 390]. In combination with the laser induced thermal heating, the bond softening allows for the desorption of surface species, most prominently sulfur atoms via the formation of S_2 dimers. Since sulfur is predominantly ejected from the lattice, a Cd-rich surface is expected to remain. The laser degradation threshold for ns-laser excitation observed by Namiki et al. was $(18 \pm 5) \text{ mJ cm}^{-2}$ [389]. This can be compared to our experimental energy density value of $\sim 1.6 \text{ mJ cm}^{-2}$ from the CdS nanolasers considering the much higher surface-to-volume ratio of the nanowires together with reduced thermal conductance for the nanowire geometry. A higher degradation threshold of $\sim 80 \text{ mJ cm}^{-2}$ was reported for ZnO [389]. Again, this can be compared to our experimental energy density value of $\sim 30 \text{ mJ cm}^{-2}$ from the ZnO nanolasers considering the nanowire geometry. The higher degradation threshold compared to CdS can mostly be explained by the lower ionicity of ZnO [388]. Other typical laser materials such as GaN, InP, or GaAs most likely also show a similar degradation mechanism, however, with different threshold values [389]. Thus, the degradation behavior of nanolaser systems has to be carefully evaluated for the respective pump conditions to assess the potential of the respective nanowire laser system for (above-) room temperature operation. Future studies on nanoscale lasers also have to make sure stable operation is observed. To ensure degradation-free measurements, experimental routines are necessary. For example, after measuring the lasing curve from low to high powers, it should be repeatable when reducing the power again. An easier way to proof stable emission might be repeatedly re-measuring the lasing spectrum at a certain power (e.g., the threshold, as shown in the inset of figure 5.3b).

Apart from such passive measures to avoid degradation, one can actively increase the critical temperature and thus the regime of stable laser operation. To increase the

degradation threshold, low refractive index substrates can be chosen that additionally exhibit a faster heat dissipation from the gain medium to the substrate. Here, CaF_2 or MgF_2 could enhance heat dissipation due to their high thermal conductivity, which is 5 and 15 times larger, respectively, than that of the SiO_2 substrates used in the experiments [391–393]. Sapphire has an even larger thermal conductivity, which might result in a higher degradation threshold [394]; however, due to its larger refractive index the lasing threshold would also increase, since the smaller refractive index difference to the nanowire would increase waveguiding losses. Coating the nanowire with a dielectric could likewise increase the degradation threshold by suppressing the laser induced desorption. On the other hand, the critical temperature (i.e., the high temperature limit for lasing) can be increased by lowering the lasing threshold. In turn, the lasing threshold can be decreased by decreasing waveguiding or reflection losses [17, 94].

5.2. Influence of electron irradiation on the luminescence of nanowires

Since the emergence of nanotechnology, imaging at the nanoscale became indispensable for the field. Instead of optical microscopes that are bound to the Abbe limit, electron microscopes are utilized to access the micro-/nanostructure and morphology of objects on the nanoscale. Their vital function was recently stressed with the advent of nanorobotic manipulation tools that allow for direct characterization and assembling at the nanoscale [395]. Researchers, however, became aware of luminescence quenching effects while acquiring CL spectra of semiconductors, indicating a detrimental effect of electron irradiation on the luminescence. In ZnO bulk crystals, a CL signal reduction was observed on the Zn-terminated surface, while a small increase followed by a decrease was observed at the O-terminated surface for prolonged irradiation with electrons [396]. In GaN nanowire ensembles, a pronounced luminescence quenching was observed under electron irradiation indicating a relation to the greatly enhanced surface-to-volume ratio in nanowires [397]. Finally, ZnO nanowires were shown to

switch from a hydrophilic surface to a hydrophobic surface by electron irradiation [398]. It is thus clear that electron beam irradiation has a strong effect on the (surface) properties of ZnO nanowires. At the same time, ZnO is well-known to be exceptionally robust against radiation damage under high energy electron irradiation in the MeV-range [399–403], but also against neutrons [404], gamma rays [405], protons [406], and ions [407, 408], making ZnO even suited for space-based applications [401] or as scintillator material [405]. Interestingly, radiation hardness was shown to be increased in nanowires due to defect compensation at the surface [409]. Despite its high resistance to irradiation damage, however, the above-mentioned luminescence quenching upon electron irradiation in the SEM was observed. To understand these effects, single ZnO nanowires were irradiated with an electron beam in an SEM. The luminescence was investigated during irradiation via CL and after certain irradiation times by PL. Further, the stability of waveguiding in single nanowires and their lasing properties were examined as a function of the electron irradiation.

5.2.1. Electron irradiation dependent cathodoluminescence

The electron beam of an SEM was scanned across half of a single ZnO nanowire on a silica substrate while the CL signal was acquired (see figure 5.4a and inset in figure 5.4b). The non-irradiated lower half was used as a reference for subsequent PL investigations. NBE and DLE were measured separately in order to investigate effects of the electron irradiation on the luminescence. This allowed fast data recording within 60 s such that changes during spectral acquisition can be neglected. In this way, CL spectra of the NBE and DLE were alternately recorded in succession during irradiation for 90 min at 10 kV with an electron flux density of $\sim 0.24 \text{ mC s}^{-1} \text{ cm}^{-2}$ (see figure 5.4b). Note that it is not possible to record spectra of pristine, non-irradiated nanowires in the CL, since already the first CL spectrum is recorded with an acquisition time of 60 s and at least several seconds of electron beam irradiation are needed to focus the electron beam on the nanowire. The very different trends for NBE and DLE become obvious in the time-evolution of the integrated signals (figure 5.4c). While the DLE signal increases monotonically and saturates for progressing irradiation, the NBE signal peaks after

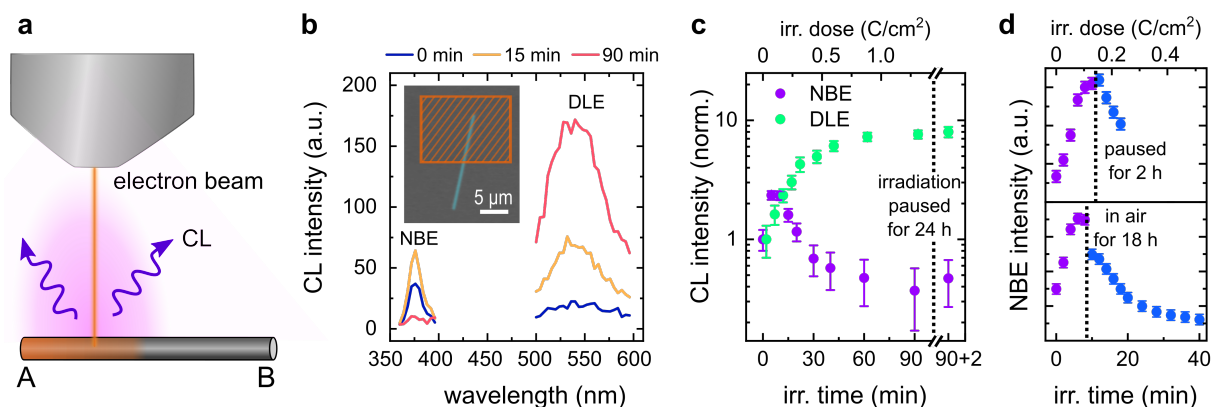


Figure 5.4.: Cathodoluminescence of single ZnO nanowires. **a** Scheme of the CL measurements upon electron irradiation. Roughly half of the nanowire was irradiated (end A), while the other half remains pristine (end B). **b** CL spectra obtained from the region indicated in the inset. The NBE and DLE spectra were acquired successively. Thus, the irradiation time prior to spectral acquisition for the DLE was always 2 min larger than given in the legend. **c** Electron irradiation dependency of the integrated CL intensity for the NBE and the DLE. After 90 min of irradiation, the electron beam was blanked and the sample was kept in vacuum for 24 h. **d** Similar electron irradiation dependencies as in (c) were measured for further wires. After reaching the maximum, irradiation was paused for 2 h (lower panel). Another sample was taken out of the vacuum and stored in air for 18 h (lower panel). Afterwards the irradiation was continued for both samples.

~ 10 min of irradiation, afterwards decreases, and finally saturates well below its initial value. After 90 minutes of irradiation, the irradiation was paused while the sample was kept in vacuum; after 24 h, another spectrum was recorded revealing that both NBE and DLE stayed nearly constant. Also shorter pauses of irradiation (in other nanowires) did not show any shifts in the irradiation dependence. Thus, there are no significant charging effects that affect the CL signal, as charging would lead to a jump in the CL signal when continuing the irradiation after pausing [410]. Remarkably, also pausing the irradiation and keeping the samples in air did hardly show any effects on the curve progression. After irradiating pristine nanowires for 10 min, the irradiation was paused for different times (10 min to 2 h, respectively). When continuing the irradiation, the curve continued undisturbed. Moving the sample out of the vacuum and keeping it in air for similar time spans also showed no changes. Keeping the sample in air for 18 h finally yielded a slight decrease in NBE intensity (see figure 5.4d).

5.2.2. Possible interaction mechanisms

To discuss these findings in detail, this section aims to introduce the mechanisms that are ascribed to the electron dose dependent luminescence of ZnO. The trend of the NBE signal with proceeding irradiation (increasing at first but decreasing for continuing irradiation) indicates at least two involved processes. In this section, one process that explains the rising luminescence in the beginning of the irradiation and several candidates to explain the subsequent decrease will be discussed.

Desorption of surface species The increase in CL luminescence observed in the beginning of the irradiation can be attributed to electron beam-induced surface desorption processes. Surface adsorbates (mostly O_2), which are always present on the surface of ZnO nanowires [244, 411, 412], can be stimulated to desorb either directly by the electron beam or via recombination with secondary holes (see section 2.5.2) [62]. This leads to a reduction of the band bending at the surface (see also section 2.5.2), which in turn leads to a higher rate of radiative recombination. In that way, the initial increase of the NBE, as observed in figure 5.4d, can be explained. Surface desorption processes also offer an explanation to the increase in DLE. When assuming surface V_O as the key recombination channel for the DLE, its increase can be explained by the electron beam induced activation of surface V_O that were previously passivated by surface adsorbates.

Surface reactions and carbon deposition Electron degradation of several phosphors was already studied in the 1960s (initially for full color cathode ray tubes in TVs). There, the CL degradation of phosphors was described by a phenomenological formula (Pfahnl's Law) [413]. Later on, mechanisms behind this empirical descriptions were identified as electron stimulated surface chemical reactions that are mostly associated with carbon [414–417]. A resulting surface carbon build-up lead to a layer of more than 100 nm thickness, resulting in an attenuation of the incident electron beam and, more importantly, to a strong optical attenuation of the CL signal [418]. Such drastic effects, however, can be ruled out for our experiments, since they require high concentration

of hydrocarbons in the residual vacuum and were negligible above 4 keV [418, 419]. However, also in modern SEMs, hydrocarbon molecules—either from the nanowire surface or from the vacuum chamber—can be cracked by the electron beam leading to the build-up of a thin carbonaceous layer [420–423]. Secondary electrons, however, also balance this build-up via the erosion of carbon from the surface depending on sample temperature, the acceleration voltage, and beam current [423–425]. In several studies, the reduction of the total amount of carbon at the surface was observed during prolonged electron beam irradiation [415–417]. This was explained by electron beam-induced chemical reactions. Such reactions can lead to the creation of volatile species that leave the surface, but they can also induce permanent changes in the surface [414, 417, 426]. As the electron beam-induced chemical surface reactions rely on the available species, vacuum pressure and the composition of the residual vacuum strongly alter the degradation process [426, 427].

These processes can be expected to be enhanced for nanowires due to the large surface-to-volume-ratio. Indeed, for GaN nanowires a sub-monolayer coverage of carbon was found to be able to reduce luminescence by two orders of magnitude [397]. This luminescence reduction could neither be explained by attenuation of primary electrons nor by optical attenuation of the CL signal. Thus, the effect was ascribed to an enhancement of non-radiative surface recombination at surface states induced by carbon adatoms.

Reduction of the surface energy The mechanism for electron-induced surface desorption is similar to the mechanism of persistent photoconductivity that is well known in ZnO, i.e., for irradiating ZnO with UV-light, the photoconductivity rises rapidly but decays slowly when the UV-irradiation is turned off (see section 2.5.2). In contrast to the fully reversible process of persistent photoconductivity, there seems to be a more permanent character of the intensity rise caused by electron irradiation, if one takes into account the findings of Milano et al. [398]. Upon electron irradiation, they found a modification of the wetting properties of ZnO nanowires from hydrophilic to hydrophobic, i.e., a reduction of the surface energy. This is explained by electron beam-induced surface alterations such as the cracking of hydrocarbons and the subsequent build-up of a carbon layer (see above). The observations upon pausing irradiation (see figure

5.4d) already evidenced little or no effect for keeping samples in air after irradiation. This is contrary to observations made after UV-irradiation in vacuum. Typically, re-adsorption leads to a fast recovery when the sample is exposed to ambient air after UV light-induced surface desorption. As we did not observe a fast recovery in air, surface adsorption processes seem to be slowed after electron irradiation. Additionally, upon starting to irradiate samples with the electron beam a second time, the CL signal does not increase in contrast to the increase observed for the initial irradiation. This corroborates the finding of an altered surface after (even a short/low-dose) electron irradiation.

Defect creation In general, defects in the ZnO material can be induced by high energy electron irradiation [399–402]; with rising defect concentration a decrease of the NBE and an increase of the DLE was observed [403]. Defect creation in electron beams can occur via elastic scattering causing atomic displacements and sputtering or via inelastic scattering causing sample heating or radiolysis by the Knotek-Feibelman mechanism [420]. Displacement thresholds, however, were reported to be above 300 keV [428, 429] making defect creation highly unlikely since the acceleration voltages for all experiments in this thesis were between 10 kV to 30 kV. In the SEM, also sputtering is negligible, since it is usually observed at the exit-surface (i.e., the sample surface on the opposite side of the impinging electron beam) in transmission electron microscopes. Electron energies in the SEM are also too low to produce significant heating in ZnO for the parameters used in this thesis [430, 431]. Although there are reports about radiolysis from ZnO resulting in the creation of V_O at the surface, oxygen desorption by radiolysis in ZnO is clearly less prominent compared to other transition metal oxides like TiO_2 [432].

Hydrogen depletion Hydrogen desorption was shown to take place in ZnO already for low electron energies above 1.5 keV by time-of-flight electron-stimulated desorption experiments [433]. Remarkably, the hydrogen desorption was still observed after several hours of irradiation indicating a removal of hydrogen not only from the surface but also from the bulk of the ZnO material. From first principles simulations, hydrogen

in ZnO is known to be a shallow donor and can exist as an interstitial (H_i) but also substitutional on oxygen lattice sites (H_O) or in Zn vacancy-hydrogen defect complexes ($V_{Zn-n}\cdot H$) [165, 270, 281] (see also section 2.5.3). While the energy of electrons in the SEM is not sufficient to generate defects, it is sufficient to dissociate hydrogen defect complexes altering the electronic properties. Therefore, the activation of defects that were formerly hydrogen passivated might well explain an increase in either non-radiative or radiative defect transition and thus the observed decrease in NBE. The effects of the hydrogen depletion on the DLE are more equivocal. On the one hand, the removal of hydrogen can explain an increase in DLE (as observed in figure 5.4c) due to the passivation of non-radiative defects in ZnO [434–437]. This is in line with a frequently observed quenching of the DLE when incorporating hydrogen into ZnO [164, 253, 278, 436, 438]. On the other hand, there are also reports on hydrogen-defect complexes being active radiative recombination centers [165, 427, 439, 440]. In this way, hydrogen desorption could lead to an increase of radiative DLE centers.

5.2.3. Irradiation parameter dependency

To gain further insight into the underlying processes, the irradiation parameters (flux density, acceleration voltage) were varied. Each curve in the following is measured for a different nanowire since the luminescence is altered upon the irradiation and measurement process. Nanowires with similar diameters of ~ 200 nm from the same growth batch were chosen for all experiments; the irradiation area size (see inset in figure 5.4b) was furthermore kept constant. The nanowires were irradiated at different acceleration voltages of 10 kV, 20 kV, and 30 kV. To estimate the interaction volume for electrons in the ZnO nanowires, Monte Carlo simulations were performed¹. Electron irradiation of a 180 nm ZnO film on a silica substrate was simulated (see figures 5.5a-c). The resulting electron hole pair generation rate g spans several orders of magnitude within the interaction volume of the electron beam. To roughly mimic the nanowire geometry, only electron energy losses within a width of 180 nm^2 in the ZnO

¹The simulations were performed using Casino v2.51 [149]. In the simulations, a beam radius of 20 nm was used and 1×10^6 electrons were simulated.

²The $180\text{ nm} \times 180\text{ nm}$ square was chosen to roughly match the cross-sectional area of the nanowires ($d \approx 200\text{ nm}$).

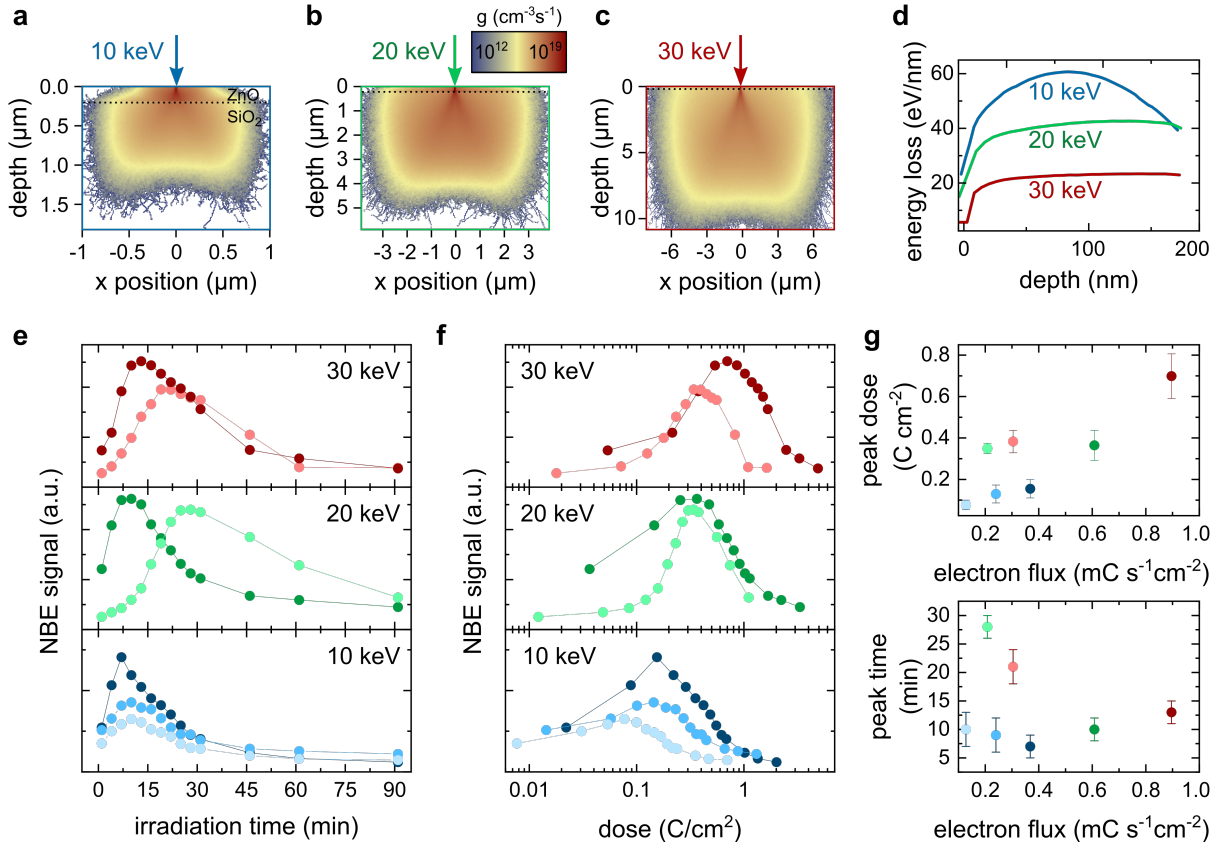


Figure 5.5.: Evolution of the NBE signal as a function of electron irradiation. **a-c** Simulated generation rates in a 180 nm layer of ZnO on silica (simulated with Casino v2.51) for 10 keV, 20 keV, and 30 keV on a logarithmic scale. **d** Penetration depth-dependent energy loss in the ZnO film extracted from the data of (a-c). **e** Time-dependent NBE signal for 30 keV, 20 keV, and 10 keV acceleration voltages (red, green, and blue) and different flux densities (from light to dark: $0.13 \text{ mC cm}^{-2} \text{ s}^{-1}$, $0.24 \text{ mC cm}^{-2} \text{ s}^{-1}$, and $0.37 \text{ mC cm}^{-2} \text{ s}^{-1}$, for 10 keV; $0.21 \text{ mC cm}^{-2} \text{ s}^{-1}$ and $0.61 \text{ mC cm}^{-2} \text{ s}^{-1}$ for 20 keV; $0.30 \text{ mC cm}^{-2} \text{ s}^{-1}$ and $0.90 \text{ mC cm}^{-2} \text{ s}^{-1}$ for 30 keV). **f** Electron irradiation dose dependency of the same data as in (e) on a logarithmic scale. **g** Peak fluence and time, i.e., the fluence or time needed to reach the maximum NBE signal, as a function of electron flux density. Symbol colors match with those in (e) and (f).

film were considered for calculating the penetration depth-dependent energy loss of the photons (see figure 5.5d). As the penetration depth is increasing with electron energy, electrons with 10 keV lose most of their energy within the ZnO film, while for 20 keV and 30 keV the energy loss within the ZnO film reduces. In the experiment, however, absolute intensity values cannot be directly compared due to slightly different nanowire diameters and lengths.

All acquired irradiation time-dependent NBE signals show a similar behavior: an initial increase is followed by a decrease with proceeding irradiation (see 5.5e and f). For increasing electron flux at a fixed energy of 10 keV (lower panel in figure 5.5e), the

peak height of the time-dependent CL signal increases, while the peak time, i.e., the irradiation time needed to reach the peak, slightly decreases. Both trends are also observed for higher electron energies of 20 keV and 30 keV (upper two panels in figure 5.5e). The same data is presented as a function of the electron fluence (on a logarithmic scale) in figure 5.5f. The respective peak time and peak dose were extracted from all curves and brought together in figure 5.5g. In general, the peak dose increases with increasing electron flux density. The peak time shows no systematic flux-dependency over the different acceleration voltages. For 10 keV, 20 keV, and 30 keV, in each case, similar trends are observed with increasing flux density, i.e., an increasing peak dose and a decreasing peak time. This clearly indicates that the underlying processes are neither solely time- nor dose-dependent. Instead, dynamic processes—in analogy to dynamic annealing in ion beam induced amorphization experiments [441–443]—must be considered (see section 5.2.7).

5.2.4. Electron irradiation dependent photoluminescence

The electron beam irradiation experiments were repeated at 10 keV with a flux of $\sim 0.24 \text{ mC cm}^{-2} \text{ s}^{-1}$ and, in addition to the CL measurements, μPL measurements were performed. In contrast to CL measurements, PL allows to acquire non-irradiated spectra (before electron irradiation). Moreover, the optical setup allows to detect PL spectra at distinct positions—decoupled from the excitation—enabling the measurement of waveguiding properties in the nanowires. Additionally, the excitation power density of the laser excitation (and thus the generation rate) can easily be varied over several orders of magnitude allowing to record the excitation power dependency. Nevertheless, taking PL spectra of irradiated nanowires requires pausing the irradiation and taking the samples out of the vacuum. Thus, the samples are exposed to air during PL measurements. Keeping these issues in mind, PL measurements are taken to complement the CL investigations of the last section.

Excitation intensity dependent PL spectra of several nanowires were acquired. The excitation intensities were limited to 1000 W cm^{-2} according to the findings of section 5.1.1 to prevent luminescence quenching. To ensure that consecutive measurements

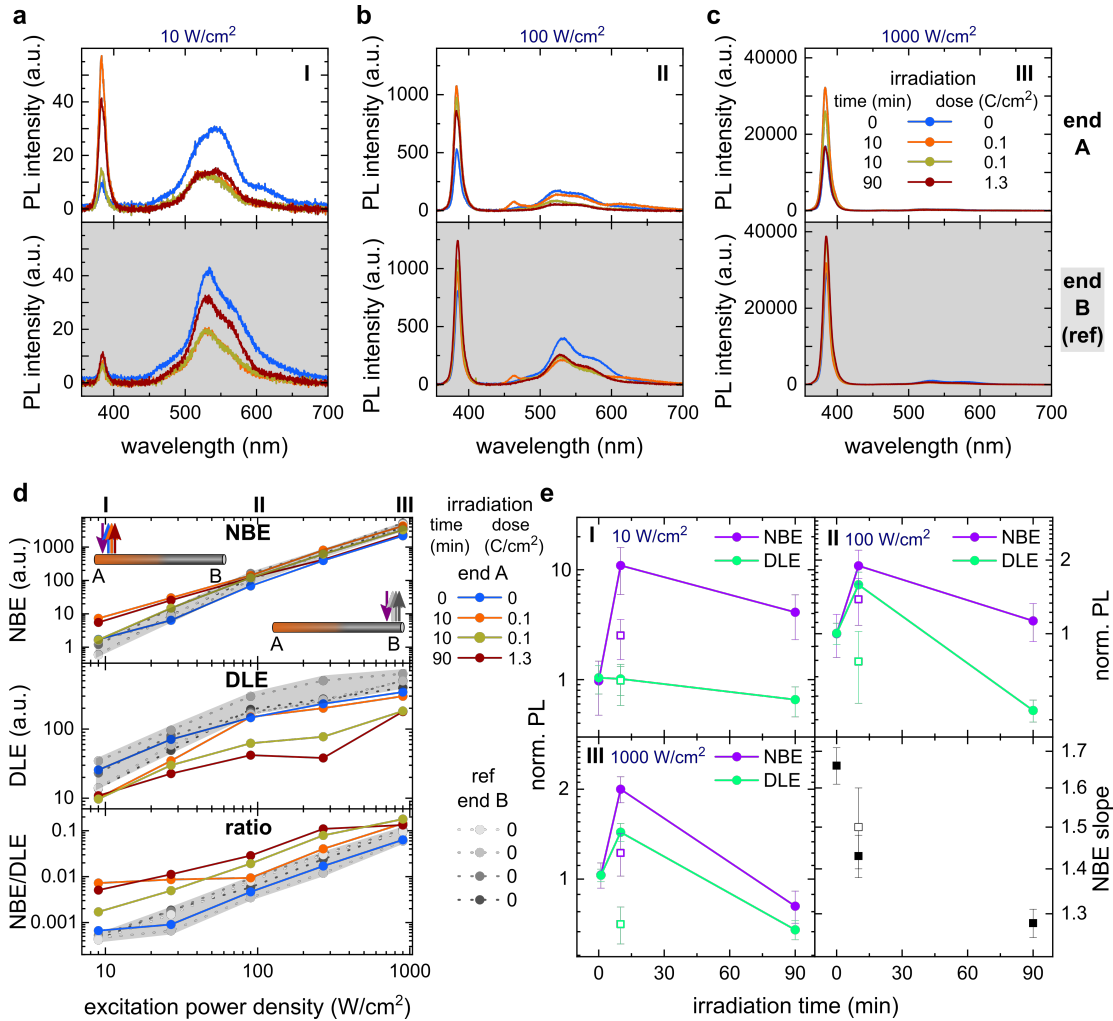


Figure 5.6.: Electron irradiation dependence of the PL. **a-c** Spectra from the irradiated end A (top row) and reference end B (bottom row) taken at excitation intensities of ~ 10 , 100, and 1000 W cm^{-2} . Spectra were measured prior to (blue line), after 10 min (orange), after 10 min and keeping the sample for 5 days at ambient conditions (yellow), and after 90 min (red) of 10 keV irradiation at a flux of $\sim 0.24 \text{ mC cm}^{-2} \text{ s}^{-1}$. The distinct peaks observed in some spectra at $\sim 460 \text{ nm}$ is a measurement artifact. **d** Excitation power density dependency of the NBE, DLE, NBE-to-DLE ratio. The sketches of the nanowire indicate the measurement positions: the colored symbols correspond to the irradiated end A and the gray symbols to reference end B. **e** Irradiation dependent PL (NBE and DLE) signals for ~ 10 , 100, and 1000 W cm^{-2} . The bottom right panel shows the slope of linear regime of the NBE signal from (a).

were all performed at the same position on the nanowire, spectra were always acquired at the ends of the wire; furthermore, the measurement position was fine-tuned and precisely repeated using the piezo-based sample stage. After acquiring PL spectra from both ends of a pristine nanowire (blue spectra in figure 5.6a-c), roughly half the nanowire was irradiated with the electron beam, while the second half served as reference (see scheme in figure 5.4a). The electron dose dependent CL signal acquired

during the irradiation revealed an initial increase with a subsequent decrease, similar to the observations made above; thus, performing PL measurements beforehand does not change the electron irradiation behavior.

The sample was then taken out of the vacuum chamber of the SEM and PL was re-measured. Spectra for different laser excitation power densities were measured before irradiation, after 10 min (corresponding to the CL peak value), and after 90 min of electron irradiation and are shown in blue, orange, and red in figure 5.6a-c for excitation power densities of 10, 100, and 1000 W cm⁻². In addition, after the 10 min irradiation, the sample was kept at ambient air for 5 days and PL was re-measured (yellow curves in figure 5.6a-c). Note that all data shown in figure 5.6 were measured on the same nanowire; repeating these measurements for further nanowires yielded the same trends. The upper row shows spectra from the irradiated end A, while the lower row depicts spectra from the non-irradiated reference end B. Integrating the NBE and DLE signals yielded the power dependency (see figure 5.6d) and the irradiation-dependency (figure 5.6e).

As already discussed above, the relative intensity between NBE and DLE changes with excitation power; more specific, the NBE-to-DLE-ratio increases with increasing excitation power density (see lower graph in figure 5.6d) [174]. As expected, there is no significant difference between the signals from end A prior to irradiation (blue) and the reference data from end B (gray dots). The irradiation-dependencies were normalized to the respective values from end B to account for different time spans in air and small deviations in the optical setup alignment. In all panels of figure 5.6e, an increase of both NBE and DLE is observed for the 10 min irradiation.

The reference spectra (see figure 5.6a-c, lower panels), are almost constant in the NBE for all irradiation times. For 10 W cm⁻², the NBE is clearly constant, while the DLE values vary. This is similar also for the higher excitation powers. The variations in the reference spectra might be attributed to different times the sample spent in air prior to the measurement and the uncertainties in re-aligning the nanowire in the optical setup. In contrast to the nearly constant reference end B, the irradiated end A shows a strong increase in NBE after 10 min of irradiation (orange curves). This behavior is fully consistent with the observations made for the CL signal (see section 5.2.1). Considering that the PL spectra were measured several minutes after taking the

sample out of the vacuum, this hints that there is no fast re-adsorption of ambient gas species in air. The absence of a fast re-adsorption process is consistent with the stability observed when pausing the irradiation in CL (see figure 5.4c and d). This, in turn, corroborates the theory that the surface is long-lastingly modified during electron beam irradiation. Thus, (surface) non-radiative recombination is decreased after the initial 10 min irradiation also when measuring in air.

Keeping the sample for 5 days at ambient air (yellow curves in 5.6a-d and hollow squares in 5.6e) yielded no changes at the reference end B, which allows concluding that purely vacuum-induced effects can be neglected here; at end A, the PL signal decreased compared to the signal measured directly after the 10 min irradiation. This, however, did not lead to a restoration to the initial (blue) spectrum: The NBE signal was reduced but stayed above the pristine value, while the DLE signal dropped to (at low excitation powers) or significantly below (at higher powers) the pristine value. The reduction in both signals indicates that non-radiative recombination rates drastically increase when leaving the sample in air after electron irradiation. This could be attributed to the surface adsorption of oxygen and the subsequent band bending.

Further irradiation (90 min; red spectra and points in figure 5.6a-d) lead to a decrease in the NBE signal. Remarkably, this decrease differs considerably for the different laser excitation power densities, which is clearly reflected in the decreasing NBE slope with increasing electron dose (see bottom right figure in 5.6e). This reduction in NBE slope might hint an increase of non-radiative recombination with increasing electron dose, since the DLE is also reduced after irradiation for all powers [177]. Notably, the slope of the NBE decreased already after the first irradiation step—despite the observed increase in NBE signal. This could be interpreted as a balance between a surface modification process that dominates for low doses and leads to increasing radiative recombination, and a (slower) second process that increases the non-radiative recombination.

In total, the dose-dependency of the NBE coincides well with the results from the CL experiments (compare figure 5.4c). Thus, the change from vacuum to air seems not to play a major role here, when measuring directly after taking the sample out of the vacuum. In contrast to the NBE, the DLE is reduced to well below the starting value at all excitation powers after 90 minutes of electron irradiation (see figure 5.6d and

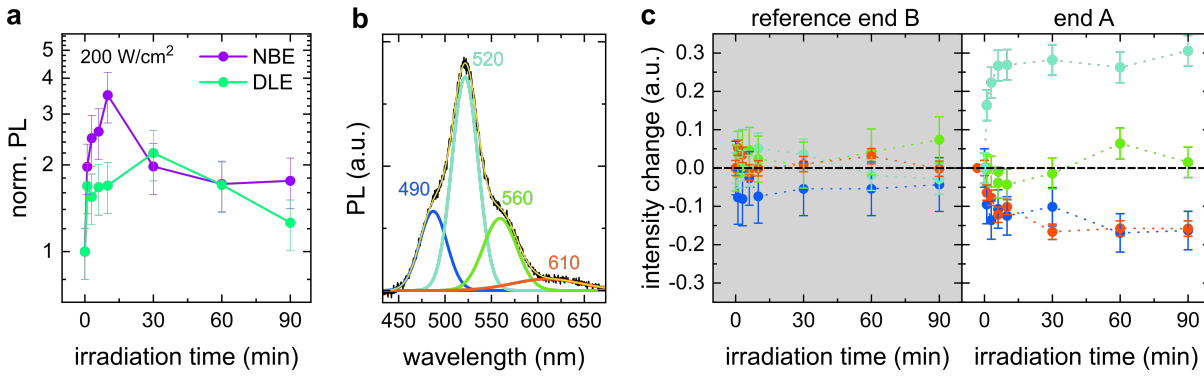


Figure 5.7.: Electron irradiation dependency of the defect luminescence. **a** Evolution of the PL signal after 10 keV irradiation at a flux of $0.02 \text{ mC cm}^{-2} \text{ s}^{-1}$. **b** Defect luminescence fitted with 4 Gaussian functions. This fitting was repeated for all irradiation steps. **c** Change in relative defect peak percentage as a function of electron irradiation. At the reference end B, no significant change is visible; at the irradiated end A, however, the 520 nm emission line shows an increase of ~ 30 percentage points in relative intensity while the 490 nm and 610 nm lines both decrease ~ 15 percentage points.

e). This is also opposed to observations for the electron beam dose dependent DLE signal from the CL measurements (compare figure 5.2.1c). There, the signal increased and saturated at ~ 8 times the starting value. On the contrary, for PL measurements, keeping the samples for 5 days in ambient air decreased the DLE further, strongly indicating that the differences between PL and CL arise from the different ambient (air or vacuum). This further insinuates that also for the DLE (at least) two competing processes contribute to the electron dose dependency. The increase in the beginning originates most likely from an overall decrease of non-radiative recombination since, along with the DLE, the NBE increases for low doses (due to the reduction of the band bending).

The experiments were repeated at lower electron fluxes of $0.02 \text{ mC cm}^{-2} \text{ s}^{-1}$. For each irradiation step, PL spectra were recorded at both end facets at 200 W cm^{-2} . The irradiation time-dependency (see figure 5.7a) corroborates the findings from the PL measurements above: While the NBE shows a similar trend as observed in CL, the DLE trend deviates from the CL results for higher irradiation doses. This confirms that a significant fraction of the mid-gap states that give rise to the DLE is closely related to the ambient conditions [244, 245]. A closer look at the DLE was taken by fitting the spectrum with multiple Gaussian functions (figure 5.7b), each arising from a different deep defect level (see section 2.5.3). All spectra were fitted with four Gaussian curves centered at the wavelengths indicated above. This multi-peak fitting was repeated after

each irradiation step, yielding the relative intensity change

$$\Delta R_I = \frac{I_\lambda(t)}{I_{\text{tot}}(t)} - \frac{I_\lambda(t=0)}{I_{\text{tot}}(t=0)}, \quad (5.2)$$

where t is the irradiation time, I_λ is the intensity of a transition with the central wavelength λ , and I_{tot} is the total DLE signal. On the reference end B, no significant changes were observed during irradiation (see figure 5.7c, left panel). But on the irradiated end A, strong changes with proceeding electron irradiation become apparent (see figure 5.7c, right panel): While the intensity of the 560 nm transition stays almost constant, the 490 and the 610 nm transitions reveal a decrease in ΔI , and the 520 nm transition increases. Note that for the NBE, neither a change of the spectral shape nor a shift of the NBE peak position was observed. These observations for the DLE agree with the findings of Ton-That et al. after hydrogen doping [164]: They observed that the 520 nm line vanishes and found an increase of the 490 nm line after H incorporation. This hints that the processes that change the DLE might be related to hydrogen, which in turn is in excellent agreement with observations that electron irradiation in ZnO leads to a desorption of hydrogen (see section 5.2.2).

As described in section 2.5.3, V_{Zn} -related radiative transitions most likely arise from $V_{\text{Zn}}-\text{n}\cdot\text{H}$ complexes. Assuming an electron irradiation-induced dissolution of the $V_{\text{Zn}}-\text{n}\cdot\text{H}$ complexes, the radiative luminescence from the defects should thus decrease since V_{Zn} gives mostly rise to non-radiative transitions according to first principles calculations and experiments. [153, 165, 281, 285, 286]. Consequently, the decreasing transitions could be related to the dissociation of $V_{\text{Zn}}-\text{n}\cdot\text{H}$ defect complexes. Similarly, one could assign the increasing 520 nm transition to a hydrogen-passivated defect, e.g., V_{O} . However, these assignments contradict that of Ton-That et al. They attributed the 490 nm transition to V_{O} as they observed this transition in Zn-rich grown samples and the 520 nm line to V_{Zn} as they observed it in O-rich grown samples. Furthermore, no additional defect transitions at lower energies were observed in any PL spectra. Such transitions were observed after high energy electron irradiation [403] and can be ascribed to V_{Zn} and $V_{\text{Zn}}-\text{H}$ complexes [165]. Not observing such transitions thus contradicts the $V_{\text{Zn}}-\text{H}$ complex dissociation hypothesis.

Apart from hydrogen-related processes, surface desorption processes could also cause

such a change in relative intensities of the different defect transitions. The irradiation time(dose)-dependence of the defect transitions in figure 5.7c shows a strong and fast increase in the beginning of the irradiation and is almost constant for proceeding irradiation. This contradicts the finding that the hydrogen desorption continued constantly also for prolonged electron irradiation [433, 444]. Partly this could be explained by the smaller material volume in the nanowires and the greatly enhanced surface-to-volume-ratio compared to bulk. In the experiments, the electron beam fully penetrated the nanowire and the energy loss in the nanowire was almost independent of the penetration depth (see figure 5.5a-d). Thus, the nanowire does not have a “hydrogen reservoir” in a deeper layer as it was observed for bulk ZnO [433, 444]. Furthermore, a hydrogen-related process would still be expected to be less abrupt. A surface desorption-process, however, could well explain the fast changes [109, 232]. This is consistent with the equally fast initial increase of the NBE that is also explained by surface desorption. Following this hypothesis, the 520 nm emission could be attributed to V_O and the 490 nm and 610 nm transitions to adsorbed oxygen species.

5.2.5. Electron irradiation of nanowire lasers

The effects of electron irradiation were finally also investigated in the stimulated emission regime. For this purpose, first the PL power dependency of several pristine nanowires was measured. The samples were then successively irradiated in the SEM (here: the whole nanowire) and the power dependency of the PL emission was re-measured after each step. To ensure similar excitation conditions for the successive optical measurements, the alignment of the optical setup and the positioning of the sample with respect to the laser beam were kept constant.

Lasing spectra taken at an fixed excitation power of $\sim 2 \cdot TH_{\text{lasing}}$ of the pristine wire show a drastic decrease already after short irradiation times (see figure 5.8a). After 30 min ($\sim 0.42 \text{ C cm}^{-2}$) of irradiation, the Fabry-Pérot modes were almost completely quenched (dark red line). To compare this to the observations in the spontaneous regime from section 5.2.4, the Fabry-Pérot modes were integrated as well as the spontaneous emission background (see figure 5.8b). In agreement with previous observations

in CL and PL, the spontaneous emission slightly increases initially and subsequently decreases. In stark contrast, the integrated lasing signal decreases by ~ 3 orders of magnitude.

A more precise picture of the electron beam-induced degradation of the stimulated emission was gained by fitting the respective power dependencies with a multimode lasing fit [201]. This reveals an threefold increase of the lasing threshold with proceeding irradiation (see figure 5.8c). Along with the lasing threshold, the spontaneous emission parameter x_0 increases after irradiation. This can be explained by the decrease of the lasing modes while the spontaneous emission stays roughly constant. This also explains the remarkable observation that the fit quality increases with electron irradiation: The relative increase of the spontaneous emission balances the differing detection efficiencies for spontaneous and stimulated emission (see also the discussion in section 5.1.2). The increase of the lasing threshold as a function of irradiation was analyzed for further nanowires and is shown in figure 5.8d. In all cases, a strong increase of the lasing threshold is visible. Most of the threshold increase occurs in the first irradiation step; therefore, also short irradiation times and low electron doses already drastically influence the lasing properties. Upon further electron irradiation, the threshold finally increases to 3 to 6 times the value of the pristine nanowire. The rate of increase reduces and the trend seems to saturate for prolonged irradiation.

In short, while the spontaneous emission stays almost constant, the stimulated emission is drastically reduced by electron irradiation. A key difference between spontaneous emission and lasing is—besides the different excitation power regime—that for lasing light has to be guided through the nanowire to be reflected at the end facet such that the net gain allows overcoming the losses. One possible explanation for the increasing threshold with proceeding irradiation could thus be increased waveguiding losses. Therefore, the electron irradiation dependency of waveguiding is addressed in more detail in the following.

5. Stability of photonic nanowire devices

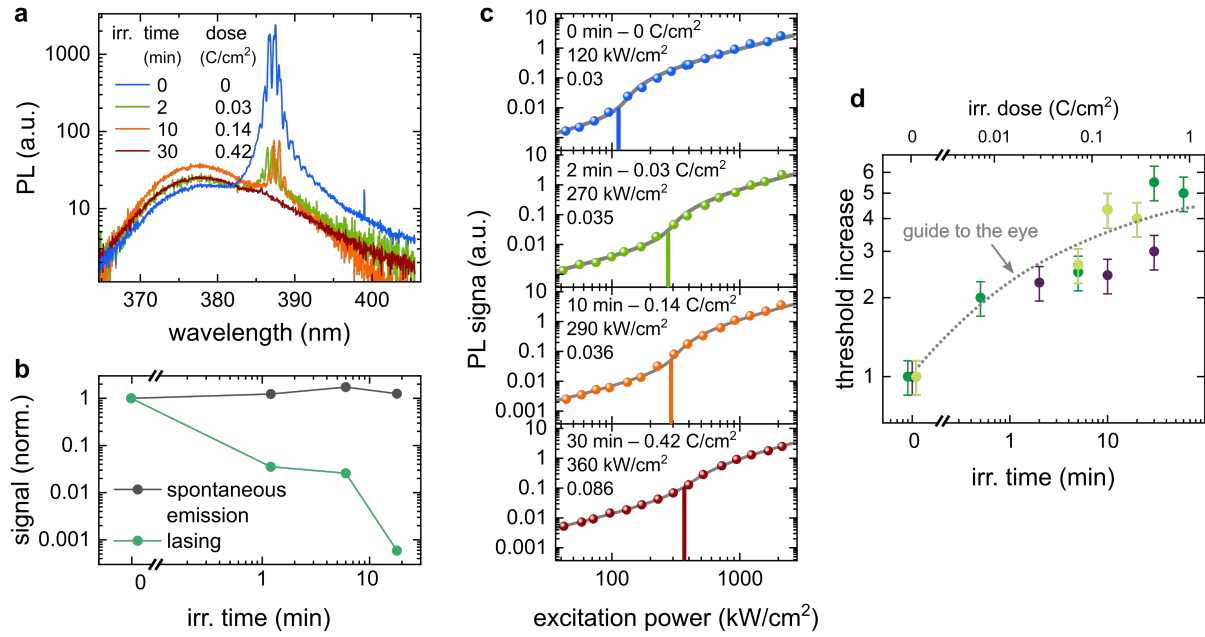


Figure 5.8.: Lasing as a function of electron irradiation. **a** Lasing spectra prior, after 2 min, 10 min, and 30 min of 10 keV electron irradiation at a flux of $\sim 0.24 \text{ mC cm}^{-2} \text{ s}^{-1}$. All spectra were acquired at a similar excitation intensity of $\sim 240 \text{ kW cm}^{-2}$, which is roughly $2 \cdot \text{TH}_{\text{lasing}}$ of the pristine wire. **b** Integrated spontaneous emission (black) and lasing modes (green) from the spectra in (a). While the spontaneous emission stays roughly constant, the lasing modes are quenched drastically. **c** Excitation power dependency of the nanowire laser emission with increasing irradiation. The threshold values are marked as vertical lines in all curves. The respective legends indicate (from top to bottom) the irradiation time and dose, the threshold power, and the spontaneous emission parameter x_0 . **d** Increase of the threshold with irradiation for the nanowire from (a-c) (purple) and 2 different nanowire lasers normalized to the respective pristine threshold.

5.2.6. Electron irradiation dependent waveguiding

Waveguiding measurements were performed similar to section 5.2.4 upon electron irradiation. A lower electron flux compared to prior experiments of $0.02 \text{ mC s}^{-1} \text{ cm}^{-2}$ was used, since already small electron doses resulted in strong threshold increases. Beside that, similar irradiation parameters were chosen. The nanowire was excited with a tightly focused laser at ends A and B as well as in the middle (M) for all irradiation steps. Subsequently, the PL from the spot as well as the waveguided emission at the end facets were detected (see figure 5.9a). Note that $\sim 40\%$ of the nanowire were irradiated with the electron beam such that the spot M stayed pristine. As discussed in section 2.3.3, the NBE signal is red-shifted during the waveguiding due to the absorption-emission-absorption process in the Urbach tail states. The

waveguiding was measured for light guided from end A to end B (A→B), from the middle M to end B (M→B) as well as from end B to end A (B→A), and the middle M to end A (M→A) (sketched in figure 5.9b). The peak wavelength shift from these waveguiding processes is displayed in figure 5.9c for proceeding irradiation. There is a somewhat lower redshift for waveguided light detected at end B compared to light detected at end A; this could stem from a slight tapering of the nanowire leading to a different confinement factors. However, there is no clear trend upon increasing electron irradiation. Thus, the absorption by the Urbach tail states is not influenced noticeably during electron irradiation.

The NBE and DLE signals were integrated and the waveguiding transition efficiency was calculated by normalizing the waveguided signals with the signals measured at the excitation spot (see figure 5.9d). As expected, the waveguiding efficiency for light that is guided through the non-irradiated part (M→B; light blue points) stays constant. The other 3 signals show a slight increase followed by a strong decay by more than one order of magnitude. The slight increase in the beginning cannot simply stem from an increase of PL at the excitation spot, as it is observed in all 3 curves (keeping in mind that the excitation spots M and B are not irradiated). Additionally, the transition efficiency is normalized to the signal at the excitation spot. The increase thus can be connected to surface desorption and the subsequently reduced non-radiative surface recombination, which was a major result of section 5.2.4. But for prolonged irradiation (at doses of $\sim 0.1 \text{ C cm}^{-2}$), the 3 waveguiding signals drastically reduce, i.e., the waveguiding losses increase. This is in good agreement with the findings from the lasing measurements where the lasing threshold was more than doubled for similar electron doses of $\sim 0.1 \text{ C cm}^{-2}$ (compare figure 5.8d).

Analyzing the DLE yields similar results but with a much larger signal-to-noise ratio due to the weaker signals (not shown). Instead, the Fabry-Pérot modes superimposed to the DLE signal (see inset of 5.9a) were used to study the effects of the electron irradiation on the waveguiding properties of the DLE. The Fabry-Pérot modes are extremely sensitive to changes in the waveguiding losses, as they depend on multiple reflections of light at the nanowire end facets. For all irradiation steps, the defect emission background was subtracted, yielding solely the Fabry-Pérot modes (see figure 5.9e). The FFT amplitude was calculated in an 10 nm interval around 500 nm

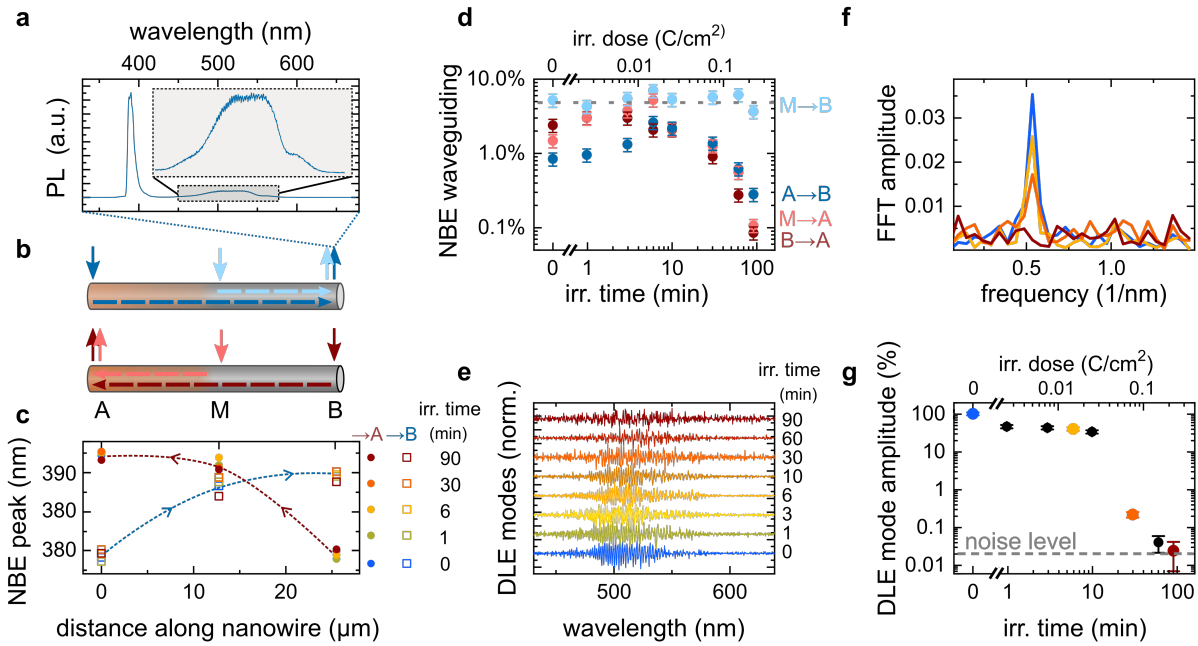


Figure 5.9.: Waveguiding as a function of electron irradiation. **a** Waveguided spectrum collected at end B after exciting the nanowire at end A. **b** Scheme of the measurement configuration. **c** NBE peak shift as a function of traveled distance in the nanowire. The hollow squares were acquired at end B upon excitation at positions A, M, and B. The full circles were acquired at end A upon excitation at positions B, M, and A. The x-axis matches the positions of end A (at 0 μm), M (at 13 μm) and end B (at 26 μm) as marked in (b). The dashed lines are guides to the eye and the arrows give the respective direction of the waveguiding. Irradiation at 10 keV with a flux of $0.02 \text{ mC cm}^{-2} \text{ s}^{-1}$ for irradiation times (color coded as indicated in the legend) yielded no significant changes. **d** The respective electron irradiation dependence of the integrated NBE intensity in the waveguided spectra. The intensity of light guided through the non-irradiated part of the wire (M \rightarrow B) stays constant with irradiation, while the intensity of light that is guided through the irradiated part drastically decreases. **e** Fabry-Pérot modes in the visible spectral range for the same nanowire as in (a-d). The defect luminescence (see inset in (a)) was subtracted to bring out the superimposed modes more clearly. **f** For all spectra in (e), a FFT analysis between 490 nm and 510 nm revealed a distinct peak at $\sim 0.5 \text{ nm}^{-1}$. **g** The DLE mode amplitudes from (f) were normalized to the pristine value and are shown as a function of irradiation. The modes strongly decrease until the noise level is reached after 90 min of irradiation.

for all curves to allow for a clear distinction from noise (figure 5.9f). Note that a relatively narrow interval must be chosen as the mode spacing slightly changes with wavelength. For the pristine nanowire (blue curve), a clear peak in the FFT amplitude is observed at $\sim 0.53 \text{ nm}^{-1}$ corresponding to an average mode spacing of 1.9 nm. Using equation 2.7, with a refractive index of 2.1, and a dispersion of $\sim -0.82 \mu\text{m}^{-1}$ at a wavelength of 500 nm [445], the resonator length is calculated to $(25 \pm 1) \mu\text{m}$, which matches the nanowire length of $(24.4 \pm 0.3) \mu\text{m}$ that was measured via SEM. With increasing electron irradiation, the mode spacing does not change noticeably. This

allows concluding that the refractive index stays constant within a measurement uncertainty of ~ 0.1 . Yet, the FFT mode amplitude decreases considerably already for the first irradiation step (2.5 mC cm^{-2}). Above 20 mC cm^{-2} the mode amplitude decreases even faster by several orders of magnitude until the Fabry-Pérot modes are fully quenched to the noise level (figure 5.9g).

Thus waveguiding is strongly mitigated even by low electron doses for both the NBE and the DLE. At the same time, the PL signal at the excitation spot remains roughly constant (or is even slightly increased). This agrees with the findings in the stimulated emission regime (see figure 5.8b). Enhanced waveguiding losses thus clearly contribute to the strong increase in lasing threshold after electron irradiation. This might be due to an enhanced non-radiative recombination due to the electron-induced hydrogen depletion, which is consistent with the observation of a threshold decrease to one fifth of the initial value when incorporating hydrogen into ZnO thin films [279]. On the other hand, also the formation of non-radiative surface defects due to electron beam-induced chemical surface reactions could explain this observation: An electron beam-induced carbonaceous surface layer was connected to luminescence quenching due to the formation of non-radiative recombination centers at the surface [397].

5.2.7. Summarizing discussion of the electron irradiation

Several mechanisms that might add to the complex behavior of the optical properties were introduced in the last sections. In the following, experimental observations and possible explanations are summarized:

1. An initial increase of the spontaneous luminescence (both NBE and DLE) was observed for irradiating previously pristine nanowires. The initial increase is explained by an electron-induced desorption of surface-adsorbed species, mostly oxygen.
2. The initial increase is not reversible within several hours in air (as it would be expected for the re-adsorption of gaseous species to a pristine ZnO surface in air [238, 240, 241]), strongly indicating changed surface dynamics. This is explained

by electron beam-induced chemical surface reactions such as the agglomeration of carbon at the surface.

3. Along with the initial increase, the relative intensity of the DLE transition lines changed. This is attributed to a change in deep defect states, e.g., the desorption of oxygen previously adsorbed to surface oxygen vacancies. Notably, no further DLE lines appear at lower energies, as would be expected for the activation of V_{Zn} and V_{Zn-H} due to hydrogen depletion. Thus, $V_{Zn-n}\cdot H$ complexes cannot have been altered in significant numbers.
4. For proceeding irradiation, the NBE starts decreasing, while the DLE stays constant (vacuum) or decreases (air). The decrease of both signals is attributed to an enhanced non-radiative recombination rate, which could stem from the electron beam induced activation of previously hydrogen-passivated defects or from electron beam activated non-radiative surface recombination centers. The DLE staying constant in vacuum while decreasing in air indicates the contribution of surface defects.
5. For stimulated emission and waveguiding (both of NBE and DLE), no initial increase was observed. Instead, both—lasing as well as waveguiding—started decreasing drastically even after short irradiation times and low doses. This is attributed to enhanced non-radiative waveguiding losses.
6. No significant shift in the mode spacing was observed (neither for the lasing nor for the DLE modes). Thus, the refractive index does not change significantly upon electron irradiation.

All in all, the observations can be explained by the dynamic interplay of at least two effects. Surface desorption processes and the resulting reduction of the surface band bending are initially dominating for the spontaneous emission. Subsequently, they are surpassed by an enhancement of non-radiative recombination for prolonged irradiation. As it requires light to pass through the nanowire several times, the waveguiding is affected much stronger by the electron irradiation, which leads to a monotonous fast decrease of the waveguiding efficiency. The stimulated emission is similarly affected by the enhancement of non-radiative recombination. The probable explanations for the increase of non-radiative recombination are the activation of previously hydrogen

passivated defects along with the activation of non-radiative surface recombination centers.

Due to the likely role of intrinsic defects in this mechanisms, growth conditions (e.g., being oxygen-rich and zinc-rich or vice versa) and post-growth treatments could influence the resistance against electron irradiation. For hydrothermally grown ZnO, Li is a well-known amphoteric defect that in turn forms defect complexes with V_{Zn} , which could dissociate upon electron irradiation [446]. Thus, hydrothermally grown ZnO might behave differently under electron irradiation [447]. Similarly, other unintentional dopants could affect the optical properties of ZnO after electron irradiation [268].

5.3. Conclusion

In this chapter, the stability of nanowire lasers upon optical pumping and electron irradiation was studied. The optical emission was characterized from nanowires in the spontaneous and the stimulated emission regime. Upon high intensity laser irradiation above the lasing threshold, CdS and ZnO nanowires show stimulated emission. However for even higher pump intensities, a deviation from the lasing behavior was observed. Passing this degradation threshold finally leads to the full quenching of stimulated emission due to a degradation of the gain material. Measuring lasing and degradation thresholds as a function of temperature in CdS nanowires allowed to predict the high temperature limit for lasing of 470 K; this is the maximum temperature that allows stable laser emission as the degradation threshold surpasses the lasing threshold for higher temperatures. The degradation threshold is highly dependent on the material system, pump conditions and sample configuration.

Upon electron irradiation in an electron microscope, the spontaneous emission of ZnO revealed an initial increase due to the desorption of surface species. Furthermore, slowed surface adsorption dynamics were observed and ascribed to the formation of hydrocarbons on the ZnO surface. Prolonged electron beam irradiation lead to a slight decrease of the nanowire's spontaneous luminescence. The effects of electron irradiation on the spontaneous luminescence were weak, however, compared to the changes of the waveguiding properties. Light guided through the nanowire (i.e., ex-

cited at one end and measured at the other) revealed a drastic decay with proceeding electron irradiation. Likewise, the stimulated emission underwent a drastic increase of the lasing threshold after electron irradiation. This was attributed to electron activated non-radiative recombination processes. The impact of non-radiative recombination enhancement effects on waveguiding and lasing is far stronger than on the spontaneous emission since light needs to effectively travel through the nanowire to be detected (waveguiding) or reflected at the end facets to form Fabry-Pérot modes (lasing).

6. Conclusion and outlook

The overarching aim of this thesis was the investigation of the operation, stability, and degradation behavior of active semiconductor nanowire devices. Integrating nanowire-based building blocks into real-world applications requires a fundamental understanding of their working range and limitations. Therefore, such insights were gained by applying advanced synchrotron nanobeam-based and optical characterization techniques to semiconductor nanowire optoelectronic and all-optical devices; furthermore, the major stability-limiting factors that contribute to the device degradation were identified. This may allow implementing superior nanowire device designs to overcome current limitations for enabling the future use of semiconductor nanowires in active on-chip devices.

In **chapter 4** GaAs nanowires with an axial p-n junction were demonstrated to function as high-spatial resolution X-ray detectors. Internal electrical fields and hot electron effects were observed at the nanoscale using advanced in-operando X-ray analytical techniques based on a focused X-ray nanobeam.

A vapor-liquid-solid-grown axial p-n homojunction GaAs nanowire (Zn and Sn-doped) was transferred to a SiO₂/Si substrate and electrically contacted by metal contacts. This allowed recording the X-ray beam induced current (XBIC) signal along with the X-ray fluorescence (XRF) signal by raster scanning the sample in an X-ray nanobeam. Using the nanowire as an X-ray detector enabled a high spatial resolution of 200 nm × 150 nm limited by the spatial extent of the p-n junction and the nanowire diameter. As there is no immediate limitation for engineering these nanowire parameters, a direct scanning spatial resolution of tens of nanometers might be possible in a similar device.

Varying the incident X-ray energy across the Ga-K edge allowed to simultaneously ac-

quire energy-dependent XRF and XBIC signals. In this way, incident energy-dependent maps of both signals were measured as a function of applied bias voltage. Increasing the bias voltage in reverse direction increased the detector efficiency; however, it also lead to a reduced detector resolution as observed via in-operando XBIC. Finally reverse voltages of -2 V and -5 V lead to a device degradation as observed in a shift of the X-ray absorption edge in the n-type segment of the nanowire. X-ray absorption near edge structure (XANES) spectra were recorded along the nanowire, revealing the degradation mechanism: a selective oxidization in the n-type segment of the nanowire, while the p-type segment stayed pristine. This was identified as the Ga coordination of the oxidized n-type region became octahedral in contrast to the non-oxidized p-type segment that maintained the tetrahedral coordination of GaAs. The selective oxidization of the n-type segment was attributed to the cooling of hot electrons via multiple scattering processes; in the p-type segment, those effects are hindered by the low hole mobility and the strong surface recombination rate in p-type GaAs. This finally resulted in the selective oxidization of the n-type segment of the nanowire X-ray detector and the degradation of the device. The nanowire geometry strongly supports the oxidization due to its reduced thermal conductivity and the large surface-to-volume ratio.

To improve the stability of the nanowire X-ray detector, an oxygen-free measurement environment could be chosen, such as He atmosphere [353] or vacuum. For device application, the passivation of the surface with a capping layer is the more suitable approach. While adding fabrication complexity, it could not only prevent oxidization but also enhance the charge carrier collection efficiency by the suppression of non-radiative surface recombination [336, 341, 448]. But on the other hand, this would reduce the detector resolution and hot carrier effects still would be a limiting factor for applying bias voltages in reverse direction.

The capabilities of the combinatory approach—i.e., the simultaneous detection of XFR, XBIC, and XANES—should be extended in future studies to include further characterization techniques such as X-ray excited optical luminescence to enhance the level of available information. In addition, the high penetration depth as one of the key strengths of X-ray based characterization methods can be used in future studies to investigate buried structures in complex devices. In this way, multimode synchrotron

nanobeam-based analysis techniques will allow gaining deep insights into the operation and stability of nanoscale building blocks in complex devices. Fourth-generation synchrotron sources will add to this development with their enhanced coherence and brilliance [449].

In **chapter 5** the operation and stability of nanowire lasers and waveguides were investigated. The optical emission from nanowires was studied focusing on the effects of high laser powers, and the irradiation with electrons in an electron microscope.

VLS-grown ZnO and CdS nanowires showed stimulated emission upon high intensity laser irradiation. At even higher excitation intensities, however, a decreasing emission intensity up to the total quenching of stimulated emission was observed—the permanent degradation of the nanowire laser. The threshold power for this degradation was found to be decreasing with temperature, while the lasing threshold increased. Thus, a critical temperature—i.e., the temperature above which no stable lasing was possible as the degradation threshold surpassed the lasing threshold—of 470 K was identified for CdS nanowire laser. The degradation mechanism was ascribed to a non-thermal bond softening by the electron-hole-plasma; in combination with the excitation laser induced thermal heating, this led to the desorption of lattice atoms. The degradation threshold of ZnO nanowires was found to be higher than for CdS, which can in part be explained by the lower Phillips ionicity of ZnO. In general, the degradation threshold strongly depends on the material system but also on experimental conditions such as the thermal dissipation in the sample and the optical pumping.

ZnO nanowires were further investigated regarding their stability upon electron irradiation. The spontaneous and stimulated emission as well as the waveguiding were measured prior and as a function of electron beam irradiation dose and time. Upon electron beam irradiation in an electron microscope, the spontaneous emission initially increased, which was ascribed to the desorption of surface species. This led to a decreasing surface band bending and, in turn, to an enhanced luminescence. Slowed surface re-adsorption dynamics were ascribed to hydrocarbons forming at the nanowire surface enabled by the electron beam. For proceeding electron irradiation, a slight decrease of the spontaneous emission was found. These observed changes, however, were weak in comparison to the effects of electron irradiation on the waveguiding

properties: A drastic decay of the light guided through the nanowire was observed with proceeding electron irradiation. Also the stimulated emission suffered a strong reduction upon electron irradiation of the nanowire. This was ascribed to non-radiative recombination processes activated by the electron beam irradiation. The enhanced non-radiative recombination rate heavily suppresses the active waveguiding process, leading to stronger losses in the nanowire lasers and consequentially an increasing threshold.

Both high intensity laser irradiation and electron irradiation severely affect the optical properties of semiconductor nanowires. To ensure stable laser operation, optical pump intensities must be kept below the degradation threshold of the material system in use. For electron irradiation, no such threshold was found; thus, electron irradiation (and thus SEM imaging) must be avoided for nanowire lasers to sustain the laser threshold. However, the altered surface properties after electron irradiation could also be beneficial in some cases to lower chemical degradation [398]. Adding a protective shell layer might improve the nanowire stability with respect to electron irradiation and optical pumping [79, 232, 261, 262].

In future experiments, a deeper understanding of the electron irradiation effects could be gained by comparing the irradiation of oxygen-deficient to zinc-deficient ZnO nanowires. In this way, the role of different intrinsic defects might be revealed. Understanding the contribution of hydrogen to the altered optical properties after electron irradiation may yield insights into the challenges connected with a stable p-type doping of ZnO [450]. Furthermore, a plasma treatment could reverse some effects of the electron irradiation: H plasma treatment in ZnO was shown to enhance the NBE and quench the DLE by passivation of the surface and hydrogen incorporation [451]. Similar results were achieved using an O₂ plasma treatment (in combination with an annealing step) [300]. Finally, Ar plasma treatment was found to remove surface contamination [452] and incorporates H [278]. An appropriate plasma treatment should thus be investigated in future experiments to neutralize the effects of the electron irradiation and thus restore efficient waveguiding and low-threshold lasing. This would allow sample inspection and selection using electron microscopy, and sample preparation using electron lithography without impairing the nanowire laser.

Also the irradiation of nanowires with different ions is worth investigating with respect to defect-creation and the resulting optical properties [251, 407, 408]. Similar to the electron-beam irradiation, the large surface-to-volume ratio in nanowires could make them drastically more sensitive also under irradiation with various ion species.

For optically pumped nanowire lasers, facilitating heat transport by a highly thermal conductive substrate can increase the degradation threshold and thus the high temperature limit for lasing. However, also changing the pulse duration from the ns to the ps or the fs-range might help achieving stable laser emission. Note that comparing absolute threshold values between the different pump pulse duration regimes makes no sense due to the vastly different temporal dynamics [379, 453]. Short laser pulses in the ps and fs-regime drastically reduce the heating of the nanowire [386, 387] and thus allow for efficient pumping even in non-resonant conditions [454].

In conclusion, semiconductor nanowires were shown to be highly functional building blocks for the miniaturization of future optoelectronic and all-optical devices. As identified in this thesis, the miniaturization to the nanoscale, however, poses several challenges beyond device fabrication. The key limitations for a stable nanodevice operation were identified as the reduced thermal conductivity facilitating the built-up of heat and the large surface-to-volume ratio facilitating the surface-related device degradation. These insights are urgently needed for developing schemes to overcome the stability challenges associated to the nanoscale. This comprises a sophisticated thermal management and a dedicated control of the surface properties, both essential for the stable long-term operation of complex nanoscale devices. Together with a high-throughput fabrication, this is an essential step towards integrating nanoscale building blocks into next-generation active real-world applications.

Bibliography

- [1] Bayda, S.; Adeel, M.; Tuccinardi, T.; Cordani, M.; Rizzolio, F. *Molecules* **2019**, *25*, 112 (cit. on p. 5).
- [2] Roco, M. C. *Journal of Nanoparticle Research* **2011**, *13*, 427 (cit. on p. 5).
- [3] Isigonis, P. et al. *Small (Weinheim an der Bergstrasse, Germany)* **2020**, *16*, e2003303 (cit. on p. 5).
- [4] Drexler, K. E., *Engines of creation: The coming area of nanotechnology*; Anchor Books: New York, 1990 (cit. on p. 5).
- [5] Giles, J. *Nature* **2004**, *429*, 591 (cit. on p. 5).
- [6] Stevens, A.; Forgan, D.; James, J. O. *International Journal of Astrobiology* **2016**, *15*, 333 (cit. on p. 5).
- [7] Lloyd, J. *Issues in Science and Technology* **2019** (cit. on p. 5).
- [8] Müller, K. H.; Kulkarni, J.; Motskin, M.; Goode, A.; Winship, P.; Skepper, J. N.; Ryan, M. P.; Porter, A. E. *ACS nano* **2010**, *4*, 6767 (cit. on p. 5).
- [9] Royal Society United Kingdom. Royal Academy of Engineering, Ed. *Nanoscience and Nanotechnologies: Opportunities and Uncertainties*, 2004 (cit. on p. 5).
- [10] Son, D. et al. *Nature nanotechnology* **2014**, *9*, 397 (cit. on p. 5).
- [11] Atlam, H. F.; Walters, R. J.; Wills, G. B. In *Proceedings of the 2018 2nd International Conference on Cloud and Big Data Computing - ICCBDC'18*, ed. by Unknown, ACM Press: New York, New York, USA, 2018, pp 71–77 (cit. on p. 5).
- [12] Wright, J. *Nature* **2014**, *509*, S58 (cit. on p. 5).
- [13] Seil, J. T.; Webster, T. J. *International Journal of Nanomedicine* **2012**, *7*, 2767 (cit. on p. 5).
- [14] Nasrollahzadeh, M.; Sajadi, S. M.; Sajjadi, M.; Issaabadi, Z. In *An Introduction to Green Nanotechnology*, Isaabadi, Z., Sajjadi, M., Atarod, M., Sajadi, M. S., Nasrollahzadeh, M., Eds.; Interface Science and Technology, Vol. 28; Academic Press: 2019, pp 113–143 (cit. on p. 5).

- [15] National Science and Technology Council, Ed. National Nanotechnology Initiative - Strategic Plan, 2016 (cit. on p. 5).
- [16] Roco, M. C. In *Nanotechnology commercialization*, Wang, B., Bothun, G., Winter, J., Mensah, T. O., Davis, V., Eds.; John Wiley & Sons: Hoboken, NJ, 2018, pp 1–23 (cit. on p. 5).
- [17] Ma, R.-M.; Oulton, R. F. *Nature Nanotechnology* **2019**, *14*, 12 (cit. on pp. 5, 7, 61, 72).
- [18] *Semiconductor Nanowires II: Properties and Applications*; Shadi A. Dayeh, Anna Fontcuberta i Morral, Chennupati Jagadish, Ed.; Semiconductors and Semimetals; Elsevier: 2016 (cit. on p. 5).
- [19] Zhang, G.; Rainville, C.; Salmon, A.; Takiguchi, M.; Tateno, K.; Gotoh, H. *ACS nano* **2015**, *9*, 10580 (cit. on pp. 5, 8).
- [20] Barrigón, E.; Heurlin, M.; Bi, Z.; Monemar, B.; Samuelson, L. *Chemical reviews* **2019**, *119*, 9170 (cit. on p. 6).
- [21] Pan, H.; Feng, Y. P. *ACS nano* **2008**, *2*, 2410 (cit. on p. 6).
- [22] Wischmeier, L.; Bekeny, C.; Voss, T.; Börner, S.; Schade, W. *physica status solidi (b)* **2006**, *243*, 919 (cit. on p. 6).
- [23] Maslov, A. V.; Ning, C. Z. *Applied Physics Letters* **2003**, *83*, 1237 (cit. on pp. 6, 17, 67).
- [24] Voss, T.; Svacha, G. T.; Mazur, E.; Muller, S.; Ronning, C.; Konjhodzic, D.; Marlow, F. *Nano letters* **2007**, *7*, 3675 (cit. on pp. 6, 7, 17).
- [25] Piccione, B.; van Vugt, L. K.; Agarwal, R. *Nano letters* **2010**, *10*, 2251 (cit. on pp. 6, 17, 66).
- [26] Dayeh, S. A.; Fontcuberta i Morral, A.; Jagadish, C., *Semiconductor nanowires II: Properties and Applications*, First edition; Semiconductors and Semimetals, Vol. Volume 94; Academic Press is an imprint of Elsevier: Amsterdam et al., 2016 (cit. on p. 6).
- [27] Li, F.; Xie, X.; Gao, Q.; Tan, L.; Zhou, Y.; Yang, Q.; Ma, J.; Fu, L.; Tan, H. H.; Jagadish, C. *Nanotechnology* **2018**, *29*, 225703 (cit. on p. 6).
- [28] Jia, C.; Lin, Z.; Huang, Y.; Duan, X. *Chemical reviews* **2019**, *119*, 9074 (cit. on pp. 6–9, 41).
- [29] Ju, S.; Facchetti, A.; Xuan, Y.; Liu, J.; Ishikawa, F.; Ye, P.; Zhou, C.; Marks, T. J.; Janes, D. B. *Nature Nanotechnology* **2007**, *2*, 378 (cit. on p. 6).
- [30] Li, L.; Gu, L.; Lou, Z.; Fan, Z.; Shen, G. *ACS nano* **2017**, *11*, 4067 (cit. on p. 6).
- [31] Bao, S.; Kim, D.; Onwukaeme, C.; Gupta, S.; Saraswat, K.; Lee, K. H.; Kim, Y.; Min, D.; Jung, Y.; Qiu, H.; Wang, H.; Fitzgerald, E. A.; Tan, C. S.; Nam, D. *Nature communications* **2017**, *8*, 1845 (cit. on p. 6).
- [32] McIntyre, P. C.; Fontcuberta i Morral, A. *Materials Today Nano* **2020**, *9*, 100058 (cit. on pp. 6, 32).

- [33] Kim, K.; Lee, J. K.; Han, S. J.; Lee, S. *Applied Sciences* **2020**, *10*, 1146 (cit. on p. 6).
- [34] Gao, Q.; Saxena, D.; Wang, F.; Fu, L.; Mokkaapati, S.; Guo, Y.; Li, L.; Wong-Leung, J.; Caroff, P.; Tan, H. H.; Jagadish, C. *Nano letters* **2014**, *14*, 5206 (cit. on pp. 6, 8).
- [35] Consonni, V.; Sarigiannidou, E.; Appert, E.; Bocheux, A.; Guillemin, S.; Donatini, F.; Robin, I.-C.; Kioseoglou, J.; Robaut, F. *ACS nano* **2014**, *8*, 4761 (cit. on p. 6).
- [36] Glas, F.; Harmand, J.-C.; Patriarche, G. *Physical Review Letters* **2007**, *99*, 146101 (cit. on p. 6).
- [37] McMahon, M. I.; Nemes, R. J. *Physical Review Letters* **2005**, *95*, 215505 (cit. on pp. 6, 11).
- [38] Fadaly, E. M. T. et al. *Nature* **2020**, *580*, 205 (cit. on p. 6).
- [39] Maliakkal, C. B.; Jacobsson, D.; Tornberg, M.; Persson, A. R.; Johansson, J.; Wallenberg, R.; Dick, K. A. *Nature communications* **2019**, *10*, 4577 (cit. on pp. 6, 8).
- [40] May, B. J.; Selcu, C. M.; Sarwar, A. T. M. G.; Myers, R. C. *Applied Physics Letters* **2018**, *112*, 093107 (cit. on p. 6).
- [41] Wallentin, J.; Anttu, N.; Asoli, D.; Huffman, M.; Aberg, I.; Magnusson, M. H.; Siefer, G.; Fuss-Kailuweit, P.; Dimroth, F.; Witzigmann, B.; Xu, H. Q.; Samuelson, L.; Deppert, K.; Borgström, M. T. *Science (New York, N.Y.)* **2013**, *339*, 1057 (cit. on p. 6).
- [42] Aberg, I.; Vescovi, G.; Asoli, D.; Naseem, U.; Gilboy, J. P.; Sundvall, C.; Dahlgren, A.; Svensson, K. E.; Anttu, N.; Bjork, M. T.; Samuelson, L. *IEEE Journal of Photovoltaics* **2016**, *6*, 185 (cit. on pp. 6, 41).
- [43] Krogstrup, P.; Jørgensen, H. I.; Heiss, M.; Demichel, O.; Holm, J. V.; Aagesen, M.; Nygard, J.; Fontcuberta i Morral, A. *Nature Photonics* **2013**, *7*, 306 (cit. on pp. 6, 41).
- [44] Li, Z.; Tan, H. H.; Jagadish, C.; Fu, L. *Advanced Materials Technologies* **2018**, *3*, 1800005 (cit. on pp. 6, 8).
- [45] Zimmermann, K.; Dissinger, F.; Cammi, D.; Jaros, A.; Meierhofer, F.; Waldvogel, S. R.; Voss, T. *The Journal of Physical Chemistry C* **2018**, *122*, 29479 (cit. on p. 6).
- [46] Jain, V.; Nowzari, A.; Wallentin, J.; Borgström, M. T.; Messing, M. E.; Asoli, D.; Graczyk, M.; Witzigmann, B.; Capasso, F.; Samuelson, L.; Pettersson, H. *Nano Research* **2014**, *7*, 544 (cit. on p. 6).
- [47] Pettersson, H.; Zubritskaya, I.; Nghia, N. T.; Wallentin, J.; Borgström, M. T.; Storm, K.; Landin, L.; Wickert, P.; Capasso, F.; Samuelson, L. *Nanotechnology* **2012**, *23*, 135201 (cit. on p. 6).
- [48] Kim, M. J.; Seo, Y.; Cruz, M. A.; Wiley, B. J. *ACS nano* **2019** (cit. on p. 6).

- [49] Husanu, E.; Ercolani, D.; Gemmi, M.; Sorba, L. *Nanotechnology* **2014**, *25*, 205601 (cit. on pp. 6, 8).
- [50] Morral, A. F. i.; Dayeh, S. A.; Jagadish, C., *Semiconductor nanowires I: Growth and Theory*, First edition; Semiconductors and Semimetals, Vol. Volume 93; Academic Press is an imprint of Elsevier: Amsterdam et al., 2015 (cit. on p. 6).
- [51] Couteau, C.; Larrue, A.; Wilhelm, C.; Soci, C. *Nanophotonics* **2015**, *4* (cit. on p. 7).
- [52] Dev, A.; Elshaer, A.; Voss, T. *IEEE Journal of Selected Topics in Quantum Electronics* **2011**, *17*, 896 (cit. on p. 7).
- [53] Greil, J.; Lugstein, A.; Zeiner, C.; Strasser, G.; Bertagnolli, E. *Nano letters* **2012**, *12*, 6230 (cit. on p. 7).
- [54] Linghu, S.; Gu, Z.; Lu, J.; Fang, W.; Yang, Z.; Yu, H.; Li, Z.; Zhu, R.; Peng, J.; Zhan, Q.; Zhuang, S.; Gu, M.; Gu, F. *Nature Communications* **2021**, *12*, 385 (cit. on p. 7).
- [55] Wongkaew, N.; Simsek, M.; Griesche, C.; Baeumner, A. J. *Chemical reviews* **2019**, *119*, 120 (cit. on p. 7).
- [56] Rodriguez-Ruiz, I.; Ackermann, T. N.; Munoz-Berbel, X.; Llobera, A. *Analytical chemistry* **2016**, *88*, 6630 (cit. on p. 7).
- [57] He, J. H.; Ho, C. H.; Chen, C. Y. *Nanotechnology* **2009**, *20*, 065503 (cit. on pp. 7, 26).
- [58] Fennell, J. F.; Liu, S. F.; Azzarelli, J. M.; Weis, J. G.; Rochat, S.; Mirica, K. A.; Ravnsbæk, J. B.; Swager, T. M. *Angewandte Chemie International Edition* **2016**, *55*, 1266 (cit. on p. 7).
- [59] Gholipour, M.; Masoumi, N. *Microelectronics Journal* **2013**, *44*, 190 (cit. on p. 7).
- [60] Bi, S.; Li, Q.; Asare-Yeboah, K.; Na, J.; Sun, Y.; Jiang, C. *The journal of physical chemistry letters* **2020**, *11*, 3947 (cit. on p. 7).
- [61] Cammi, D.; Rodiek, B.; Zimmermann, K.; Kück, S.; Voss, T. *Journal of Materials Research* **2017**, *32*, 2464 (cit. on p. 7).
- [62] Chen, M.-W.; Retamal, J. R. D.; Chen, C.-Y.; He, J.-H. *IEEE Electron Device Letters* **2012**, *33*, 411 (cit. on pp. 7, 27, 75).
- [63] Soci, C.; Zhang, A.; Xiang, B.; Dayeh, S. A.; Aplin, D. P. R.; Park, J.; Bao, X. Y.; Lo, Y. H.; Wang, D. *Nano Letters* **2007**, *7*, 1003 (cit. on pp. 7, 27).
- [64] Dai, X.; Tchernycheva, M.; Soci, C. In *Semiconductor Nanowires II: Properties and Applications*, Shadi A. Dayeh, Anna Fontcuberta i Morral, Chennupati Jagadish, Ed.; Semiconductors and Semimetals, Vol. 94; Elsevier: 2016, pp 75–107 (cit. on p. 7).
- [65] Peng, K.; Parkinson, P.; Fu, L.; Gao, Q.; Jiang, N.; Guo, Y.-N.; Wang, F.; Joyce, H. J.; Boland, J. L.; Tan, H. H.; Jagadish, C.; Johnston, M. B. *Nano letters* **2015**, *15*, 206 (cit. on p. 7).

- [66] Chayanun, L.; Hrachowina, L.; Björling, A.; Borgström, M. T.; Wallentin, J. *Nano letters* **2020** (cit. on pp. 7, 43, 44).
- [67] Yang, J. C.; Mun, J.; Kwon, S. Y.; Park, S.; Bao, Z.; Park, S. *Advanced materials (Deerfield Beach, Fla.)* **2019**, *31*, e1904765 (cit. on p. 7).
- [68] Ra, Y.-H.; Wang, R.; Woo, S. Y.; Djavid, M.; Sadaf, S. M.; Lee, J.; Botton, G. A.; Mi, Z. *Nano letters* **2016**, *16*, 4608 (cit. on p. 7).
- [69] Ra, Y.-H.; Kang, S.; Lee, C.-R. *Advanced Optical Materials* **2018**, *6*, 1701391 (cit. on pp. 7, 41).
- [70] Tchernycheva, M.; Messanvi, A.; de Luna Bugallo, A.; Jacopin, G.; Lavenus, P.; Rigutti, L.; Zhang, H.; Halioua, Y.; Julien, F. H.; Eymery, J.; Durand, C. *Nano letters* **2014**, *14*, 3515 (cit. on pp. 7, 41).
- [71] Luo, M.-C.; Ren, F.-F.; Gagrani, N.; Qiu, K.; Wang, Q.; Le Yu; Ye, J.; Yan, F.; Zhang, R.; Tan, H. H.; Jagadish, C.; Ji, X. *Advanced Optical Materials* **2020**, *8*, 2000514 (cit. on p. 7).
- [72] Sirbuly, D. J.; Law, M.; Pauzauskie, P.; Yan, H.; Maslov, A. V.; Knutsen, K.; Ning, C.-Z.; Saykally, R. J.; Yang, P. *Proceedings of the National Academy of Sciences of the United States of America* **2005**, *102*, 7800 (cit. on p. 7).
- [73] Wu, X.; Chen, Q.; Xu, P.; Tong, L.; Fan, X. *Applied Physics Letters* **2017**, *111*, 031112 (cit. on p. 7).
- [74] Zapf, M.; Röder, R.; Winkler, K.; Kaden, L.; Greil, J.; Wille, M.; Grundmann, M.; Schmidt-Grund, R.; Lugstein, A.; Ronning, C. *Nano letters* **2017**, *17*, 6637 (cit. on pp. 7, 9).
- [75] Cheng, R.; Zou, C.-L.; Guo, X.; Wang, S.; Han, X.; Tang, H. X. *Nature Communications* **2019**, *10*, 4104 (cit. on p. 7).
- [76] Shang, Q.; Li, C.; Zhang, S.; Liang, Y.; Liu, Z.; Liu, X.; Zhang, Q. *Nano letters* **2020** (cit. on pp. 7, 65).
- [77] Zheng, S.; Long, Y.; Gao, D.; Luo, Y.; Wang, L.; Cao, X.; Wang, J. *ACS Photonics* **2020** (cit. on p. 7).
- [78] Piccione, B.; Cho, C.-H.; van Vugt, L. K.; Agarwal, R. *Nature nanotechnology* **2012**, *7*, 640 (cit. on pp. 7, 64).
- [79] Liborius, L.; Bieniek, J.; Nägelein, A.; Tegude, F.-J.; Prost, W.; Hannappel, T.; Poloczek, A.; Weimann, N. *physica status solidi (b)* **2020**, *257*, 1900358 (cit. on pp. 7, 98).
- [80] Saxena, D.; Mokkalapati, S.; Parkinson, P.; Jiang, N.; Gao, Q.; Tan, H. H.; Jagadish, C. *Nature Photonics* **2013**, *7*, 963 (cit. on pp. 7, 64).
- [81] Zapf, M.; Sidiropoulos, T.; Röder, R. *Advanced Optical Materials* **2019**, *7*, 1900504 (cit. on p. 7).

- [82] Röder, R.; Wille, M.; Geburt, S.; Rensberg, J.; Zhang, M.; Lu, J. G.; Capasso, F.; Buschlinger, R.; Peschel, U.; Ronning, C. *Nano letters* **2013**, *13*, 3602 (cit. on pp. 7, 70).
- [83] Zimmler, M. A.; Capasso, F.; Müller, S.; Ronning, C. *Semiconductor Science and Technology* **2010**, *25*, 024001 (cit. on pp. 7, 20, 68).
- [84] Eaton, S. W.; Fu, A.; Wong, A. B.; Ning, C.-Z.; Yang, P. *Nature Reviews Materials* **2016**, *1*, 318 (cit. on pp. 7, 61, 69).
- [85] Quan, L. N.; Kang, J.; Ning, C.-Z.; Yang, P. *Chemical reviews* **2019**, *119*, 9153 (cit. on p. 7).
- [86] Davanco, M.; Liu, J.; Sapienza, L.; Zhang, C.-Z.; de Miranda Cardoso, J. V.; Verma, V.; Mirin, R.; Nam, S. W.; Liu, L.; Srinivasan, K. *Nature communications* **2017**, *8*, 889 (cit. on p. 7).
- [87] Zhang, Y.; Saxena, D.; Aagesen, M.; Liu, H. *Nanotechnology* **2019**, *30*, 192002 (cit. on pp. 7, 8, 61).
- [88] Zimmler, M. A.; Bao, J.; Capasso, F.; Müller, S.; Ronning, C. *Applied Physics Letters* **2008**, *93*, 051101 (cit. on pp. 7, 64).
- [89] Johnson, J. C.; Yan, H.; Schaller, R. D.; Haber, L. H.; Saykally, R. J.; Yang, P. *The Journal of Physical Chemistry B* **2001**, *105*, 11387 (cit. on pp. 7, 64).
- [90] Geburt, S.; Thielmann, A.; Röder, R.; Borschel, C.; McDonnell, A.; Kozlik, M.; Kühnel, J.; Sunter, K. A.; Capasso, F.; Ronning, C. *Nanotechnology* **2012**, *23*, 365204 (cit. on pp. 8, 64).
- [91] Xiao, Y.; Meng, C.; Wu, X.; Tong, L. *Applied Physics Letters* **2011**, *99*, 023109 (cit. on p. 8).
- [92] Saxena, D.; Jiang, N.; Yuan, X.; Mokkaapati, S.; Guo, Y.; Tan, H. H.; Jagadish, C. *Nano letters* **2016**, *16*, 5080 (cit. on p. 8).
- [93] Burgess, T.; Saxena, D.; Mokkaapati, S.; Li, Z.; Hall, C. R.; Davis, J. A.; Wang, Y.; Smith, L. M.; Fu, L.; Caroff, P.; Tan, H. H.; Jagadish, C. *Nature communications* **2016**, *7*, 11927 (cit. on pp. 8, 17, 46).
- [94] Alanis, J. A.; Chen, Q.; Lysevych, M.; Burgess, T.; Li Li; Liu, Z.; Tan, H. H.; Jagadish, C.; Parkinson, P. *Nanoscale Advances* **2019**, *1*, 4393 (cit. on pp. 8, 72).
- [95] Joyce, H. J.; Docherty, C. J.; Gao, Q.; Tan, H. H.; Jagadish, C.; Lloyd-Hughes, J.; Herz, L. M.; Johnston, M. B. *Nanotechnology* **2013**, *24*, 214006 (cit. on p. 8).
- [96] Zapf, M.; Ronning, C.; Röder, R. *Applied Physics Letters* **2017**, *110*, 173103 (cit. on pp. 8–10, 61).
- [97] Jevtics, D.; McPhillimy, J.; Guilhabert, B.; Alanis, J. A.; Tan, H. H.; Jagadish, C.; Dawson, M. D.; Hurtado, A.; Parkinson, P.; Strain, M. J. *Nano letters* **2020**, *20*, 1862 (cit. on pp. 8, 41).

- [98] Zhao, Y.; You, S. S.; Zhang, A.; Lee, J.-H.; Huang, J.; Lieber, C. M. *Nature nanotechnology* **2019**, *14*, 783 (cit. on pp. 8, 41).
- [99] Zhao, X. et al. *Nano letters* **2020**, *20*, 599 (cit. on p. 8).
- [100] Gao, Q.; Li, Z.; Li Li; Vora, K.; Li, Z.; Alabadla, A.; Wang, F.; Guo, Y.; Peng, K.; Wenas, Y. C.; Mokkaapati, S.; Karouta, F.; Tan, H. H.; Jagadish, C.; Fu, L. *Progress in Photovoltaics: Research and Applications* **2019**, *27*, 237 (cit. on p. 8).
- [101] Hammarberg, S.; Dagytė, V.; Chayanun, L.; Hill, M. O.; Wyke, A.; Björling, A.; Johansson, U.; Kalbfleisch, S.; Heurlin, M.; Lauhon, L. J.; Borgström, M. T.; Wallentin, J. *Nano Research* **2020**, *13*, 2460 (cit. on p. 8).
- [102] Barrigón, E.; Hultin, O.; Lindgren, D.; Yadegari, F.; Magnusson, M. H.; Samuelson, L.; Johansson, L. I. M.; Björk, M. T. *Nano letters* **2018**, *18*, 1088 (cit. on p. 8).
- [103] Vukajlovic-Plestina, J.; Kim, W.; Ghisalberti, L.; Varnavides, G.; Tütüncüoğlu, G.; Potts, H.; Friedl, M.; Güniat, L.; Carter, W. C.; Dubrovskii, V. G.; Fontcuberta i Morral, A. *Nature Communications* **2019**, *10*, 869 (cit. on p. 8).
- [104] Aseev, P. et al. *Nano letters* **2019**, *19*, 218 (cit. on p. 8).
- [105] Friedl, M.; Cervený, K.; Huang, C.; Dede, D.; Samani, M.; Hill, M. O.; Morgan, N.; Kim, W.; Güniat, L.; Segura-Ruiz, J.; Lauhon, L. J.; Zumbühl, D. M.; Fontcuberta i Morral, A. *Nano letters* **2020** (cit. on p. 8).
- [106] Hwang, S.-W. et al. *Science (New York, N.Y.)* **2012**, *337*, 1640 (cit. on p. 9).
- [107] Pimenta, A. C. S.; Limborço, H.; González, J. C.; Cifuentes, N.; Ramos, S. L. L. M.; Matinaga, F. M. *RSC Advances* **2019**, *9*, 39488 (cit. on pp. 9, 50, 58).
- [108] McKibbin, S. R.; Colvin, J.; Troian, A.; Knutsson, J. V.; Webb, J. L.; Otnes, G.; Dirscherl, K.; Sezen, H.; Amati, M.; Gregoratti, L.; Borgström, M. T.; Mikkelsen, A.; Timm, R. *Nano letters* **2020** (cit. on p. 9).
- [109] Milano, G.; Luebben, M.; Laurenti, M.; Porro, S.; Bejtka, K.; Bianco, S.; Breuer, U.; Boarino, L.; Valov, I.; Ricciardi, C. *Advanced Materials Interfaces* **2019**, *6*, 1900803 (cit. on pp. 9, 26, 86).
- [110] Lee, J.; Lee, W.; Lim, J.; Yu, Y.; Kong, Q.; Urban, J. J.; Yang, P. *Nano letters* **2016**, *16*, 4133 (cit. on pp. 9, 57).
- [111] Walia, J.; Dhindsa, N.; Flannery, J.; Khodabad, I.; Forrest, J.; LaPierre, R.; Saini, S. S. *Nano letters* **2014**, *14*, 5820 (cit. on pp. 9, 57).
- [112] Zou, X.; Chen, X.; Huang, H.; Xu, Y.; Duan, W. *Nanoscale* **2015**, *7*, 8776 (cit. on p. 9).
- [113] Alanis, J. A.; Saxena, D.; Mokkaapati, S.; Jiang, N.; Peng, K.; Tang, X.; Fu, L.; Tan, H. H.; Jagadish, C.; Parkinson, P. *Nano letters* **2017**, *17*, 4860 (cit. on p. 9).

- [114] Martin, P. N.; Aksamija, Z.; Pop, E.; Ravaioli, U. *Nano letters* **2010**, *10*, 1120 (cit. on pp. 9, 57, 59).
- [115] Li, D.; Wu, Y.; Kim, P.; Shi, L.; Yang, P.; Majumdar, A. *Applied Physics Letters* **2003**, *83*, 2934 (cit. on pp. 9, 57).
- [116] Zapf, M.; Ritzer, M.; Liborius, L.; Johannes, A.; Hafermann, M.; Schönherr, S.; Segura-Ruiz, J.; Martínez-Criado, G.; Prost, W.; Ronning, C. *Nature Communications* **2020**, *11*, 4729 (cit. on pp. 10, 41).
- [117] Theeß, G. Elektronenstrahlinduzierte Modifikation von Halbleiternanodrähten, Examination thesis, Jena: Friedrich-Schiller-Universität Jena, 2019 (cit. on pp. 10, 61).
- [118] Nicklaus, J. Elektronenstrahl-induzierte Modifikation von Halbleiternanodrähten, Bachelor thesis, Jena: Friedrich-Schiller-Universität Jena, 2020 (cit. on pp. 10, 61).
- [119] Husko, C.; de Rossi, A.; Combrié, S.; Tran, Q. V.; Raineri, F.; Wong, C. W. *Applied Physics Letters* **2009**, *94*, 021111 (cit. on p. 11).
- [120] Ahn, M.-W.; Park, K.-S.; Heo, J.-H.; Park, J.-G.; Kim, D.-W.; Choi, K. J.; Lee, J.-H.; Hong, S.-H. *Applied Physics Letters* **2008**, *93*, 263103 (cit. on p. 11).
- [121] Subannajui, K.; Wongchoosuk, C.; Ramgir, N.; Wang, C.; Yang, Y.; Hartel, A.; Cimalla, V.; Zacharias, M. *Journal of Applied Physics* **2012**, *112*, 034311 (cit. on p. 11).
- [122] Adachi, S. *Journal of Applied Physics* **1985**, *58*, R1 (cit. on p. 11).
- [123] Blakemore, J. S. *Journal of Applied Physics* **1982**, *53*, R123 (cit. on pp. 11, 45, 57).
- [124] Senichev, A.; Corfdir, P.; Brandt, O.; Ramsteiner, M.; Breuer, S.; Schilling, J.; Geelhaar, L.; Werner, P. *Nano Research* **2018**, *11*, 4708 (cit. on p. 11).
- [125] De Luca, M.; Rubini, S.; Felici, M.; Meaney, A.; Christianen, P. C. M.; Martelli, F.; Polimeni, A. *Nano letters* **2017**, *17*, 6540 (cit. on p. 11).
- [126] Chen, H.-L.; Cattoni, A.; de Lépinau, R.; Walker, A. W.; Höhn, O.; Lackner, D.; Siefer, G.; Faustini, M.; Vandamme, N.; Goffard, J.; Behaghel, B.; Dupuis, C.; Bardou, N.; Dimroth, F.; Collin, S. *Nature Energy* **2019**, *4*, 761 (cit. on p. 12).
- [127] Kim, O. K.; Spitzer, W. G. *Journal of Applied Physics* **1979**, *50*, 4362 (cit. on p. 12).
- [128] Devreese, J. T.; Peeters, F., *Polarons and Excitons in Polar Semiconductors and Ionic Crystals*; NATO ASI Series, Series B, Vol. 127; Springer: Boston, MA, 1984 (cit. on p. 12).
- [129] Bernardi, M.; Vigil-Fowler, D.; Ong, C. S.; Neaton, J. B.; Louie, S. G. *Proceedings of the National Academy of Sciences of the United States of America* **2015**, *112*, 5291 (cit. on pp. 12, 57, 58).
- [130] Moore, W. J.; Holm, R. T. *Journal of Applied Physics* **1996**, *80*, 6939 (cit. on p. 12).

- [131] Nam, S. B.; Reynolds, D. C.; Litton, C. W.; Almassy, R. J.; Collins, T. C.; Wolfe, C. M. *Physical Review B* **1976**, *13*, 761 (cit. on p. 12).
- [132] Sell, D. D. *Physical Review B* **1972**, *6*, 3750 (cit. on p. 12).
- [133] *Landolt-Börnstein. Numerical data and functional relationships in science and technology. New Series. Group III: Crystal and Solid State Physics. Vol. 22: Semiconductors.* Paufler, P., Ed.; Springer-Verlag: Berlin, 1988; Vol. 23 (cit. on p. 12).
- [134] European Parliament and the Council Regulation (EC) No 1223/2009 on cosmetic products, 2009 (cit. on p. 12).
- [135] Li, Z.; Yang, R.; Yu, M.; Bai, F.; Li, C.; Wang, Z. L. *The Journal of Physical Chemistry C* **2008**, *112*, 20114 (cit. on p. 12).
- [136] Wang, Z. L. *Journal of Physics: Condensed Matter* **2004**, *16*, R829 (cit. on pp. 12, 32).
- [137] Ivanov, I.; Pollmann, J. *Physical review. B, Condensed matter* **1981**, *24*, 7275 (cit. on p. 12).
- [138] Phillips, J. C. *Reviews of Modern Physics* **1970**, *42*, 317 (cit. on p. 12).
- [139] Özgür, Ü.; Alivov, Y. I.; Liu, C.; Teke, A.; Reshchikov, M. A.; Doğan, S.; Avrutin, V.; Cho, S.-J.; Morkoç, H. *Journal of Applied Physics* **2005**, *98*, 041301 (cit. on p. 12).
- [140] Meyer, B. K.; Alves, H.; Hofmann, D. M.; Kriegseis, W.; Forster, D.; Bertram, F.; Christen, J.; Hoffmann, A.; Straßburg, M.; Dworzak, M.; Haboek, U.; Rodina, A. V. *physica status solidi (b)* **2004**, *241*, 231 (cit. on pp. 12, 30).
- [141] Yoshikawa, H.; Adachi, S. *Japanese Journal of Applied Physics* **1997**, *36*, 6237 (cit. on pp. 12, 17).
- [142] Xu, S. J.; Xiong, S.-J.; Shi, S. L. *The Journal of Chemical Physics* **2005**, *123*, 221105 (cit. on p. 12).
- [143] Thomas, D. G.; Hopfield, J. J. *Journal of Applied Physics* **1962**, *33*, 3243 (cit. on pp. 13, 14).
- [144] Hotje, U.; Rose, C.; Binnewies, M. *Solid State Sciences* **2003**, *5*, 1259 (cit. on p. 13).
- [145] *Bonds and bands in semiconductors*; Phillips, J. C., Ed.; Materials science and technology; Academic Press: New York, NY, 1973 (cit. on p. 13).
- [146] Thomas, D. G.; Hopfield, J. J. *Physical Review* **1962**, *128*, 2135 (cit. on p. 13).
- [147] Bieniewski, T. M.; Czyzak, S. J. *Journal of the Optical Society of America* **1963**, *53*, 496 (cit. on p. 13).
- [148] Kanaya, K.; Okayama, S. *Journal of Physics D: Applied Physics* **1972**, *5*, 43 (cit. on p. 13).
- [149] Drouin, D.; Couture, A. R.; Joly, D.; Tastet, X.; Aimez, V.; Gauvin, R. *Scanning* **2007**, *29*, 92 (cit. on pp. 13, 78).

- [150] Alig, R. C.; Bloom, S. *Journal of Applied Physics* **1978**, *49*, 3476 (cit. on pp. 13, 45).
- [151] Kanaya, K.; Kawakatsu, H. *Journal of Physics D: Applied Physics* **1972**, *5*, 1727 (cit. on p. 13).
- [152] Yu, P. Y.; Cardona, M., *Fundamentals of Semiconductors: Physics and Materials Properties*, 4. ed.; Graduate Texts in Physics; Springer-Verlag Berlin Heidelberg: Berlin, Heidelberg, 2010 (cit. on p. 14).
- [153] Koida, T.; Chichibu, S. F.; Uedono, A.; Tsukazaki, A.; Kawasaki, M.; Sota, T.; Segawa, Y.; Koinuma, H. *Applied Physics Letters* **2003**, *82*, 532 (cit. on pp. 14, 29, 85).
- [154] Reynolds, D. C.; Look, D. C.; Jogai, B.; Hoelscher, J. E.; Sherriff, R. E.; Harris, M. T.; Callahan, M. J. *Journal of Applied Physics* **2000**, *88*, 2152 (cit. on p. 14).
- [155] Heitz; Hoffmann; Broser *Physical review. B, Condensed matter* **1994**, *49*, 14307 (cit. on p. 14).
- [156] Dietz, R. E.; Hopfield, J. J.; Thomas, D. G. *Journal of Applied Physics* **1961**, *32*, 2282 (cit. on p. 14).
- [157] Titova, L. V.; Hoang, T. B.; Jackson, H. E.; Smith, L. M.; Yarrison-Rice, J. M.; Lensch, J. L.; Lauhon, L. J. *Applied Physics Letters* **2006**, *89*, 053119 (cit. on p. 14).
- [158] Klingshirn, C., *Semiconductor Optics // Semiconductor optics: With 20 tables*, 3. ed.; Springer: Berlin, Heidelberg, 2007 (cit. on pp. 14–16).
- [159] Grundmann, M., *Physics of Semiconductors: An introduction including nanophysics and applications*; SPRINGER NATURE: [S.l.], 2020 (cit. on pp. 14, 15).
- [160] Ueta, M.; Kanzaki, H.; Kobayashi, K., *Excitonic processes in solids*; Springer Series in Solid-State Sciences, Vol. 60; Springer: Berlin, 1986 (cit. on p. 15).
- [161] Magde, D.; Mahr, H. *Physical Review Letters* **1970**, *24*, 890 (cit. on p. 15).
- [162] Klingshirn, C.; Fallert, J.; Zhou, H.; Sartor, J.; Thiele, C.; Maier-Flaig, F.; Schneider, D.; Kalt, H. *physica status solidi (b)* **2010**, *247*, 1424 (cit. on p. 15).
- [163] Bohnert, K.; Schmieder, G.; El-Dessouki, S.; Klingshirn, C. *Solid State Communications* **1978**, *27*, 295 (cit. on pp. 15, 19).
- [164] Ton-That, C.; Weston, L.; Phillips, M. R. *Physical Review B* **2012**, *86*, 115205 (cit. on pp. 16, 28, 29, 78, 85).
- [165] Villafuerte, J.; Donatini, F.; Kioseoglou, J.; Sarigiannidou, E.; Chaix-Pluchery, O.; Pernot, J.; Consonni, V. *The Journal of Physical Chemistry C* **2020**, *124*, 16652 (cit. on pp. 16, 28, 29, 78, 85).

- [166] Vidya, R.; Ravindran, P.; Fjellvåg, H.; Svensson, B. G.; Monakhov, E.; Ganchenkova, M.; Nieminen, R. M. *Physical Review B* **2011**, *83* (cit. on pp. 16, 28, 30).
- [167] Choi, S.; Phillips, M. R.; Aharonovich, I.; Pornsuwan, S.; Cowie, B. C. C.; Ton-That, C. *Advanced Optical Materials* **2015**, *3*, 821 (cit. on pp. 16, 28–30).
- [168] Djurišić, A. B.; Leung, Y. H.; Tam, K. H.; Hsu, Y. F.; Ding, L.; Ge, W. K.; Zhong, Y. C.; Wong, K. S.; Chan, W. K.; Tam, H. L.; Cheah, K. W.; Kwok, W. M.; Phillips, D. L. *Nanotechnology* **2007**, *18*, 095702 (cit. on pp. 16, 28, 66).
- [169] Zhang, M.; Averseng, F.; Haque, F.; Borghetti, P.; Krafft, J.-M.; Baptiste, B.; Costentin, G.; Stankic, S. *Nanoscale* **2019**, *11*, 5102 (cit. on pp. 16, 28).
- [170] Spindler, C.; Galvani, T.; Wirtz, L.; Rey, G.; Siebentritt, S. *Journal of Applied Physics* **2019**, *126*, 175703 (cit. on p. 16).
- [171] Schmidt; Lischka; Zulehner *Physical review. B, Condensed matter* **1992**, *45*, 8989 (cit. on p. 16).
- [172] Cooper, D. E.; Bajaj, J.; Newman, P. R. *Journal of Crystal Growth* **1988**, *86*, 544 (cit. on p. 16).
- [173] Cui, J. B.; Thomas, M. A. *Journal of Applied Physics* **2009**, *106*, 033518 (cit. on pp. 16, 29).
- [174] Hou, D.; Voss, T.; Ronning, C.; Menzel, A.; Zacharias, M. *Journal of Applied Physics* **2014**, *115*, 233516 (cit. on pp. 16, 17, 64, 82).
- [175] Reshchikov, M. A.; Morkoç, H.; Nemeth, B.; Nause, J.; Xie, J.; Hertog, B.; Osinsky, A. *Physica B: Condensed Matter* **2007**, *401-402*, 358 (cit. on p. 16).
- [176] Grieshaber, W.; Schubert, E. F.; Goepfert, I. D.; Karlicek, R. F.; Schurman, M. J.; Tran, C. *Journal of Applied Physics* **1996**, *80*, 4615 (cit. on p. 16).
- [177] van Dijken, A.; Meulenkaamp, E. A.; Vanmaekelbergh, D.; Meijerink, A. *The Journal of Physical Chemistry B* **2000**, *104*, 1715 (cit. on pp. 16, 30, 83).
- [178] Pankove, J. I., *Optical Processes in Semiconductors*; Dover Books on Physics; Dover Publications: Newburyport, 2012 (cit. on p. 16).
- [179] Stoneham, A. M. *Reports on Progress in Physics* **1981**, *44*, 1251 (cit. on p. 16).
- [180] Malitson, I. H. *Journal of the Optical Society of America* **1965**, *55*, 1205 (cit. on p. 17).
- [181] Al-Azzawi, A., *Fibre optics: Principles and practices*; CRC Press: Boca Raton u.a., 2007 (cit. on p. 17).
- [182] Barrelet, C. J.; Greytak, A. B.; Lieber, C. M. *Nano Letters* **2004**, *4*, 1981 (cit. on p. 17).
- [183] Rai, R. C. *Journal of Applied Physics* **2013**, *113*, 153508 (cit. on pp. 18, 64, 66).

- [184] Liu, X.; Zhang, Q.; Xiong, Q.; Sum, T. C. *Nano letters* **2013**, *13*, 1080 (cit. on pp. 18, 65).
- [185] Urbach, F. *Physical Review* **1953**, *92*, 1324 (cit. on p. 18).
- [186] Martienssen, W. *Journal of Physics and Chemistry of Solids* **1959**, *8*, 294 (cit. on p. 18).
- [187] Aghamalyan, N. R.; Gambaryan, I. A.; Goulanian, E. K.; Hovsepyan, R. K.; Kostanyan, R. B.; Petrosyan, S. I.; Vardanyan, E. S.; Zerrouk, A. F. *Semiconductor Science and Technology* **2003**, *18*, 525 (cit. on pp. 18, 66).
- [188] Schönau, S.; Ruske, F.; Neubert, S.; Rech, B. *Applied Physics Letters* **2013**, *103*, 192108 (cit. on pp. 18, 66).
- [189] Pan, A.; Liu, D.; Liu, R.; Wang, F.; Zhu, X.; Zou, B. *Small* **2005**, *1*, 980 (cit. on p. 18).
- [190] Li, J.; Meng, C.; Liu, Y.; Wu, X.; Lu, Y.; Ye, Y.; Dai, L.; Tong, L.; Liu, X.; Yang, Q. *Advanced Materials* **2013**, *25*, 833 (cit. on p. 18).
- [191] Huang, R.; Yamamoto, Y.; André, R.; Bleuse, J.; Muller, M.; Ulmer-Tuffigo, H. *Physical Review B* **2002**, *65*, 165314 (cit. on p. 18).
- [192] Newbury, P. R.; Shahzad, K.; Cammack, D. A. *Applied Physics Letters* **1991**, *58*, 1065 (cit. on p. 18).
- [193] Bagnall, D. M.; Chen, Y. F.; Zhu, Z.; Yao, T.; Shen, M. Y.; Goto, T. *Applied Physics Letters* **1998**, *73*, 1038 (cit. on p. 18).
- [194] Koch, S. W.; Haug, H.; Schmieder, G.; Bohnert, W.; Klingshirn, C. *physica status solidi (b)* **1978**, *89*, 431 (cit. on p. 18).
- [195] Michalsky, T.; Wille, M.; Dietrich, C. P.; Röder, R.; Ronning, C.; Schmidt-Grund, R.; Grundmann, M. *Applied Physics Letters* **2014**, *105*, 211106 (cit. on p. 18).
- [196] Bohnert, K.; Schmieder, G.; Klingshirn, C. *physica status solidi (b)* **1980**, *98*, 175 (cit. on p. 19).
- [197] Othonos, A. *Journal of Applied Physics* **1998**, *83*, 1789 (cit. on p. 19).
- [198] Landsberg *Proceedings of the Physical Society. Section A* **1949**, *62*, 806 (cit. on p. 19).
- [199] Siegman, A. E., *Lasers*; Univ. Science Books: Mill Valley, Calif., 1986 (cit. on p. 20).
- [200] Maslov, A. V.; Ning, C. Z. *IEEE Journal of Quantum Electronics* **2004**, *40*, 1389 (cit. on p. 20).
- [201] Casperson *Journal of Applied Physics* **1975**, 5194 (cit. on pp. 21, 67, 69, 87).
- [202] Lambert, J. H., I. H. *Lambert Academiae Scientiarum Electoralis Boicae, Et Societatis Physico-Medicae Basiliensis Membri ... Photometria Sive De Mensura Et Gradibus Luminis, Colorum Et Umbrae*; Klett and Detleffsen: Augustae Vindelicorum and Augustae Vindelicorum, 1760 (cit. on p. 21).

- [203] Beer *Annalen der Physik und Chemie* **1852**, 162, 78 (cit. on p. 21).
- [204] Henke, B. L.; Gullikson, E. M.; Davis, J. C. *Atomic Data and Nuclear Data Tables* **1993**, 54, 181 (cit. on p. 22).
- [205] Thompson, A.; Attwood, D.; Gullikson, E.; Howells, M.; Kim, K.-J.; Kirz, J.; Kortright, J.; Lindau, I.; Liu, Y.; Pianetta, P.; Robinson, A.; Scofield, J.; Underwood, J.; Williams, G.; Winick, H., *X-ray data booklet*; Lawrence Berkeley National Laboratory: 2009 (cit. on p. 22).
- [206] Lifshin, E., *X-ray characterization of materials*; Wiley-VCH: Weinheim and New York, 1999 (cit. on pp. 22, 50).
- [207] Newville, M. *Reviews in Mineralogy and Geochemistry* **2014**, 78, 33 (cit. on pp. 22, 23).
- [208] Calvin, S., *XAFS for Everyone*; CRC Press: Hoboken, 2013 (cit. on pp. 23, 39).
- [209] Mino, L.; Agostini, G.; Borfecchia, E.; Gianolio, D.; Piovano, A.; Gallo, E.; Lamberti, C. *Journal of Physics D: Applied Physics* **2013**, 46, 423001 (cit. on p. 23).
- [210] Bordiga, S.; Groppo, E.; Agostini, G.; van Bokhoven, J. A.; Lamberti, C. *Chemical reviews* **2013**, 113, 1736 (cit. on p. 23).
- [211] Getsoian, A. “; Das, U.; Camacho-Bunquin, J.; Zhang, G.; Gallagher, J. R.; Hu, B.; Cheah, S.; Schaidle, J. A.; Ruddy, D. A.; Hensley, J. E.; Krause, T. R.; Curtiss, L. A.; Miller, J. T.; Hock, A. S. *Catalysis Science & Technology* **2016**, 6, 6339 (cit. on pp. 23, 50).
- [212] Revenant, C.; Benwadih, M.; Proux, O. *physica status solidi (RRL) - Rapid Research Letters* **2015**, 9, 652 (cit. on pp. 23, 50).
- [213] Behrens, P. *TrAC Trends in Analytical Chemistry* **1992**, 11, 237 (cit. on pp. 23, 50, 54).
- [214] Mino, L.; Borfecchia, E.; Segura-Ruiz, J.; Giannini, C.; Martinez-Criado, G.; Lamberti, C. *Reviews of Modern Physics* **2018**, 90 (cit. on p. 23).
- [215] Chayanun, L.; Dagytė, V.; Troian, A.; Salomon, D.; Borgström, M.; Wallentin, J. *Nanotechnology* **2018**, 29, 454001 (cit. on p. 23).
- [216] Stuckelberger, M.; West, B.; Nietzold, T.; Lai, B.; Maser, J. M.; Rose, V.; Bertoni, M. I. *Journal of Materials Research* **2017**, 32, 1825 (cit. on p. 23).
- [217] Chayanun, L.; Otnes, G.; Troian, A.; Hammarberg, S.; Salomon, D.; Borgström, M. T.; Wallentin, J. *Journal of synchrotron radiation* **2019**, 26, 102 (cit. on pp. 23, 43, 45).
- [218] Ibach, H.; Lüth, H., *Solid-state physics: An introduction to principles of materials science*, 4., extensively updated and enl. ed.; Physics and astronomy online library; Springer: Dordrecht, 2009 (cit. on p. 24).
- [219] Hodes, G.; Kamat, P. V. *The journal of physical chemistry letters* **2015**, 6, 4090 (cit. on p. 24).

- [220] Dan, Y.; Seo, K.; Takei, K.; Meza, J. H.; Javey, A.; Crozier, K. B. *Nano letters* **2011**, *11*, 2527 (cit. on p. 25).
- [221] Zhang, Z.; Yates, J. T. *Chemical reviews* **2012**, *112*, 5520 (cit. on pp. 25, 26).
- [222] Chen, C.-Y.; Retamal, J. R. D.; Wu, I.-W.; Lien, D.-H.; Chen, M.-W.; Ding, Y.; Chueh, Y.-L.; Wu, C.-I.; He, J.-H. *ACS nano* **2012**, *6*, 9366 (cit. on p. 26).
- [223] Yang, L. L.; Zhao, Q. X.; Israr, M. Q.; Sadaf, J. R.; Willander, M.; Pozina, G.; Yang, J. H. *Journal of Applied Physics* **2010**, *108*, 103513 (cit. on p. 26).
- [224] Calarco, R.; Marso, M.; Richter, T.; Aykanat, A. I.; Meijers, R.; V D Hart, A.; Stoica, T.; Lüth, H. *Nano Letters* **2005**, *5*, 981 (cit. on p. 26).
- [225] Hong, W.-K.; Jo, G.; Kwon, S.-S.; Song, S.; Lee, T. *IEEE Transactions on Electron Devices* **2008**, *55*, 3020 (cit. on p. 26).
- [226] Bridoux, G.; Ruano, G. D.; Ferreyra, J. M.; Villafuerte, M. *Journal of Applied Physics* **2020**, *127*, 245704 (cit. on p. 26).
- [227] Chen, M.-W.; Chen, C.-Y.; Lien, D.-H.; Ding, Y.; He, J.-H. *Optics Express* **2010**, *18*, 14836 (cit. on p. 26).
- [228] Vempati, S.; Ozcan, S.; Uyar, T. *Applied Surface Science* **2018**, *457*, 676 (cit. on p. 26).
- [229] Fan, S.-W.; Srivastava, A. K.; Dravid, V. P. *Applied Physics Letters* **2009**, *95*, 142106 (cit. on pp. 26, 27).
- [230] Takata, M.; Tsubone, D.; Yanagida, H. *Journal of the American Ceramic Society* **1976**, *59*, 4 (cit. on p. 26).
- [231] Choopun, S.; Hongstith, N.; Mangkorntong, P.; Mangkorntong, N. *Physica E: Low-dimensional Systems and Nanostructures* **2007**, *39*, 53 (cit. on p. 26).
- [232] Liu, W. Z.; Xu, H. Y.; Ma, J. G.; Liu, C. Y.; Liu, Y. X.; Liu, Y. C. *Applied Physics Letters* **2012**, *100*, 203101 (cit. on pp. 26, 86, 98).
- [233] Liu, J.; Gao, F.; Wu, L.; Zhang, H.; Hong, W.; Jin, G.; Zhai, Z.; Fu, C. *Applied Physics A* **2020**, *126* (cit. on p. 26).
- [234] Xu, H.; Fan, W.; Rosa, A. L.; Zhang, R. Q.; Frauenheim, T. *Physical Review B* **2009**, *79* (cit. on p. 26).
- [235] Kim, W.; Choi, M.; Yong, K. *Sensors and Actuators B: Chemical* **2015**, *209*, 989 (cit. on pp. 26, 30).
- [236] Pati, S.; Majumder, S. B.; Banerji, P. *Journal of Alloys and Compounds* **2012**, *541*, 376 (cit. on p. 26).
- [237] Melnick, D. A. *The Journal of Chemical Physics* **1957**, *26*, 1136 (cit. on p. 27).

- [238] Vieira, D. H.; Da Silva Ozório, M.; Nogueira, G. L.; Fugikawa-Santos, L.; Alves, N. *Materials Science in Semiconductor Processing* **2021**, *121*, 105339 (cit. on pp. 27, 91).
- [239] Özdoğan, M.; Çelebi, C.; Utlü, G. *Materials Science in Semiconductor Processing* **2020**, *107*, 104863 (cit. on p. 27).
- [240] Wilken, S.; Parisi, J.; Borchert, H. *The Journal of Physical Chemistry C* **2014**, *118*, 19672 (cit. on pp. 27, 91).
- [241] Khan, F.; Ajmal, H. M. S.; Nam, K.; Kim, S.-D. *Optics Express* **2020**, *28*, 27688 (cit. on pp. 27, 91).
- [242] Prades, J. D.; Hernandez-Ramirez, F.; Jimenez-Diaz, R.; Manzanares, M.; Andreu, T.; Cirera, A.; Romano-Rodriguez, A.; Morante, J. R. *Nanotechnology* **2008**, *19*, 465501 (cit. on p. 27).
- [243] Kushwaha, A.; Aslam, M. *Journal of Applied Physics* **2012**, *112*, 054316 (cit. on p. 27).
- [244] Röhr, J. A.; Sá, J.; Konezny, S. J. *Communications Chemistry* **2019**, *2*, 1 (cit. on pp. 27, 75, 84).
- [245] Ma, Y.; Choi, T.-W.; Cheung, S. H.; Cheng, Y.; Xu, X.; Xie, Y.-M.; Li, H.-W.; Li, M.; Luo, H.; Zhang, W.; So, S. K.; Chen, S.; Tsang, S.-W. *Nanoscale* **2019**, *11*, 8736 (cit. on pp. 27, 84).
- [246] Zhang, Z.; Yates, J. T. *The Journal of Physical Chemistry C* **2010**, *114*, 3098 (cit. on p. 27).
- [247] Cammi, D.; Zimmermann, K.; Gorny, R.; Vogt, A.; Dissinger, F.; Gad, A.; Markiewicz, N.; Waag, A.; Prades, J. D.; Ronning, C.; Waldvogel, S. R.; Voss, T. *The Journal of Physical Chemistry C* **2018**, *122*, 1852 (cit. on p. 27).
- [248] Perdew, J. P. *International Journal of Quantum Chemistry* **1985**, *28*, 497 (cit. on p. 28).
- [249] Janotti, A.; van de Walle, C. G. *Reports on Progress in Physics* **2009**, *72*, 126501 (cit. on pp. 28, 30).
- [250] McCluskey, M. D.; Jokela, S. J. *Journal of Applied Physics* **2009**, *106*, 071101 (cit. on p. 28).
- [251] Brillson, L.; Cox, J.; Gao, H.; Foster, G.; Ruane, W.; Jarjour, A.; Allen, M.; Look, D.; von Wenckstern, H.; Grundmann, M. *Materials* **2019**, *12* (cit. on pp. 28, 66, 99).
- [252] Vanheusden, K.; Seager, C. H.; Warren, W. L.; Tallant, D. R.; Voigt, J. A. *Applied Physics Letters* **1996**, *68*, 403 (cit. on pp. 28, 30).
- [253] Wang, R.-C.; Cheng, C.-F. *Plasma Processes and Polymers* **2015**, *12*, 51 (cit. on pp. 28, 78).
- [254] Alvi, N. H.; Ul Hasan, K.; Nur, O.; Willander, M. *Nanoscale Research Letters* **2011**, *6*, 130 (cit. on pp. 28, 29).

- [255] Wu, X. L.; Siu, G. G.; Fu, C. L.; Ong, H. C. *Applied Physics Letters* **2001**, *78*, 2285 (cit. on p. 28).
- [256] Camarda, P.; Messina, F.; Vaccaro, L.; Agnello, S.; Buscarino, G.; Schneider, R.; Popescu, R.; Gerthsen, D.; Lorenzi, R.; Gelardi, F. M.; Cannas, M. *Physical chemistry chemical physics : PCCP* **2016**, *18*, 16237 (cit. on p. 28).
- [257] Čížek, J.; Valenta, J.; Hruška, P.; Melikhova, O.; Procházka, I.; Novotný, M.; Bulíř, J. *Applied Physics Letters* **2015**, *106*, 251902 (cit. on p. 28).
- [258] Cabral, L.; Lopez-Richard, V.; Da Silva, J. L.; Marques, G. E.; Lima, M. P.; Onofre, Y. J.; Teodoro, M. D.; de Godoy, M. *Journal of Luminescence* **2020**, *227*, 117536 (cit. on p. 28).
- [259] Kennedy, O. W.; White, E. R.; Howkins, A.; Williams, C. K.; Boyd, I. W.; Warburton, P. A.; Shaffer, M. S. P. *The Journal of Physical Chemistry Letters* **2019**, *10*, 386 (cit. on p. 28).
- [260] Ruane, W. T.; Johansen, K. M.; Leedy, K. D.; Look, D. C.; von Wenckstern, H.; Grundmann, M.; Farlow, G. C.; Brillson, L. J. *Nanoscale* **2016**, *8*, 7631 (cit. on pp. 28, 29).
- [261] Zhang, Y.; Ozu, S.; Wu, G.; Ding, C.; Liu, F.; Liu, D.; Minemoto, T.; Masuda, T.; Hayase, S.; Toyoda, T.; Shen, Q. *The Journal of Physical Chemistry C* **2020**, *124*, 15812 (cit. on pp. 28, 66, 98).
- [262] Liu, M.; Nam, C.-Y.; Black, C. T.; Kamcev, J.; Zhang, L. *The Journal of Physical Chemistry C* **2013**, *117*, 13396 (cit. on pp. 28, 98).
- [263] Djurišić, A. B.; Choy, W. C. H.; Roy, V. A. L.; Leung, Y. H.; Kwong, C. Y.; Cheah, K. W.; Gundu Rao, T. K.; Chan, W. K.; Fei Lui, H.; Surya, C. *Advanced Functional Materials* **2004**, *14*, 856 (cit. on p. 28).
- [264] Wardle, M. G.; Goss, J. P.; Briddon, P. R. *Applied Physics Letters* **2006**, *88*, 261906 (cit. on pp. 28, 29).
- [265] Ip, K.; Overberg, M. E.; Heo, Y. W.; Norton, D. P.; Pearton, S. J.; Kucheyev, S. O.; Jagadish, C.; Williams, J. S.; Wilson, R. G.; Zavada, J. M. *Applied Physics Letters* **2002**, *81*, 3996 (cit. on p. 29).
- [266] Lyons, J. L.; Varley, J. B.; Steiauf, D.; Janotti, A.; van de Walle, C. G. *Journal of Applied Physics* **2017**, *122*, 035704 (cit. on pp. 29, 30).
- [267] Koßmann, J.; Hättig, C. *Physical chemistry chemical physics : PCCP* **2012**, *14*, 16392 (cit. on pp. 29, 30).
- [268] Wardle, M. G.; Goss, J. P.; Briddon, P. R. *Physical Review B* **2005**, *72* (cit. on pp. 29, 30, 93).
- [269] Park, Y. R.; Kim, J.; Kim, Y. S. *Applied Surface Science* **2009**, *255*, 9010 (cit. on p. 29).
- [270] van de Walle, C. G. *Physical review letters* **2000**, *85*, 1012 (cit. on pp. 29, 78).

- [271] Qiu, H.; Meyer, B.; Wang, Y.; Wöll, C. *Physical Review Letters* **2008**, *101*, 236401 (cit. on p. 29).
- [272] Beh, H.; Hiller, D.; Bruns, M.; Welle, A.; Becker, H.-W.; Berghoff, B.; Sürgers, C.; Merz, R.; Zacharias, M. *Journal of Applied Physics* **2017**, *122*, 025306 (cit. on p. 29).
- [273] Beh, H.; Hiller, D.; Laube, J.; Gutsch, S.; Zacharias, M. *Journal of Vacuum Science & Technology A: Vacuum, Surfaces, and Films* **2017**, *35*, 01B127 (cit. on p. 29).
- [274] Bang, J.; Chang, K. J. *Applied Physics Letters* **2008**, *92*, 132109 (cit. on p. 29).
- [275] Ip, K.; Overberg, M. E.; Heo, Y. W.; Norton, D. P.; Pearton, S. J.; Stutz, C. E.; Luo, B.; Ren, F.; Look, D. C.; Zavada, J. M. *Applied Physics Letters* **2003**, *82*, 385 (cit. on p. 29).
- [276] Doh, W. H.; Roy, P. C.; Kim, C. M. *Langmuir : the ACS journal of surfaces and colloids* **2010**, *26*, 16278 (cit. on p. 29).
- [277] Strzhemechny, Y. M.; Nemergut, J.; Smith, P. E.; Bae, J.; Look, D. C.; Brillson, L. J. *Journal of Applied Physics* **2003**, *94*, 4256 (cit. on p. 29).
- [278] Dev, A.; Niepelt, R.; Richters, J. P.; Ronning, C.; Voss, T. *Nanotechnology* **2010**, *21*, 065709 (cit. on pp. 29, 78, 98).
- [279] Ohashi, N.; Wang, Y.-G.; Ishigaki, T.; Wada, Y.; Taguchi, H.; Sakaguchi, I.; Ohgaki, T.; Adachi, Y.; Haneda, H. *Journal of Crystal Growth* **2007**, *306*, 316 (cit. on pp. 29, 91).
- [280] Karazhanov, S. Z.; Marstein, E. S.; Holt, A. *Journal of Applied Physics* **2009**, *105*, 033712 (cit. on pp. 29, 30).
- [281] Cossuet, T.; Donatini, F.; Lord, A. M.; Appert, E.; Pernot, J.; Consonni, V. *The Journal of Physical Chemistry C* **2018**, *122*, 22767 (cit. on pp. 29, 30, 78, 85).
- [282] Ahn, C. H.; Kim, Y. Y.; Kim, D. C.; Mohanta, S. K.; Cho, H. K. *Journal of Applied Physics* **2009**, *105*, 013502 (cit. on p. 29).
- [283] Kohan, A. F.; Ceder, G.; Morgan, D.; van de Walle, C. G. *Physical review. B, Condensed matter* **2000**, *61*, 15019 (cit. on p. 29).
- [284] Fabbri, F.; Villani, M.; Catellani, A.; Calzolari, A.; Cicero, G.; Calestani, D.; Calestani, G.; Zappettini, A.; Dierre, B.; Sekiguchi, T.; Salviati, G. *Scientific Reports* **2014**, *4*, 5158 (cit. on p. 29).
- [285] Frodason, Y. K.; Johansen, K. M.; Bjørheim, T. S.; Svensson, B. G.; Alkauskas, A. *Physical Review B* **2017**, *95* (cit. on pp. 29, 85).
- [286] Frodason, Y. K.; Johansen, K. M.; Bjørheim, T. S.; Svensson, B. G.; Alkauskas, A. *Physical Review B* **2018**, *97* (cit. on pp. 29, 30, 85).

- [287] Shimizu, H.; Wilde, M.; Sato, W. *Nuclear Instruments and Methods in Physics Research Section B: Beam Interactions with Materials and Atoms* **2020**, *467*, 13 (cit. on p. 29).
- [288] Herklotz, F.; Hupfer, A.; Johansen, K. M.; Svensson, B. G.; Koch, S. G.; Lavrov, E. V. *Physical Review B* **2015**, *92* (cit. on p. 30).
- [289] De Angelis, F.; Armelao, L. *Physical chemistry chemical physics : PCCP* **2011**, *13*, 467 (cit. on p. 30).
- [290] Monticone, S.; Tufeu, R.; Kanaev, A. V. *The Journal of Physical Chemistry B* **1998**, *102*, 2854 (cit. on p. 30).
- [291] Liu, W.; Li, M.; Guzzon, R. S.; Norberg, E. J.; Parker, J. S.; Lu, M.; Coldren, L. A.; Yao, J. *Nature Photonics* **2016**, *10*, 190 (cit. on p. 30).
- [292] Janotti, A.; van de Walle, C. G. *Applied Physics Letters* **2005**, *87*, 122102 (cit. on p. 30).
- [293] Paudel, T. R.; Lambrecht, W. R. L. *Physical Review B* **2008**, *77*, 205202 (cit. on p. 30).
- [294] Janotti, A.; van de Walle, C. G. *Nature materials* **2007**, *6*, 44 (cit. on p. 30).
- [295] Selim, F. A.; Weber, M. H.; Solodovnikov, D.; Lynn, K. G. *Physical review letters* **2007**, *99*, 085502 (cit. on p. 30).
- [296] Alkauskas, A.; Pasquarello, A. *Physical Review B* **2011**, *84* (cit. on p. 30).
- [297] Buckeridge, J.; Catlow, C. R. A.; Farrow, M. R.; Logsdail, A. J.; Scanlon, D. O.; Keal, T. W.; Sherwood, P.; Woodley, S. M.; Sokol, A. A.; Walsh, A. *Physical Review Materials* **2018**, *2*, 054604 (cit. on p. 30).
- [298] Mun Wong, K.; Alay-e-Abbas, S. M.; Fang, Y.; Shaukat, A.; Lei, Y. *Journal of Applied Physics* **2013**, *114*, 034901 (cit. on p. 30).
- [299] Fra, V.; Beccaria, M.; Milano, G.; Guastella, S.; Bianco, S.; Porro, S.; Laurenti, M.; Stassi, S.; Ricciardi, C. *Nanotechnology* **2020**, *31*, 374001 (cit. on pp. 30, 66).
- [300] Yan, D.; Zhang, W.; Cen, J.; Stavitski, E.; Sadowski, J. T.; Vescovo, E.; Walter, A.; Attenkofer, K.; Stacchiola, D. J.; Liu, M. *Applied Physics Letters* **2017**, *111*, 231901 (cit. on pp. 30, 98).
- [301] Ton-That, C.; Phillips, M. R.; Foley, M.; Moody, S. J.; Stampfl, A. P. J. *Applied Physics Letters* **2008**, *92*, 261916 (cit. on p. 30).
- [302] Koch, S. G.; Lavrov, E. V.; Weber, J. *Physical Review B* **2014**, *89* (cit. on p. 30).
- [303] Zhang, M.; Averseng, F.; Krafft, J.-M.; Borghetti, P.; Costentin, G.; Stankic, S. *The Journal of Physical Chemistry C* **2020**, *124*, 12696 (cit. on p. 30).
- [304] Erhart, P.; Albe, K. *Applied Physics Letters* **2006**, *88*, 201918 (cit. on p. 30).

- [305] Wagner, R. S.; Ellis, W. C. *Applied Physics Letters* **1964**, *4*, 89 (cit. on p. 31).
- [306] Lieber, C. M. *Solid State Communications* **1998**, *107*, 607 (cit. on p. 31).
- [307] Morales; Lieber *Science* **1998**, *279*, 208 (cit. on p. 31).
- [308] Cui, Y.; Lauhon, L. J.; Gudixsen, M. S.; Wang, J.; Lieber, C. M. *Applied Physics Letters* **2001**, *78*, 2214 (cit. on p. 31).
- [309] Finkelman, R. B.; Larson, R. R.; Dwornik, E. J. *Journal of Crystal Growth* **1974**, *22*, 159 (cit. on p. 31).
- [310] Simon, H.; Krekeler, T.; Schaan, G.; Mader, W. *Crystal Growth & Design* **2013**, *13*, 572 (cit. on p. 31).
- [311] Ahlén, N.; Johnsson, M.; Larsson, A.-K.; Sundman, B. *Journal of the European Ceramic Society* **2000**, *20*, 2607 (cit. on p. 31).
- [312] Givargizov, E. I. In *Vapour Growth and Epitaxy*, Cullen, G. W., Kaldis, E., Parker, R. L., Eds.; Elsevier Science: Burlington, 2013, pp 20–30 (cit. on p. 32).
- [313] Wang, Z. L. *Materials Today* **2004**, *7*, 26 (cit. on p. 32).
- [314] Borchers, C.; Muller, S.; Stichtenoth, D.; Schwen, D.; Ronning, C. *The journal of physical chemistry. B* **2006**, *110*, 1656 (cit. on p. 32).
- [315] Ogrisek, M. Kontrolliertes Wachstum von Zinkoxid und Vanadium(IV)-oxid Nanodrähten, Master thesis, Friedrich-Schiller-Universität Jena, 2013 (cit. on p. 32).
- [316] Geburt, S. Lasing and ion beam doping of semiconductor nanowires, Dissertation, Jena: Friedrich-Schiller-Universität, 2012 (cit. on pp. 32, 35–37).
- [317] Zapf, M. Emission tuning of CdS nanowires by temperature and strain, Master thesis, Jena: Friedrich-Schiller-Universität, 2016 (cit. on pp. 33, 61, 67).
- [318] *Electron microscopy: Principles and fundamentals*; Amelinckx, S., Ed.; VCH-Verl.-Ges: Weinheim u.a., 1997 (cit. on p. 34).
- [319] Reimer, L., *Scanning Electron Microscopy: Physics of Image Formation and Microanalysis*, Second Completely Revised and Updated Edition; Springer Series in Optical Sciences, Vol. 45; Springer Berlin Heidelberg: Berlin, Heidelberg and s.l., 1998 (cit. on pp. 34, 35).
- [320] Russ, J. C.; Frs, M. A.; Kiessling, R.; Charles, J., *Fundamentals of Energy Dispersive X-Ray Analysis: Butterworths Monographs in Materials*; Elsevier Science: Burlington, 1984 (cit. on p. 35).
- [321] *Scanning* **1979**, *2*, 126 (cit. on p. 38).

- [322] Martínez-Criado, G.; Villanova, J.; Tucoulou, R.; Salomon, D.; Suuronen, J.-P.; Labouré, S.; Guilloud, C.; Valls, V.; Barrett, R.; Gagliardini, E.; Dabin, Y.; Baker, R.; Bohic, S.; Cohen, C.; Morse, J. *Journal of synchrotron radiation* **2016**, *23*, 344 (cit. on p. 38).
- [323] Solé, V. A.; Papillon, E.; Cotte, M.; Walter, P.; Susini, J. *Spectrochimica Acta Part B: Atomic Spectroscopy* **2007**, *62*, 63 (cit. on p. 39).
- [324] Henderson, G. S.; de Groot, F. M. F.; Moulton, B. J. A. *Reviews in Mineralogy and Geochemistry* **2014**, *78*, 75 (cit. on pp. 39, 50, 54).
- [325] Stampanoni, M.; Borchert, G.; Wyss, P.; Abela, R.; Patterson, B.; Hunt, S.; Vermeulen, D.; Rüegsegger, P. *Nuclear Instruments and Methods in Physics Research Section A: Accelerators, Spectrometers, Detectors and Associated Equipment* **2002**, *491*, 291 (cit. on p. 41).
- [326] Lezhneva, G. M.; Melkadze, R. G.; Khvedelidze, L. V. *Russian Microelectronics* **2005**, *34*, 229 (cit. on p. 41).
- [327] Wallentin, J.; Osterhoff, M.; Wilke, R. N.; Persson, K.-M.; Wernersson, L.-E.; Sprung, M.; Salditt, T. *Nano letters* **2014**, *14*, 7071 (cit. on pp. 43–45).
- [328] Luo, Z.; Moch, J. G.; Johnson, S. S.; Chen, C. C. *Curr Nanosci (Current Nanoscience)* **2017**, *13* (cit. on p. 43).
- [329] van Bokhoven, J. A.; Lamberti, C., *X-ray absorption and X-ray emission spectroscopy: Theory and applications*; X-ray Absorption and X-ray Emission Spectroscopy: Theory and Applications; John Wiley & Sons Inc: Chichester, West Sussex, 2015 (cit. on p. 44).
- [330] Vakulov, D. et al. *Nano letters* **2020**, *20*, 2703 (cit. on p. 45).
- [331] Gil, E.; Dubrovskii, V. G.; Avit, G.; André, Y.; Leroux, C.; Lekhal, K.; Grecenkov, J.; Trassoudaine, A.; Castelluci, D.; Monier, G.; Ramdani, R. M.; Robert-Goumet, C.; Bideux, L.; Harmand, J. C.; Glas, F. *Nano letters* **2014**, *14*, 3938 (cit. on p. 45).
- [332] Gutsche, C.; Niepelt, R.; Gnauck, M.; Lysov, A.; Prost, W.; Ronning, C.; Tegude, F.-J. *Nano letters* **2012**, *12*, 1453 (cit. on p. 45).
- [333] Gustafsson, A.; Bolinsson, J.; Sköld, N.; Samuelson, L. *Applied Physics Letters* **2010**, *97*, 072114 (cit. on p. 45).
- [334] Joshi, R.; Grondin, R. O. *Applied Physics Letters* **1989**, *54*, 2438 (cit. on p. 45).
- [335] Kaneto, T.; Kim, K. W.; Littlejohn, M. A. *Applied Physics Letters* **1993**, *63*, 48 (cit. on p. 45).
- [336] Parkinson, P.; Joyce, H. J.; Gao, Q.; Tan, H. H.; Zhang, X.; Zou, J.; Jagadish, C.; Herz, L. M.; Johnston, M. B. *Nano letters* **2009**, *9*, 3349 (cit. on pp. 45, 46, 57, 96).
- [337] Parkinson, P.; Lloyd-Hughes, J.; Gao, Q.; Tan, H. H.; Jagadish, C.; Johnston, M. B.; Herz, L. M. *Nano Letters* **2007**, *7*, 2162 (cit. on pp. 45, 58).

- [338] Buttar, C. *Nuclear Instruments and Methods in Physics Research Section A: Accelerators, Spectrometers, Detectors and Associated Equipment* **1997**, 395, 1 (cit. on p. 45).
- [339] Alig, R. C.; Bloom, S. *Physical Review Letters* **1975**, 35, 1522 (cit. on p. 45).
- [340] Seltzer, S. Tables of X-Ray Mass Attenuation Coefficients and Mass Energy-Absorption Coefficients, NIST Standard Reference Database 126, 1995 (cit. on p. 46).
- [341] Joyce, H. J.; Baig, S. A.; Parkinson, P.; Davies, C. L.; Boland, J. L.; Tan, H. H.; Jagadish, C.; Herz, L. M.; Johnston, M. B. *Journal of Physics D: Applied Physics* **2017**, 50, 224001 (cit. on pp. 46, 96).
- [342] Sager, D.; Gutsche, C.; Prost, W.; Tegude, F.-J.; Bacher, G. *Journal of Applied Physics* **2013**, 113, 174303 (cit. on pp. 46, 56).
- [343] Martínez-Criado, G.; Segura-Ruiz, J.; Chu, M.-H.; Tucoulou, R.; López, I.; Nogales, E.; Mendez, B.; Piqueras, J. *Nano letters* **2014**, 14, 5479 (cit. on pp. 48, 50, 51, 53).
- [344] Ram Boppana, V. B.; Doren, D. J.; Lobo, R. F. *Journal of Materials Chemistry* **2010**, 20, 9787 (cit. on pp. 48, 50, 51, 53).
- [345] Johannes, A.; Salomon, D.; Martinez-Criado, G.; Glaser, M.; Lugstein, A.; Ronning, C. *Science advances* **2017**, 3, eaao4044 (cit. on pp. 49, 54).
- [346] Nishi, K.; Shimizu, K.-i.; Takamatsu, M.; Yoshida, H.; Satsuma, A.; Tanaka, T.; Yoshida, S.; Hattori, T. *The Journal of Physical Chemistry B* **1998**, 102, 10190 (cit. on p. 50).
- [347] Faro, A. C.; Rodrigues, V. d. O.; Eon, J.-G. *The Journal of Physical Chemistry C* **2011**, 115, 4749 (cit. on p. 50).
- [348] Pearton, S. J.; Yang, J.; Cary, P. H.; Ren, F.; Kim, J.; Tadjer, M. J.; Mastro, M. A. *Applied Physics Reviews* **2018**, 5, 011301 (cit. on p. 50).
- [349] Pizzini, S.; Roberts, K. J.; Greaves, G. N.; Barrett, N. T.; Dring, I.; Oldman, R. J. *Faraday Discussions of the Chemical Society* **1990**, 89, 51 (cit. on p. 50).
- [350] Machon, D.; McMillan, P. F.; Xu, B.; Dong, J. *Physical Review B* **2006**, 73, 1183 (cit. on p. 50).
- [351] Dymock, K.; Palenik, G. J. *Acta Crystallographica Section B Structural Crystallography and Crystal Chemistry* **1974**, 30, 1364 (cit. on p. 50).
- [352] Thurmond, C. D. *Journal of The Electrochemical Society* **1980**, 127, 1366 (cit. on p. 50).
- [353] Al Hassan, A.; Lähnemann, J.; Davtyan, A.; Al-Humaidi, M.; Herranz, J.; Bahrami, D.; Anjum, T.; Bertram, F.; Dey, A. B.; Geelhaar, L.; Pietsch, U. *Journal of Synchrotron Radiation* **2020**, 27, 1200 (cit. on pp. 52, 96).

- [354] Wallander, H.; Wallentin, J. *Journal of Synchrotron Radiation* **2017**, *24*, 925 (cit. on pp. 52, 57, 58).
- [355] *Hot electrons in semiconductors: Physics and devices*; Balkan, N., Ed.; Oxford science publications, Vol. 5; Clarendon Press: Oxford, 1998 (cit. on p. 57).
- [356] Shah; Pinczuk; Gossard; Wiegmann *Physical review letters* **1985**, *54*, 2045 (cit. on p. 57).
- [357] Long, A. P.; Beton, P. H.; Kelly, M. J. *Semiconductor Science and Technology* **1986**, *1*, 63 (cit. on pp. 57, 58).
- [358] Wittenbecher, L.; Viñas Boström, E.; Vogelsang, J.; Lehman, S.; Dick, K. A.; Verdozzi, C.; Zigmantas, D.; Mikkelsen, A. *ACS nano* **2021**, *15*, 1133 (cit. on pp. 57, 58).
- [359] Schreiber, E.; Fitting, H.-J. *Journal of Electron Spectroscopy and Related Phenomena* **2003**, *131-132*, 87 (cit. on p. 57).
- [360] Gadzuk *Physical Review Letters* **1996**, *76*, 4234 (cit. on p. 57).
- [361] Buntin; Richter; Cavanagh; King *Physical review letters* **1988**, *61*, 1321 (cit. on p. 57).
- [362] Barman, S.; Srivastava, G. P. *Physical Review B* **2006**, *73*, 71 (cit. on pp. 57, 59).
- [363] Soini, M.; Zardo, I.; Uccelli, E.; Funk, S.; Koblmüller, G.; Fontcuberta i Morral, A.; Abstreiter, G. *Applied Physics Letters* **2010**, *97*, 263107 (cit. on pp. 57–59).
- [364] Kim, J. H.; Seong, D.; Ihm, G. H.; Rhee, C. *International Journal of Thermophysics* **1998**, *19*, 281 (cit. on p. 57).
- [365] Carlson, R. O.; Slack, G. A.; Silverman, S. J. *Journal of Applied Physics* **1965**, *36*, 505 (cit. on p. 57).
- [366] Hayes, J.; Levi, A. *IEEE Journal of Quantum Electronics* **1986**, *22*, 1744 (cit. on p. 58).
- [367] Fischetti; Laux *Physical review. B, Condensed matter* **1988**, *38*, 9721 (cit. on p. 58).
- [368] Gunn, J. B. *Solid State Communications* **1963**, *1*, 88 (cit. on p. 59).
- [369] Sobhani, A.; Knight, M. W.; Wang, Y.; Zheng, B.; King, N. S.; Brown, L. V.; Fang, Z.; Nordlander, P.; Halas, N. J. *Nature communications* **2013**, *4*, 1643 (cit. on p. 59).
- [370] Takeda, E.; Suzuki, N. *IEEE Electron Device Letters* **1983**, *4*, 111 (cit. on p. 59).
- [371] Duan, X.; Huang, Y.; Agarwal, R.; Lieber, C. M. *Nature* **2003**, *421*, 241 (cit. on p. 61).
- [372] Yang, X. et al. *ACS nano* **2020**, *14*, 3397 (cit. on p. 61).
- [373] Voss, T.; Kudyk, I.; Wischmeier, L.; Gutowski, J. *physica status solidi (b)* **2009**, *246*, 311 (cit. on p. 62).
- [374] Varshni, Y. P. *Physica* **1967**, *34*, 149 (cit. on p. 63).

- [375] Onufrijevs, P.; Medvids, A.; Dauksta, E.; Mimura, H.; Andrulevicius, M.; Berezovska, N.; Dmitruk, I.; Grase, L.; Mezinskas, G. *Optics & Laser Technology* **2016**, *86*, 21 (cit. on pp. 64, 68).
- [376] Wagner, R. E.; Tomlinson, W. J. *Applied optics* **1982**, *21*, 2671 (cit. on p. 64).
- [377] Shan, F. K.; Kim, B. I.; Liu, G. X.; Liu, Z. F.; Sohn, J. Y.; Lee, W. J.; Shin, B. C.; Yu, Y. S. *Journal of Applied Physics* **2004**, *95*, 4772 (cit. on p. 64).
- [378] Guo, P.; Zhuang, X.; Xu, J.; Zhang, Q.; Hu, W.; Zhu, X.; Wang, X.; Wan, Q.; He, P.; Zhou, H.; Pan, A. *Nano letters* **2013**, *13*, 1251 (cit. on p. 66).
- [379] Wille, M.; Sturm, C.; Michalsky, T.; Röder, R.; Ronning, C.; Schmidt-Grund, R.; Grundmann, M. *Nanotechnology* **2016**, *27*, 225702 (cit. on pp. 68, 99).
- [380] van Exter, M. P.; Nienhuis; Woerdman *Physical Review A* **1996**, *54*, 3553 (cit. on p. 69).
- [381] Wille, M.; Michalsky, T.; Krüger, E.; Grundmann, M.; Schmidt-Grund, R. *Applied Physics Letters* **2016**, *109*, 061102 (cit. on p. 70).
- [382] Faist, J.; Capasso, F.; Sivco, D. L.; Hutchinson, A. L.; Sirtori, C.; Chu, S. N. G.; Cho, A. Y. *Applied Physics Letters* **1994**, *65*, 2901 (cit. on p. 70).
- [383] Fallert, J.; Dietz, R. J. B.; Zhou, H.; Sartor, J.; Klingshirn, C.; Kalt, H. *physica status solidi (c)* **2009**, *6*, 449 (cit. on p. 70).
- [384] Tatebayashi, J.; Kako, S.; Ho, J.; Ota, Y.; Iwamoto, S.; Arakawa, Y. *Nature Photonics* **2015**, *9*, 501 (cit. on p. 70).
- [385] Versteegh, M. A. M.; Vanmaekelbergh, D.; Dijkhuis, J. I. *Physical review letters* **2012**, *108*, 157402 (cit. on p. 70).
- [386] Bonse, J.; Baudach, S.; Krüger, J.; Kautek, W.; Lenzner, M. *Applied Physics A* **2002**, *74*, 19 (cit. on pp. 70, 99).
- [387] Manenkov, A. A.; Prokhorov, A. M. *Soviet Physics Uspekhi* **1986**, *29*, 104 (cit. on pp. 70, 99).
- [388] Ichige, K.; Matsumoto, Y.; Namiki, A. *Nuclear Instruments and Methods in Physics Research Section B: Beam Interactions with Materials and Atoms* **1988**, *33*, 820 (cit. on p. 71).
- [389] Namiki, A.; Cho, S.; Ichige, K. *Japanese Journal of Applied Physics* **1987**, *26*, 39 (cit. on p. 71).
- [390] van Vechten, J. A.; Tsu, R.; Saris, F. W. *Physics Letters A* **1979**, *74*, 422 (cit. on p. 71).
- [391] Yamane, T.; Nagai, N.; Katayama, S.-i.; Todoki, M. *Journal of Applied Physics* **2002**, *91*, 9772 (cit. on p. 72).
- [392] Slack, G. A. *Physical Review* **1961**, *122*, 1451 (cit. on p. 72).

- [393] Lambropoulos, J. C.; Jolly, M. R.; Amsden, C. A.; Gilman, S. E.; Sinicropi, M. J.; Diakomihalis, D.; Jacobs, S. D. *Journal of Applied Physics* **1989**, *66*, 4230 (cit. on p. 72).
- [394] Cahill, D. G.; Lee, S.-M.; Selinder, T. I. *Journal of Applied Physics* **1998**, *83*, 5783 (cit. on p. 72).
- [395] Shi, C.; Luu, D. K.; Yang, Q.; Liu, J.; Chen, J.; Ru, C.; Xie, S.; Luo, J.; Ge, J.; Sun, Y. *Microsystems & Nanoengineering* **2016**, *2*, 16024 (cit. on p. 72).
- [396] Dierre, B.; Yuan, X. L.; Sekiguchi, T. *Journal of Applied Physics* **2008**, *104*, 043528 (cit. on p. 72).
- [397] Lähnemann, J.; Flissikowski, T.; Wölz, M.; Geelhaar, L.; Grahn, H. T.; Brandt, O.; Jahn, U. *Nanotechnology* **2016**, *27*, 455706 (cit. on pp. 72, 76, 91).
- [398] Milano, G.; D'Ortenzi, L.; Bejtka, K.; Mandrile, L.; Giovannozzi, A. M.; Boarino, L.; Pirri, C. F.; Ricciardi, C.; Porro, S. *The Journal of Physical Chemistry C* **2018**, *122*, 8011 (cit. on pp. 73, 76, 98).
- [399] Fang, Z.-Q.; Claflin, B.; Look, D. C.; Farlow, G. C. *Journal of Applied Physics* **2007**, *101*, 086106 (cit. on pp. 73, 77).
- [400] Look, D. C.; Reynolds, D. C.; Hemsley, J. W.; Jones, R. L.; Sizelove, J. R. *Applied Physics Letters* **1999**, *75*, 811 (cit. on pp. 73, 77).
- [401] Look, D. C.; Hemsley, J. W.; Sizelove, J. R. *Physical Review Letters* **1999**, *82*, 2552 (cit. on pp. 73, 77).
- [402] Tuomisto, F.; Saarinen, K.; Look, D. C.; Farlow, G. C. *Physical Review B* **2005**, *72*, 811 (cit. on pp. 73, 77).
- [403] Kappers, L. A.; Gilliam, O. R.; Evans, S. M.; Halliburton, L. E.; Giles, N. C. *Nuclear Instruments and Methods in Physics Research Section B: Beam Interactions with Materials and Atoms* **2008**, *266*, 2953 (cit. on pp. 73, 77, 85).
- [404] Lorenz, K.; Peres, M.; Franco, N.; Marques, J. G.; Miranda, S. M. C.; Magalhães, S.; Monteiro, T.; Wesch, W.; Alves, E.; Wendler, E. In *Oxide-based Materials and Devices II*, ed. by Teherani, F. H.; Look, D. C.; Rogers, D. J., SPIE: 2011, 79400O (cit. on p. 73).
- [405] Empizo, M. J. F. et al. *Applied Physics Express* **2015**, *8*, 061101 (cit. on p. 73).
- [406] Polyakov, A. Y.; Smirnov, N. B.; Govorkov, A. V.; Kozhukhova, E. A.; Vdovin, V. I.; Ip, K.; Overberg, M. E.; Heo, Y. W.; Norton, D. P.; Pearton, S. J.; Zavada, J. M.; Dravin, V. A. *Journal of Applied Physics* **2003**, *94*, 2895 (cit. on p. 73).
- [407] Wendler, E.; Bilani, O.; Gärtner, K.; Wesch, W.; Hayes, M.; Auret, F. D.; Lorenz, K.; Alves, E. *Nuclear Instruments and Methods in Physics Research Section B: Beam Interactions with Materials and Atoms* **2009**, *267*, 2708 (cit. on pp. 73, 99).

- [408] Pal, S.; Sarkar, A.; Chattopadhyay, S.; Chakrabarti, M.; Sanyal, D.; Kumar, P.; Kanjilal, D.; Rakshit, T.; Ray, S. K.; Jana, D. *Nuclear Instruments and Methods in Physics Research Section B: Beam Interactions with Materials and Atoms* **2013**, *311*, 20 (cit. on pp. 73, 99).
- [409] Espinet-Gonzalez, P.; Barrigón, E.; Otnes, G.; Vescovi, G.; Mann, C.; France, R. M.; Welch, A. J.; Hunt, M. S.; Walker, D.; Kelzenberg, M. D.; Åberg, I.; Borgström, M. T.; Samuelson, L.; Atwater, H. A. *ACS nano* **2019**, *13*, 12860 (cit. on p. 73).
- [410] Swart, H.; Greeff, A.; Holloway, P.; Berning, G. *Applied Surface Science* **1999**, *140*, 63 (cit. on p. 74).
- [411] Liao, Z.-M.; Zhang, H.-Z.; Zhou, Y.-B.; Xu, J.; Zhang, J.-M.; Yu, D.-P. *Physics Letters A* **2008**, *372*, 4505 (cit. on p. 75).
- [412] An, W.; Wu, X.; Zeng, X. C. *The Journal of Physical Chemistry C* **2008**, *112*, 5747 (cit. on p. 75).
- [413] Pfahnl, A., *Advances in Electron Tube Techniques*; Pergamon: New York, 1961 (cit. on p. 75).
- [414] Swart, H. C.; Sebastian, J. S.; Trottier, T. A.; Jones, S. L.; Holloway, P. H. *Journal of Vacuum Science & Technology A: Vacuum, Surfaces, and Films* **1996**, *14*, 1697 (cit. on pp. 75, 76).
- [415] Coetsee, E.; Swart, H. C.; Terblans, J. J. *Journal of Vacuum Science & Technology A: Vacuum, Surfaces, and Films* **2007**, *25*, 1226 (cit. on pp. 75, 76).
- [416] Nagpure, I. M.; Pitale, S. S.; Coetsee, E.; Ntwaeaborwa, O. M.; Terblans, J. J.; Swart, H. C. *Applied Surface Science* **2011**, *257*, 10147 (cit. on pp. 75, 76).
- [417] Holloway, P. H.; Swart, H. C.; Martin Ntwaeaborwa, O. *Journal of Vacuum Science & Technology A: Vacuum, Surfaces, and Films* **2013**, *31*, 050808 (cit. on pp. 75, 76).
- [418] Kondoleon, C. A.; Rack, P.; Lambers, E.; Holloway, P. *Journal of Vacuum Science & Technology A: Vacuum, Surfaces, and Films* **2000**, *18*, 2699 (cit. on pp. 75, 76).
- [419] Swart, H. C.; Oosthuizen, L.; Holloway, P. H.; Berning, G. L. P. *Surface and Interface Analysis* **1998**, *26*, 337 (cit. on p. 76).
- [420] Egerton, R. F.; Li, P.; Malac, M. *Micron (Oxford, England : 1993)* **2004**, *35*, 399 (cit. on pp. 76, 77).
- [421] Postek, M. T.; Vladár, A. E.; Purushotham, K. P. *Scanning* **2014**, *36*, 347 (cit. on p. 76).
- [422] Ennos, A. E. *British Journal of Applied Physics* **1953**, *4*, 101 (cit. on p. 76).
- [423] Hirsch, P.; Kässens, M.; Püttmann, M.; Reimer, L. *Scanning* **1994**, *16*, 101 (cit. on p. 76).
- [424] Matthews, M. B.; Kearns, S. L.; Buse, B. *Microscopy and Microanalysis* **2018**, *24*, 612 (cit. on p. 76).

- [425] Egerton, R. F.; Rossouw, C. J. *Journal of Physics D: Applied Physics* **1976**, *9*, 659 (cit. on p. 76).
- [426] Hasabeldaim, E.; Ntwaeaborwa, O. M.; Kroon, R. E.; Swart, H. C. *Journal of Vacuum Science & Technology B, Nanotechnology and Microelectronics: Materials, Processing, Measurement, and Phenomena* **2016**, *34*, 041221 (cit. on p. 76).
- [427] Hasabeldaim, E.; Ntwaeaborwa, O. M.; Kroon, R. E.; Craciun, V.; Coetsee, E.; Swart, H. C. *Applied Surface Science* **2017**, *424*, 412 (cit. on pp. 76, 78).
- [428] Yoshiie, T.; Iwanaga, H.; Shibata, N.; Ichihara, M.; Takeuchi, S. *Philosophical Magazine A* **1979**, *40*, 297 (cit. on p. 77).
- [429] Meese, J.; Locker, D. *Solid State Communications* **1972**, *11*, 1547 (cit. on p. 77).
- [430] Ding, Y.; Liu, Y.; Niu, S.; Wu, W.; Wang, Z. L. *Journal of Applied Physics* **2014**, *116*, 154304 (cit. on p. 77).
- [431] Yuan, P.; Wu, J. Y.; Ogletree, D. F.; Urban, J. J.; Dames, C.; Ma, Y. *Nano letters* **2020**, *20*, 3019 (cit. on p. 77).
- [432] Tanaka, S.-i.; Mase, K.; Nagaoka, S.-i. *Surface Science* **2004**, *572*, 43 (cit. on p. 77).
- [433] Dierre, B.; Yuan, X.; Ueda, K.; Sekiguchi, T. *Journal of Applied Physics* **2010**, *108*, 104902 (cit. on pp. 77, 86).
- [434] Ohashi, N.; Ishigaki, T.; Okada, N.; Sekiguchi, T.; Sakaguchi, I.; Haneda, H. *Applied Physics Letters* **2002**, *80*, 2869 (cit. on p. 78).
- [435] Ohashi, N.; Ishigaki, T.; Okada, N.; Taguchi, H.; Sakaguchi, I.; Hishita, S.; Sekiguchi, T.; Haneda, H. *Journal of Applied Physics* **2003**, *93*, 6386 (cit. on p. 78).
- [436] Sekiguchi, T.; Ohashi, N.; Terada, Y. *Japanese Journal of Applied Physics* **1997**, *36*, L289 (cit. on p. 78).
- [437] Dong, J. J.; Zhang, X. W.; You, J. B.; Cai, P. F.; Yin, Z. G.; An, Q.; Ma, X. B.; Jin, P.; Wang, Z. G.; Chu, P. K. *ACS applied materials & interfaces* **2010**, *2*, 1780 (cit. on p. 78).
- [438] Empizo, M. J. F. et al. *Journal of Applied Physics* **2017**, *121*, 175102 (cit. on p. 78).
- [439] Lord, A. M.; Consonni, V.; Cossuet, T.; Donatini, F.; Wilks, S. P. *ACS applied materials & interfaces* **2020**, *12*, 13217 (cit. on p. 78).
- [440] Xue, X.; Wang, T.; Jiang, X.; Jiang, J.; Pan, C.; Wu, Y. *CrystEngComm* **2014**, *16*, 1207 (cit. on p. 78).
- [441] Goldberg, R. D.; Williams, J. S.; Elliman, R. G. *Nuclear Instruments and Methods in Physics Research Section B: Beam Interactions with Materials and Atoms* **1995**, *106*, 242 (cit. on p. 80).

- [442] Kucheyev, S. O.; Boudinov, H.; Williams, J. S.; Jagadish, C.; Li, G. *Journal of Applied Physics* **2002**, *91*, 4117 (cit. on p. 80).
- [443] Williams, J. S.; Short, K. T.; Elliman, R. G.; Ridgway, M. C.; Goldberg, R. *Nuclear Instruments and Methods in Physics Research Section B: Beam Interactions with Materials and Atoms* **1990**, *48*, 431 (cit. on p. 80).
- [444] Dierre, B.; Yuan, X. L.; Sekiguchi, T. *Microelectronics Journal* **2009**, *40*, 262 (cit. on p. 86).
- [445] Bond, W. L. *Journal of Applied Physics* **1965**, *36*, 1674 (cit. on p. 90).
- [446] Bjørheim, T. S.; Erdal, S.; Johansen, K. M.; Knutsen, K. E.; Norby, T. *The Journal of Physical Chemistry C* **2012**, *116*, 23764 (cit. on p. 93).
- [447] Donatini, F.; Sartel, C.; Sallet, V.; Pernot, J. *Nanotechnology* **2017**, *28*, 235701 (cit. on p. 93).
- [448] Lauhon, L. J.; Gudiksen, M. S.; Wang, D.; Lieber, C. M. *Nature* **2002**, *420*, 57 (cit. on p. 96).
- [449] Torino, L., Benoist, N., Ewald, F., Plouviez, E., Pons, J.-L., Roche, B., Scheidt, K., Taoutaou, F., Uberto, F., Eds., *Beam Instrumentation Performances through the ESRF-EBS Commissioning*: JACoW Publishing, Geneva, Switzerland, 2020 (cit. on p. 97).
- [450] Tang, K.; Gu, S.-L.; Ye, J.-D.; Zhu, S.-M.; Zhang, R.; Zheng, Y.-D. *Chinese Physics B* **2017**, *26*, 047702 (cit. on p. 98).
- [451] Chen, C.; He, H.; Lu, Y.; Wu, K.; Ye, Z. *ACS applied materials & interfaces* **2013**, *5*, 6354 (cit. on p. 98).
- [452] Barnett, C. J.; Navarro-Torres, J.; McGettrick, J. D.; Maffei, T. G. G.; Barron, A. R. *Nanotechnology* **2020**, *31*, 505705 (cit. on p. 98).
- [453] Röder, R.; Sidiropoulos, T. P. H.; Tessarek, C.; Christiansen, S.; Oulton, R. F.; Ronning, C. *Nano letters* **2015**, *15*, 4637 (cit. on p. 99).
- [454] Hollinger, R.; Malevich, P.; Shumakova, V.; Ališauskas, S.; Zapf, M.; Röder, R.; Pugžlys, A.; Baltuška, A.; Ronning, C.; Spielmann, C.; Kartashov, D. *Nano letters* **2019**, *19*, 3563 (cit. on p. 99).

A. List of publications

1. **Zapf, M.**; Ritzer, M.; Liborius, L.; Johannes, A.; Hafermann, M.; Schönherr, S.; Segura-Ruiz, J.; Martínez-Criado, G.; Prost, W. and Ronning, C.
Hot electrons in a nanowire hard X-ray detector. *Nature Communications* **2020**, *11*(1), 4727.
2. **Zapf, M.**; Sidiropoulos, T. and Röder, R.
Tailoring Spectral and Temporal Properties of Semiconductor Nanowire Lasers. *Advanced Optical Materials* **2019**, *7*, 1900504.
3. **Zapf, M.**; Röder, R.; Winkler, K.; Kaden, L.; Greil, J.; Wille, M.; Grundmann, M.; Schmidt-Grund, R.; Lugstein, A. and Ronning, C.
Dynamical Tuning of Nanowire Lasing Spectra. *Nano letters* **2017**, *17*, 6637.
4. **Zapf, M.**; Ronning, C. and Röder, R.
High temperature limit of semiconductor nanowire lasers. *Appl. Phys. Lett.* **2017** *110* (17), 173103.
5. Hafermann, M.; **Zapf, M.**; Ritzer, M.; Printscher, A.; Luo, Y.; Ambrosio, A.; Wilson, W. L. and Ronning, C.
Grayscale Nanopatterning of Phase-Change Materials for Subwavelength-Scaled, Inherently Planar, Nonvolatile, and Reconfigurable Optical Devices. *ACS Applied Nano Materials* **2020**, *3* (5), 4486-4493.
6. Schütt, F.; **Zapf, M.**; Signetti, S.; Strobel, J.; Krüger, H.; Röder, R.; Carstensen, J.; Wolff, N.; Marx, J.; Carey, T.; Schweichel, M.; Terasa, M.-I.; Siebert, L.; Hong, H.-K.; Kaps, S.; Fiedler, B.; Mishra, Y. K.; Lee, Z.; Pugno, N. M.; Kienle, L.; Ferrari, A. C.; Torrisi, F.; Ronning, C. and Adelung, R.
Conversionless efficient and broadband laser light diffusers for high brightness illumination applications. *Nat Commun* **2020**, *11* (1), 1437.
7. Kennedy, O. W.; **Zapf, M.**; Audinot, J.-N.; Pal, S.; Eswara, S.; Wirtz, T.; Ronning, C. and Warburton, P. A.
Photoluminescence of ZnO/ZnMgO heterostructure nanobelts grown by MBE. *Nanotechnology* **2020**, *31* (13), 135604.

8. Plass, C. T.; Ritzer, M.; Schöppe, P.; Schönherr, S.; **Zapf, M.**; Hafermann, M.; Johannes, A.; Martínez-Criado, G.; Segura-Ruiz, J.; Würz, R.; Jackson, P.; Schnohr, C. S. and Ronning, C.
In-Operando Nanoscale X-ray Analysis Revealing the Local Electrical Properties of Rubidium-Enriched Grain Boundaries in Cu(In,Ga)Se₂ Solar Cells. *ACS applied materials & interfaces* **2020**, *12* (51), 57117–57123.
9. Hollinger, R.; Gupta, D.; **Zapf, M.**; Karst, M.; Röder, R.; Uschmann, I.; Reislöhner, U.; Kartashov, D.; Ronning, C. and Spielmann, C.
Polarization dependent multiphoton absorption in ZnO thin films. *J. Phys. D: Appl. Phys.* **2020**, *53* (5), 55102.
10. Hollinger, R.; Herrmann, P.; Korolev, V.; **Zapf, M.**; Shumakova, V.; Röder, R.; Uschmann, I.; Pugžlys, A.; Baltuška, A.; Zürich, M.; Ronning, C.; Spielmann, C. and Kartashov, D.
Polarization Dependent Excitation and High Harmonic Generation from Intense Mid-IR Laser Pulses in ZnO. *Nanomaterials*, **2020**, *11* (1), 4.
11. Röder, R.; Geburt, S.; **Zapf, M.**; Franke, D.; Lorke, M.; Frauenheim, T.; da Rosa, A. L. and Ronning, C.
Transition Metal and Rare Earth Element Doped Zinc Oxide Nanowires for Optoelectronics. *phys. stat. sol. (b)* **2019**, *256* (4), 1800604.
12. Hollinger, R.; Gupta, D.; **Zapf, M.**; Röder, R.; Kartashov, D.; Ronning, C. and Spielmann, C.
Single nanowire defined emission properties of ZnO nanowire arrays. *J. Phys. D: Appl. Phys.* **2019**, *52* (29), 295101.
13. Strobel, J.; Ghimpu, L.; Postica, V.; Lupan, O.; **Zapf, M.**; Schönherr, S.; Röder, R.; Ronning, C.; Schütt, F.; Mishra, Y. K.; Tiginyanu, I.; Adelung, R.; Marx, J.; Fiedler, B.; Kienle, L.
Improving gas sensing by CdTe decoration of individual Aerographite microtubes. *Nanotechnology*, **2019**, *30* (6), 65501.
14. Hollinger, R.; Malevich, P.; Shumakova, V.; Ališauskas, S.; **Zapf, M.**; Röder, R.; Pugžlys, A.; Baltuška, A.; Ronning, C.; Spielmann, C.; Kartashov, D.
Strong Light-Field Driven Nanolasers. *Nano letters* **2019**, *19* (6), 3563–3568.
15. Schöppe, P.; Schönherr, S.; Jackson, P.; Würz, R.; Wisniewski, W.; Ritzer, M.; **Zapf, M.**; Johannes, A.; Schnohr, C. S. and Ronning, C.
Overall Distribution of Rubidium in Highly Efficient Cu(In,Ga)Se₂ Solar Cells.

ACS applied materials & interfaces **2018**, 10 (47), 40592–40598.

16. Tesch, A.; Röder, R.; **Zapf, M.**; Ronning, C.; Warncke, P.; Fischer, D.; Herrmann, K.-H.; Reichenbach, J. R.; Müller, F. A.
Paramagnetic, NIR -luminescent Nd³⁺- and Gd³⁺-doped fluorapatite as contrast agent for multimodal biomedical imaging. *J Am Ceram Soc* **2018**, 101 (10), 4441–4446.
17. Parkhomenko, I.; Vlasukova, L.; Komarov, F.; Makhavikov, M.; Milchanin, O.; Wendler, E.; **Zapf, M.**; Ronning, C.
Luminescence of ZnO nanocrystals in silica synthesized by dual (Zn, O) implantation and thermal annealing. *J. Phys. D: Appl. Phys.*, **2021**, 54 (26), 265104.

List of oral presentations

1. *Degradation Limits of Optically Pumped Nano Lasers*
DPG spring meeting, Dresden 2017.
2. *High Temperature Limit of Semiconductor Nanowire Lasers*
MRS Fall Meeting, Boston 2017.
3. *Dynamical Tuning of Nanowire Laser Spectra*
DPG spring meeting, Berlin 2018.
4. *Wavelength-Selective Reflection Enhancement in Semiconductor Nanowires*
MRS Fall Meeting, Boston 2018.
5. *Distributed Bragg Reflectors in Nanowires towards Impurity Nanolasers*
DPG spring meeting, Regensburg 2019.
6. *Semiconductor Nanowire Photonics*
Laboratory for Electronic Materials and Devices, University College London 2020.

B. Ehrenwörtliche Erklärung

Ich erkläre hiermit ehrenwörtlich, dass ich die vorliegende Arbeit selbständig, ohne unzulässige Hilfe Dritter und ohne Benutzung anderer als der angegebenen Hilfsmittel und Literatur angefertigt habe. Die aus anderen Quellen direkt oder indirekt übernommenen Daten und Konzepte sind unter Angabe der Quelle gekennzeichnet. Bei der Auswahl und Auswertung folgenden Materials haben mir die nachstehend aufgeführten Personen in der jeweils beschriebenen Weise entgeltlich/unentgeltlich geholfen:

- Die Synthese der CdS Nanodrähte wurde von Dr. Marcel Wille durchgeführt.
- ZnO Nanodrähte wurden in Zusammenarbeit mit Lukas Trefflich hergestellt.
- Die GaAs Nanodrähte mit axialem pn-Übergang wurden von Lisa Liborius in der Gruppe von Dr. Werner Prost gewachsen, elektrisch kontaktiert und elektrisch vorcharakterisiert.
- Die Kathodolumineszenz-Spektroskopie an ZnO Nanodrähten wurde in Zusammenarbeit mit Gesine Wolf und Dr. Sven Schönherr durchgeführt.
- Die Photolumineszenz-Spektroskopie an ZnO Nanodrähten wurde in Zusammenarbeit mit Gesine Wolf und Johannes Nicklaus durchgeführt. Lasing-Messungen an elektronenbestrahlten ZnO Nanodrähten wurden in Zusammenarbeit Gesine Wolf durchgeführt. Alle Wellenleitungsexperimente wurden in Zusammenarbeit mit Johannes Nicklaus durchgeführt.
- Messungen zur optischen Zerstörschwelle von Nanodrähten wurden teilweise in Zusammenarbeit mit Dr. Robert Röder im Rahmen meiner Masterarbeit durchgeführt.
- Die kombinierten nano-XRF und nano-XBIC Messungen wurden in Zusammenarbeit mit Dr. Maurizio Ritzer, Dr. Sven Schönherr, Dr. Martin Hafermann, Dr. Andreas Johannes, Dr. Damien Salomon, Dr. Jaime Segura-Ruiz und Dr. Gema Martínez-Criado durchgeführt.
- Im Übrigen waren jeweils die Koautoren der angeführten Veröffentlichungen (siehe Anhang List of Publications) an der Interpretation der Ergebnisse beteiligt.

B. Ehrenwörtliche Erklärung

Weitere Personen waren an der inhaltlich-materiellen Erstellung der vorliegenden Arbeit nicht beteiligt. Insbesondere habe ich hierfür nicht die entgeltliche Hilfe von Vermittlungs- bzw. Beratungsdiensten (Promotionsberater oder andere Personen) in Anspruch genommen. Niemand hat von mir unmittelbar oder mittelbar geldwerte Leistungen für Arbeiten erhalten, die im Zusammenhang mit dem Inhalt der vorgelegten Dissertation stehen.

Die Arbeit wurde bisher weder im In- noch im Ausland in gleicher oder ähnlicher Form einer anderen Prüfungsbehörde vorgelegt.

Die geltende Promotionsordnung der Physikalisch-Astronomischen Fakultät ist mir bekannt.

Ich versichere ehrenwörtlich, dass ich nach bestem Wissen die reine Wahrheit gesagt und nichts verschwiegen habe.

Jena, den 30.09.2021

Maximilian Zapf